

AD_____

Award Number: W81XWH-04-1-0559

TITLE: Concurrent MR-NIR Imaging for Breast Cancer Diagnosis

PRINCIPAL INVESTIGATOR: Birsen Yazici, Ph.D.

CONTRACTING ORGANIZATION: Rensselaer Polytechnic Institute
Troy, NY 12180-3590

REPORT DATE: June 2008

TYPE OF REPORT: Annual

PREPARED FOR: U.S. Army Medical Research and Materiel Command
Fort Detrick, Maryland 21702-5012

DISTRIBUTION STATEMENT: Approved for Public Release;
Distribution Unlimited

The views, opinions and/or findings contained in this report are those of the author(s) and should not be construed as an official Department of the Army position, policy or decision unless so designated by other documentation.

| REPORT DOCUMENTATION PAGE | | | | Form Approved OMB No. 0704-0188 | |
|---|------------------|--------------------------|--------------------------------------|--|--|
| Public reporting burden for this collection of information is estimated to average 1 hour per response, including the time for reviewing instructions, searching existing data sources, gathering and maintaining the data needed, and completing and reviewing this collection of information. Send comments regarding this burden estimate or any other aspect of this collection of information, including suggestions for reducing this burden to Department of Defense, Washington Headquarters Services, Directorate for Information Operations and Reports (0704-0188), 1215 Jefferson Davis Highway, Suite 1204, Arlington, VA 22202-4302. Respondents should be aware that notwithstanding any other provision of law, no person shall be subject to any penalty for failing to comply with a collection of information if it does not display a currently valid OMB control number. PLEASE DO NOT RETURN YOUR FORM TO THE ABOVE ADDRESS. | | | | | |
| 1. REPORT DATE (DD-MM-YYYY) 01-06-2008 | | 2. REPORT TYPE Annual | | 3. DATES COVERED (From - To) 1 Jun 2007 – 31 May 2008 | |
| 4. TITLE AND SUBTITLE Concurrent MR-NIR Imaging for Breast Cancer Diagnosis | | | | 5a. CONTRACT NUMBER | |
| | | | | 5b. GRANT NUMBER W81XWH-04-1-0559 | |
| | | | | 5c. PROGRAM ELEMENT NUMBER | |
| 6. AUTHOR(S) Birsen Yazici, Ph.D. E-Mail: yazici@ecse.rpi.edu | | | | 5d. PROJECT NUMBER | |
| | | | | 5e. TASK NUMBER | |
| | | | | 5f. WORK UNIT NUMBER | |
| 7. PERFORMING ORGANIZATION NAME(S) AND ADDRESS(ES) Rensselaer Polytechnic Institute Troy, NY 12180-3590 | | | | 8. PERFORMING ORGANIZATION REPORT NUMBER | |
| 9. SPONSORING / MONITORING AGENCY NAME(S) AND ADDRESS(ES) U.S. Army Medical Research and Materiel Command Fort Detrick, Maryland 21702-5012 | | | | 10. SPONSOR/MONITOR'S ACRONYM(S) | |
| | | | | 11. SPONSOR/MONITOR'S REPORT NUMBER(S) | |
| 12. DISTRIBUTION / AVAILABILITY STATEMENT Approved for Public Release; Distribution Unlimited | | | | | |
| 13. SUPPLEMENTARY NOTES – Original contains colored plates: ALL DTIC reproductions will be in black and white. | | | | | |
| 14. ABSTRACT The primary objective of this research program is to investigate concurrent near infrared (NIR) optical and magnetic resonance (MR) imaging for breast cancer diagnosis. The NIR diffuse optical imaging offers novel criteria for cancer differentiation with the ability to measure (in vivo) oxygenation and vascularization state, the uptake and release of contrast agents and chromophore concentrations with high sensitivity. However, NIR diffuse optical tomography is inherently a low spatial resolution imaging modality due to diffuse nature of light photons. Alternatively, MRI provides high spatial resolution with excellent tissue discrimination, but has limited ability to monitor hemoglobin dynamics and other contrast mechanisms that optical imaging provides. Therefore, concurrent MRI-NIR optical imaging brings together the most advantageous aspects of the two imaging modalities for breast cancer diagnosis. | | | | | |
| 15. SUBJECT TERMS No subject terms provided. | | | | | |
| 16. SECURITY CLASSIFICATION OF: | | | 17. LIMITATION OF ABSTRACT UU | 18. NUMBER OF PAGES 71 | 19a. NAME OF RESPONSIBLE PERSON USAMRMC |
| a. REPORT U | b. ABSTRACT U | c. THIS PAGE U | | | 19b. TELEPHONE NUMBER (include area code) |

Table of Contents

| | |
|--|--------------|
| Introduction..... | 4-6 |
| Body..... | 6-38 |
| Key Research Accomplishments..... | 39 |
| Reportable Outcomes..... | 39-40 |
| Conclusions..... | 40-41 |
| References..... | 42-47 |
| Appendices..... | 48 |

Concurrent MR-NIR Imaging for Breast Cancer Diagnosis

Birsen Yazici

I. INTRODUCTION

Near infrared (NIR) diffuse optical imaging provides quantitative functional information from breast tissue that can not be obtained by conventional radiological methods. NIR techniques can provide *in vivo* measurements of oxygenation and vascularization state, the uptake and release of molecular contrast agents and chromophore concentrations with high sensitivity. There is considerable evidence that tumor growth is dependent on angiogenesis [1]- [3], and that tumor aggressiveness can be assessed from its increased number of new vessels and reduced oxygenation state relative to normal breast tissue and benign breast lesions [4]- [6]. NIR diffuse optical tomographic (DOT) methods has the potential to characterize angiogenesis related vessel density as it measures the total hemoglobin concentration and provide the ability to differentiate between benign and malignant lesions based on oxygen saturation. Furthermore, NIR methods are non-ionizing, relatively inexpensive and can be made portable.

The diagnosis and management of cancer involves several stages where magnetic resonance (MR) plays a valuable and growing role. MRI of the breast is now a routine part of the clinical care in many centers [9]- [11]. Magnetic Resonance imaging (MRI) is indicated in patients with inconclusive clinical and/or mammographic examinations. Patients that may benefit include women with radiographically dense breasts, and high risk potential population [12]- [13]. MRI possesses less than 10% contrast for soft tissue pathology [14]. Gadolinium (Gd) enhanced MRI offers much better contrast and is specific for tumor vessel imaging. However, the signal in the Gd-MRI arises from the larger vessels as the contrast agent is flushed out of the vascular bed of the tumor [15]. In comparison, NIR measurements of absorption have extremely high contrast. It was reported that 5% change in vascular density as measured histologically in ductal carcinomas leads to approximately 300% contrast in NIR absorption coefficients [7]. Furthermore, there are studies suggesting that the kinetics of contrast enhanced optical

spectroscopy provides information about the cellular spaces [8]. On the other hand, NIR DOT suffers from poor spatial resolution and as such, it is unlikely that NIR imaging will be a stand-alone screening method in the general population. Therefore, we believe that the concurrent MR and NIR imaging brings together the most advantageous aspects of the two imaging modalities (structural and functional). In the future, we envision that this multimodality imaging approach will lead to high resolution hemoglobin tomography and comprehensive quantitative functional tissue characterization to differentiate malignant and benign tumors.

In this project, the clinical studies are performed using the novel MR-NIR hybrid time-resolved spectroscopy (TRS) imager and fast Indocyanine Green (ICG) enhanced spectroscopic imager developed by Dr. Chance, a Co-PI of this proposal, at the University of Pennsylvania (UPenn), Biophysics Department, Diffuse Optical Imaging and Spectroscopy Laboratory.

The central hypothesis of this project is that the concurrent MR-NIR diffuse optical tomographic methods coupled with fast contrast enhanced NIR spectroscopic methods provide fundamentally new quantitative functional and structural information for breast cancer tumor characterization and detection. This new information can be obtained by novel modeling, analysis and data fusion methods from the tomographic, temporal and cellular-based contrast measurements, which exploit fast imaging techniques together with TRS tomographic methods. In this project, we investigate new methods for multi-modality high spatial resolution hemoglobin tomography, pharmacokinetic modeling of molecular contrast agents based on fast NIR spectroscopy and analysis of structural and functional information provided by MR and NIR imaging methods for breast cancer detection based on receiver operating characteristics methodology. Specific aims of the project are as follows:

- Aim 1: Utilize a priori anatomical information provided by MRI, to reconstruct 3D high resolution hemoglobin, water and lipid concentration, and oxygen saturation images directly from 6 wavelength time resolved optical measurements. Evaluate improvements in image reconstruction between that of stand-alone NIR and concurrent MR-NIR measurements using water and lipid images obtained from MRI.
- Aim 2: Develop a compartmentalized pharmacokinetic modeling of ICG, optical contrast agent, and extract quantitative parameters that can characterize tumor metabolism and angiogenesis. Compare ICG kinetics with the Gadolinium, MR contrast agent, kinetics and biopsy findings.
- Aim 3: Evaluate accuracy of breast cancer diagnosis based on the quantitative functional information extracted from stand-alone NIR system. This information includes hemoglobin, water and lipid concentration, optical scatter power and oxygen saturation images, and ICG pharmacokinetic parameters. Evaluate the added value

of ICG kinetic parameters in breast cancer diagnosis.

- Aim 4: Combine NIR based breast cancer diagnosis features with the systematic MR breast architecture and kinetics interpretation model developed by Dr. Nunes, M.D, Co-PI of this proposal, to evaluate the sensitivity and specificity of concurrent MR-NIR imaging method. Compare results with that of stand-alone MR and NIR results.

In the following sections, we will provide detailed description of our current research in line with the statement of work (SOW) and the aims outlined above. For the period of June 1st, 2007 to May 31st 2008, SOW includes only the first two aims of the project.

II. BODY

A. AIM 2 - Direct Reconstruction of Optical Fluorophores

1) *Spatially Resolved Compartmental Modeling and the Two-compartment Model for ICG*: In general, a compartmental model is given by time-dependent coupled ODEs and a measurement model [18]–[20]. Such a model can be extended to include spatial variations in a straightforward manner.

Let $\Omega \subset \mathbb{R}^3$ denote the domain of interest. For an n -compartment model, let $\mathcal{C}(\mathbf{r}, t) \in \mathbb{R}^n$ represent the concentration vector in different compartments at location $\mathbf{r} \in \Omega$, and at time $t \in [T_0, T_1]$; and let $\alpha_n(\mathbf{r})$ denote the parameter vector whose elements are the pharmacokinetic rates and volume fractions at location \mathbf{r} . Then, a spatially-resolved compartmental model can be expressed as the following state-space model:

$$\dot{\mathcal{C}}(\mathbf{r}, t) = \mathcal{K}(\alpha_n(\mathbf{r}))\mathcal{C}(\mathbf{r}, t), \quad (1)$$

$$a(\mathbf{r}, t) = \mathcal{V}(\alpha_n(\mathbf{r}))\mathcal{C}(\mathbf{r}, t) \quad t \in [T_0, T_1], \quad \mathbf{r} \in \Omega, \quad (2)$$

where $\dot{\mathcal{C}}$ denotes the elementwise time-derivative of \mathcal{C} , $\mathcal{K}(\mathbf{r}, \alpha_n) \in \mathbb{R}^{n \times n}$ is the system matrix whose entries are the pharmacokinetic rates, $a(\mathbf{r}, t)$ is the total fluorophore concentration at location \mathbf{r} and time t , and $\mathcal{V}(\mathbf{r}, \alpha_n) \in \mathbb{R}^n$ is the vector comprised of volume fractions.

Although our study is applicable to pharmacokinetic modeling of any optical fluorophore, in the following subsection, we will specifically discuss the spatially-resolved pharmacokinetic modeling of ICG using a two-compartment model due to its relevance to breast cancer studies.

2) *Two-compartment Model for the ICG Pharmacokinetics*: ICG is an optical dye commonly used in retinopathy and hepatic diagnostics. Given its low toxicity and FDA approval, it has recently been utilized as a blood pooling

agent for the detection and diagnosis of cancerous tumors in conjunction with NIR optical methods [34], [35], [37], [41]. In normal tissue, ICG acts as a blood flow indicator in tight capillaries of normal vessels. However in tumors, ICG may act as a diffusible (extravascular) flow in the leaky capillary of cancer vessels. Therefore, the pharmacokinetics of ICG can be used for tumor detection, diagnosis, and staging. Fig. 1 shows the two-compartment model for the ICG kinetics. The two compartments are comprised of plasma and extracellular-extravascular space (EES). Spatially resolved ICG transition between plasma and the EES can be modeled using the following coupled ODEs:

$$\begin{bmatrix} \dot{C}_e(\mathbf{r}, t) \\ \dot{C}_p(\mathbf{r}, t) \end{bmatrix} = \begin{bmatrix} -k_{out}(\mathbf{r}) & k_{in}(\mathbf{r}) \\ k_{out}(\mathbf{r}) & -(k_{in} + k_{elm})(\mathbf{r}) \end{bmatrix} \begin{bmatrix} C_e(\mathbf{r}, t) \\ C_p(\mathbf{r}, t) \end{bmatrix}, \quad t \in [T_0, T_1], \quad \mathbf{r} \in \Omega, \quad (3)$$

where $k_{in}(\mathbf{r})$ and $k_{out}(\mathbf{r})$ are the spatially-resolved pharmacokinetic-rates that govern the leakage into and the drainage out of the EES, $k_{elm}(\mathbf{r})$ describes the ICG elimination from the body through kidneys and liver. The vector $\mathcal{C}(\mathbf{r}, t)$ in (1) and (2) is composed of $C_p(\mathbf{r}, t)$, and $C_e(\mathbf{r}, t)$, representing the ICG concentration in plasma and the EES at $\mathbf{r} \in \Omega$ and $t \in [T_0, T_1]$, respectively.

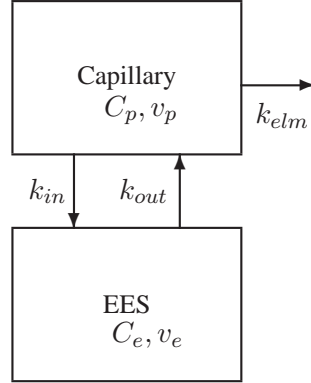


Fig. 1. Block diagram of the two-compartment model for the ICG pharmacokinetics.

The ICG concentration in tissue, $a(\mathbf{r}, t)$, is given as a linear combination of the ICG concentration in plasma and the EES

$$a(\mathbf{r}, t) = v_p(\mathbf{r})C_p(\mathbf{r}, t) + v_e(\mathbf{r})C_e(\mathbf{r}, t) \quad t \in [T_0, T_1], \quad \mathbf{r} \in \Omega, \quad (4)$$

where $v_p(\mathbf{r})$, $v_e(\mathbf{r})$ are spatially-resolved plasma and EES volume fractions, respectively. Here, the unknowns are concentrations in different compartments, pharmacokinetic rates, and volume fractions.

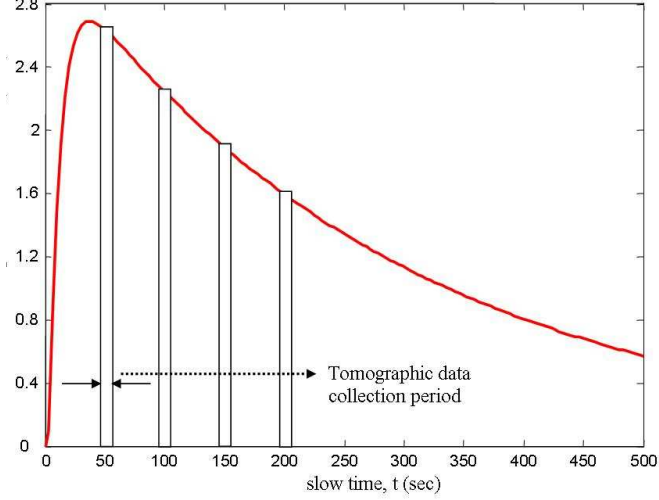


Fig. 2. Total fluorophore concentration versus slow-time variable, t .

We combine all the pharmacokinetic parameters into a single vector and define

$$\alpha_2(\mathbf{r}) = [k_{in}(\mathbf{r}) \quad k_{out}(\mathbf{r}) \quad k_{elm}(\mathbf{r}) \quad v_p(\mathbf{r}) \quad v_e(\mathbf{r})]^T. \quad (5)$$

3) *Concentration-to-Measurement Map for FDOT*: In this work, the quantity we wish to reconstruct is the spatially resolved pharmacokinetic-rate images from a sequence of boundary measurements obtained by diffuse optical tomographic methods. To do this, we first develop a map which relates sequence of boundary measurements to the spatially resolved fluorophore concentrations. We call this map *concentration-to-measurement* (CTM) map.

A suitable CTM map can be developed based on a photon propagation model in fluorescing medium. We use diffusion approximation of radiative transfer equation to model photon propagation where the propagation of excitation and emission light are modeled by two coupled diffusion equations.

To relate time-varying fluorophore concentrations to a sequence of boundary measurements, we parameterize time evolution of the fluorophore concentration by a slow-time parameter t ; and photon propagation during one instance of a tomographic data collection process by a fast-time parameter t' . Note that t' is in the order of the speed of light whereas t is in the order of seconds. Thus, we assume that the absorption and scattering coefficients of tissue are constant during one instance of the tomographic data collection period but vary with the slow-time variable t . As a result, frequency domain couple diffusion equation is adequate to model light propagation during the dynamic data collection process. Figure 2 illustrates a typical time evolution of the fluorophore concentration with respect to slow-time variable t .

In the following subsections, for notational brevity, we drop the slow-time dependence in our equations and set $a(\mathbf{r}, t) = a(\mathbf{r})$, $\mu_{axf}(\mathbf{r}, t) = \mu_{axf}(\mathbf{r})$, $\phi_{x,m}(\mathbf{r}, \omega, t) = \phi_{x,m}(\mathbf{r}, \omega)$, etc. Note that $B_{x,m}$ is a shorthand notation for the quantity B at either excitation or emission wavelengths.

4) *Model for Light Propagation in Fluorescing Medium:* The light propagation at the excitation and emission wavelengths can be modelled by the following coupled diffusion equations: [42]:

$$-\nabla \cdot D_x(\mathbf{r})\nabla\phi_x(\mathbf{r}, \omega) + \left(\mu_{ax}(\mathbf{r}) + \frac{j\omega}{c}\right)\phi_x(\mathbf{r}, \omega) = S(\mathbf{r}, \omega), \quad \mathbf{r} \in \Omega \subset \mathbb{R}^3 \quad (6)$$

$$-\nabla \cdot D_m(\mathbf{r})\nabla\phi_m(\mathbf{r}, \omega) + \left(\mu_{am}(\mathbf{r}) + \frac{j\omega}{c}\right)\phi_m(\mathbf{r}, \omega) = -\phi_x(\mathbf{r}, \omega)\gamma\mu_{axf}(\mathbf{r})\frac{1 - j\omega\tau(\mathbf{r})}{1 + [\omega\tau(\mathbf{r})]^2}. \quad (7)$$

where the subscripts x and m denote the excitation and emission wavelengths, respectively. $\phi_{x,m}(\mathbf{r}, \omega)$ represents the spatially varying optical field in the medium; ω denotes the modulation frequency of the source (the Fourier transform with respect to the fast-time variable t'); c is the speed of light inside the medium Ω ; $\tau(\mathbf{r})$ is the fluorophore lifetime; γ is the fluorophore's quantum efficiency; $\mu_{ax,m}(\mathbf{r})$ stands for the spatially varying absorption coefficient of the medium at the excitation and emission wavelengths, respectively, $\mu_{axf}(\mathbf{r})$ is the fluorophore's absorption coefficient; and $\gamma\mu_{axf}(\mathbf{r})$ is the fluorophore yield; $S(\mathbf{r}, \omega)$ is the excitation source, $D_{x,m}(\mathbf{r})$ is the spatially varying diffusion coefficient given by $D_{x,m}(\mathbf{r}) = \frac{1}{3[\mu'_{sx,m}(\mathbf{r}) + \mu_{ax,m}(\mathbf{r})]}$, where $\mu'_{sx,m}(\mathbf{r})$ is the reduced scattering coefficient.

The optical coefficients at the excitation and emission wavelengths are due to both the endogenous chromophores and exogenous fluorophore. Thus,

$$\mu_{ax}(\mathbf{r}) = \mu_{axe}(\mathbf{r}) + \mu_{axf}(\mathbf{r}), \quad (8)$$

$$\mu_{am}(\mathbf{r}) = \mu_{ame}(\mathbf{r}) + \mu_{amf}(\mathbf{r}). \quad (9)$$

Here, the subscript e denotes the endogenous chromophores, and the subscript f denotes the exogenous fluorophore.

We choose Robin-type boundary conditions given as [46]

$$2D_x(\mathbf{r})\frac{\partial\phi_x(\mathbf{r}, \omega)}{\partial\nu} + \rho\phi_x(\mathbf{r}, \omega) = 0, \quad \mathbf{r} \in \partial\Omega \quad (10)$$

$$2D_m(\mathbf{r})\frac{\partial\phi_m(\mathbf{r}, \omega)}{\partial\nu} + \rho\phi_m(\mathbf{r}, \omega) = 0, \quad (11)$$

where $\partial\Omega$ denotes the boundary of Ω , ν denotes the outward normal of the boundary $\partial\Omega$, ρ is a constant accounting for the refractive index mismatch between the two regions separated by $\partial\Omega$.

Let $a(\mathbf{r})$ denote the concentration of fluorophores at $\mathbf{r} \in \Omega$. The relationship between $a(\mathbf{r})$ and the fluorophore absorption coefficient, $\mu_{a(x,m)f}$, is given by [43]

$$\mu_{a(x,m)f}(\mathbf{r}) = \ln 10 \epsilon_{x,m} a(\mathbf{r}) \quad \mathbf{r} \in \Omega, \quad (12)$$

where $\epsilon_{x,m}$ denotes the fluorophore extinction coefficients at the excitation and emission wavelengths, respectively.

5) *Non-linear Concentration-to-Measurement Map*: Let $\Phi_m(\mathbf{r}_d, \mathbf{r}_s; \omega)$ denote the ratio of the emission data to the excitation data (normalized Born data [46]) at the emission wavelength at the detector location \mathbf{r}_d due to an excitation source at \mathbf{r}_s . The relationship between $\Phi_m(\mathbf{r}_d, \mathbf{r}_s; \omega)$ and $a(\mathbf{r})$ is given by

$$\begin{aligned} \Phi_m(\mathbf{r}_d, \mathbf{r}_s; \omega) &= \frac{\ln 10 \epsilon_x \gamma}{\phi_x(\mathbf{r}_d, \mathbf{r}_s; \omega)} \int_{\Omega} G_m(\mathbf{r}_d, \mathbf{r}; \omega) a(\mathbf{r}) \frac{1 - j\omega\tau(\mathbf{r})}{1 + [\omega\tau(\mathbf{r})]^2} \phi_x(\mathbf{r}, \mathbf{r}_s; \omega) d^3\mathbf{r} \\ &=: \mathcal{F}_{\mathbf{r}_d, \mathbf{r}_s}(a) \end{aligned} \quad (13)$$

where $\phi_x(\mathbf{r}, \mathbf{r}_s; \omega)$ is the photon density at location \mathbf{r} due to a source at \mathbf{r}_s at the excitation wavelength; $G_m(\mathbf{r}_d, \mathbf{r}; \omega)$ is the Green's function of (7) and (11) at \mathbf{r}_d , due to a point source at \mathbf{r} , and $\mathcal{F}_{\mathbf{r}_d, \mathbf{r}_s}(a)$ is the non-linear operator that maps the total fluorophore concentration a to the normalized measurements Φ_m . Note that the non-linearity in (13) is due to the μ_{amf} dependence of $G_m(\mathbf{r}_d, \mathbf{r}; \omega)$, and $\mu_{a(m,x)}$ dependence of ϕ_x .

We assume that: *i*) The endogenous absorption coefficients at the emission and the excitation wavelengths are approximately equal, i.e. $\mu_{ame} \approx \mu_{axe}$. This is a valid assumption for a number of different applications such as small animal and breast imaging [47]. *ii*) The diffusion coefficients at both the excitation and emission wavelengths are independent of the endogenous and exogenous absorption coefficients, i.e. $D_{x,m}(\mathbf{r}) \approx 1/(3\mu'_{sx,m}(\mathbf{r}))$. Furthermore, the diffusion coefficients are known but can be spatially varying. *iii*) The lifetime parameter, $\tau(\mathbf{r})$, $\mathbf{r} \in \Omega$, is known, and not necessarily constant.

Let N_d and N_s denote the number of detectors and sources, respectively. Let Φ be the measurement vector formed by concatenating the measurements for each source-detector pair as follows:

$$\Phi = [\Phi_m(\mathbf{r}_{d_1}, \mathbf{r}_{s_1}; \omega), \dots, \Phi_m(\mathbf{r}_{d_{N_d}}, \mathbf{r}_{s_1}; \omega), \dots, \Phi_m(\mathbf{r}_{d_{N_d}}, \mathbf{r}_{s_{N_s}}; \omega)]^T. \quad (14)$$

Using (13) and (14), we form the following relationship between a and Φ :

$$\Phi =: \mathcal{F}(a), \quad (15)$$

where \mathcal{F} is an operator with matrix kernel in which $\mathcal{F}_{ij} = \mathcal{F}_{\mathbf{r}_{d_i}, \mathbf{r}_{s_j}}$ for $i = 1, \dots, N_d$, $j = 1, \dots, N_s$.

Note that for notational brevity, we assume a single-frequency measurement model. A multi-frequency measurement model is a straightforward extension of the single-frequency measurement model.

6) *Linear Concentration-to-Measurement Map*: An approximate linear map between the normalized measurements and the total fluorophore concentration can be obtained based on the assumption that the presence of exogenous fluorophores does not change the optical coefficients $\mu_{ax,m}$ and $D_{x,m}$ [42]. This assumption leads to the following relationship between the measurements and the fluorophore concentrations:

$$\begin{aligned}\Phi_m(\mathbf{r}_d, \mathbf{r}_s; \omega) &= \frac{\ln 10 \epsilon_x \gamma}{\phi_x^e(\mathbf{r}_d, \mathbf{r}_s; \omega)} \int_{\Omega} G_m^e(\mathbf{r}_d, \mathbf{r}; \omega) a(\mathbf{r}) \frac{1 - j\omega\tau(\mathbf{r})}{1 + [\omega\tau(\mathbf{r})]^2} \phi_x^e(\mathbf{r}, \mathbf{r}_s; \omega) d^3\mathbf{r} \\ &=: \mathcal{W}_{\mathbf{r}_d, \mathbf{r}_s}(a),\end{aligned}\tag{16}$$

where $G_m^e(\mathbf{r}_d, \mathbf{r}; \omega)$ is the Green's function of (7) and (11) when $\mu_{am} = \mu_{ame}$, $\phi_x^e(\mathbf{r}, \mathbf{r}_s; \omega)$ is the predicted optical field at \mathbf{r} due to a source located at \mathbf{r}_s when $\mu_{ax} = \mu_{axe}$, and $\mathcal{W}_{\mathbf{r}_d, \mathbf{r}_s}(a)$ denotes the linear operator that maps the normalized measurement at \mathbf{r}_d due to a source at \mathbf{r}_s to the total fluorophore concentration.

Forming a measurement vector as in (14), we write

$$\Phi =: \mathcal{W}(a)\tag{17}$$

where \mathcal{W} is the linear operator with a matrix kernel in which $\mathcal{W}_{ij} = \mathcal{W}_{\mathbf{r}_{d_i}, \mathbf{r}_{s_j}}$ for $i = 1, \dots, N_d$ $j = 1, \dots, N_s$.

Note that the reconstruction of the pharmacokinetic-rate images that will be discussed in the subsequent sections is not tied to any specific linearization method. Alternatively, a different linear approximation to \mathcal{F} can be obtained by computing its first-order Fréchet derivative to yield a relationship between measurements and total fluorophore concentration. However, we adopted the model in (17) for image reconstruction using *in vivo* breast data.

7) *Pharmacokinetic-rates-to-Measurement Map*: In this section, we combine the CTM map with the spatially resolved compartmental model to obtain a mapping between the spatially resolved pharmacokinetic-rates and sequence of boundary measurements. We call this composite map the *pharmacokinetic-rate-to-measurement* (PTM) map.

Recall that

$$\dot{\mathcal{C}}(\mathbf{r}, t) = \mathcal{K}(\alpha_n(\mathbf{r}))\mathcal{C}(\mathbf{r}, t) \quad t \in [T_0, T_1], \quad \mathbf{r} \in \Omega.\tag{18}$$

Let $\Phi(t)$ denote the measurement vector (16) and $a(\mathbf{r}, t)$ denote the fluorophore concentration at slow-time parameter t . Combining the CTM map (15) with the compartmental model (2), we obtain the following non-linear relationship:

$$\Phi(t) = \mathcal{F}(\mathcal{V}(\alpha_n(\mathbf{r}))\mathcal{C}(\mathbf{r}, t)), \quad t \in [T_0, T_1], \quad \mathbf{r} \in \Omega.\tag{19}$$

For the linear CTM map, (19) becomes

$$\Phi(t) = \mathcal{W}(\mathcal{V}(\alpha_n(\mathbf{r}))\mathcal{C}(\mathbf{r}, t)) \quad t \in [T_0, T_1], \quad \mathbf{r} \in \Omega.\tag{20}$$

The equations (18) & (19) and (18) & (20) constitute the PTM map. We next discretize these equations and incorporate dynamic model uncertainties and measurement noise to the PTM map.

We use first-order Lagrange basis to discretize the domain of interest Ω . Let \mathbf{r}_j , $j = 1, \dots, N$ be the discrete points representing the spatial location of the voxels in Ω . Let $\mathbf{C}(\mathbf{r}_j, t)$ represent the concentration vector at time t in different compartments, and $\alpha_n(\mathbf{r}_j)$ represent the pharmacokinetic-rates and volume fractions at the j^{th} voxel centered at \mathbf{r}_j , $j = 1, \dots, N$. Assuming that the dynamic measurements are collected at time instances, $t = k\Delta$, $k = 1, \dots, K$, where Δ is the sampling period, we define $\mathbf{C}(\mathbf{r}_j, k) = \mathbf{C}(\mathbf{r}_j, k\Delta)$, and express the discrete spatially resolved compartmental model as follows:

$$\mathbf{C}(\mathbf{r}_j, k+1) = \mathbf{K}(\boldsymbol{\theta}_n(\mathbf{r}_j))\mathbf{C}(\mathbf{r}_j, k) + \boldsymbol{\xi}(\mathbf{r}_j, k), \quad k = 1, \dots, K, \quad j = 1, \dots, N, \quad (21)$$

where $\boldsymbol{\xi}(\mathbf{r}_j, k)$ is a zero-mean Gaussian process with $E[\boldsymbol{\xi}(\mathbf{r}_j, k_1)\boldsymbol{\xi}(\mathbf{r}_i, k_2)] = \delta(\mathbf{r}_j - \mathbf{r}_i)\delta(k_1 - k_2)\mathbf{Q}_n$, representing the dynamic model uncertainty; $\mathbf{K}(\boldsymbol{\theta}_n(\mathbf{r}_j)) := e^{\boldsymbol{\kappa}(\boldsymbol{\alpha}_n(\mathbf{r}_j))\Delta}$ is the discrete-time system matrix as described in [48] and, $\boldsymbol{\theta}_n(\mathbf{r}_j)$ represents the discrete-time parameter vector for the pharmacokinetic-rates and volume fractions. For a detailed discussion of the discretization procedure and an explicit relationship between the parameters $\boldsymbol{\theta}_n(\mathbf{r}_j)$ and $\boldsymbol{\alpha}_n(\mathbf{r}_j)$, see [37], [48].

Let $\boldsymbol{\Psi}(k) = \boldsymbol{\Phi}(k\Delta)$. Replacing $\boldsymbol{\alpha}_n(\mathbf{r}_j)$ with $\boldsymbol{\theta}_n(\mathbf{r}_j)$, (19) and (20) are discretized as:

$$\boldsymbol{\Psi}(k) = \mathbf{F}(\mathbf{V}(\boldsymbol{\theta}_n(\mathbf{r}_j))\mathbf{C}(\mathbf{r}_j, k)) + \boldsymbol{\eta}(k), \quad (22)$$

$$\boldsymbol{\Psi}(k) = \mathbf{W}\mathbf{V}(\boldsymbol{\theta}_n(\mathbf{r}_j))\mathbf{C}(\mathbf{r}_j, k) + \boldsymbol{\eta}(k), \quad k = 1, \dots, K, \quad j = 1, \dots, N, \quad (23)$$

where \mathbf{F} and \mathbf{W} are the resulting operators when $\boldsymbol{\alpha}_n(\mathbf{r}_j)$ is replaced with $\boldsymbol{\theta}_n(\mathbf{r}_j)$ in (13) and (16), respectively; $\boldsymbol{\eta}(k)$ is a zero-mean Gaussian process with $E[\boldsymbol{\eta}(k_1)\boldsymbol{\eta}(k_2)] = \delta(k_1 - k_2)\mathbf{R}$ representing the measurement noise, and $\mathbf{V}(\boldsymbol{\theta}_n(\mathbf{r}_j))$ is the vector of discrete volume fractions at \mathbf{r}_j .

For the two-compartment ICG pharmacokinetic model combined with the linear CTM map, the explicit form of (21) and (23) are given by

$$\begin{bmatrix} C_e(\mathbf{r}_j, k+1) \\ C_p(\mathbf{r}_j, k+1) \end{bmatrix} = \begin{bmatrix} \tau_{11}(\mathbf{r}_j) & \tau_{12}(\mathbf{r}_j) \\ \tau_{21}(\mathbf{r}_j) & \tau_{22}(\mathbf{r}_j) \end{bmatrix} \begin{bmatrix} C_e(\mathbf{r}_j, k) \\ C_p(\mathbf{r}_j, k) \end{bmatrix} + \begin{bmatrix} \xi_e(\mathbf{r}_j, k) \\ \xi_p(\mathbf{r}_j, k) \end{bmatrix}, \quad k = 1, \dots, K \quad (24)$$

$$\boldsymbol{\Psi}(k) = \mathbf{W} \begin{bmatrix} v_e(\mathbf{r}_j) & v_p(\mathbf{r}_j) \end{bmatrix} \begin{bmatrix} C_e(\mathbf{r}_j, k) \\ C_p(\mathbf{r}_j, k) \end{bmatrix} + \boldsymbol{\eta}(k), \quad k = 1, \dots, K \quad (25)$$

where $\mathbf{C}(\mathbf{r}_j, k) = [C_e(\mathbf{r}_j, k) \ C_p(\mathbf{r}_j, k)]^T$, $\boldsymbol{\xi}(\mathbf{r}_j, k) = [\xi_e(\mathbf{r}_j, k) \ \xi_p(\mathbf{r}_j, k)]^T$, $\mathbf{V}(\boldsymbol{\theta}_2(\mathbf{r}_j)) = [v_e(\mathbf{r}_j) \ v_p(\mathbf{r}_j)]$, $\boldsymbol{\theta}_2(\mathbf{r}_j) =$

$[\tau_{11}(\mathbf{r}_j) \ \tau_{12}(\mathbf{r}_j) \ \tau_{21}(\mathbf{r}_j) \ \tau_{22}(\mathbf{r}_j) \ v_e(\mathbf{r}_j) \ v_p(\mathbf{r}_j)]^T$, and $\mathbf{K}(\boldsymbol{\theta}_n(\mathbf{r}_j))$ is the 2-by-2 system matrix in (24), for $j = 1, \dots, N$ and $k = 1, \dots, K$.

8) *Reconstruction of Pharmacokinetic Rate and Concentration Images from the Boundary Measurements*: The forward model in (21) and (22)/(23) forms a state-space model, (21) being the state equation and (22)/(23) being the measurement equation. In this section, we discuss the estimation of the system parameters, $\boldsymbol{\theta}_n(\mathbf{r}_j)$, and the states $\mathbf{C}_d(\mathbf{r}_j, k)$ for $j = 1, \dots, N$, from the measurements $\boldsymbol{\Psi}(k)$, $k = 1, \dots, K$ using the extended Kalman filtering (EKF) framework.

Note that both the fluorophore concentrations in different compartments, $\mathbf{C}(\mathbf{r}_j, k)$, and the system parameters, $\boldsymbol{\theta}_n(\mathbf{r}_j)$, are unknown. In this case, we estimate both the states and system parameters from measurements within the EKF framework. To do so, we regard the state equation in (21) as a non-linear equation in which the system parameters and states are combined to form the new states of the non-linear equation. We then iteratively linearize the non-linear state equation and solve for the new unknown states using the EKF framework. This approach requires use of temporal prior models on $\boldsymbol{\theta}_n(\mathbf{r}_j)$. We describe one such model in the following subsection.

9) *A priori Model for Pharmacokinetic-rates and Volume Fractions*: To impose a temporal prior model on $\boldsymbol{\theta}_n(\mathbf{r}_j)$, we extend our notation to $\boldsymbol{\theta}_n(\mathbf{r}_j, k)$, $k = 1, \dots, K$. Note that $\boldsymbol{\theta}_n(\mathbf{r}_j, k)$ is a vector containing pharmacokinetic-rates and volume fractions at location $\mathbf{r}_j \in \Omega$ and time $k\Delta$. For each element, $\tilde{\theta}_n(\mathbf{r}_j, k)$, of the vector $\boldsymbol{\theta}_n(\mathbf{r}_j, k)$, we impose the following dynamic model:

$$\tilde{\theta}_n(\mathbf{r}_j, k+1) = \tilde{\theta}_n(\mathbf{r}_j, k) + \tilde{\zeta}_1(\mathbf{r}_j, k) \quad (26)$$

where $\tilde{\zeta}_1(\mathbf{r}_j, k)$ is a zero-mean Gaussian process with $E[\tilde{\zeta}_1(\mathbf{r}_1, k_1)\tilde{\zeta}_1(\mathbf{r}_2, k_2)] = \delta(\mathbf{r}_1 - \mathbf{r}_2)\delta(k_1 - k_2)z_1$, $z_1 > 0$.

Note that $\boldsymbol{\theta}_n(\mathbf{r}_j)$ is modeled as a time-independent parameter, and the model in (26) relates $\tilde{\theta}_n(\mathbf{r}_j, k+1)$ and $\tilde{\theta}_n(\mathbf{r}_j, k)$ with an all-pass filter. If, on the other hand, $\boldsymbol{\theta}_n(\mathbf{r}_j)$ is time-dependent, a different filter can be chosen based on *a priori* physiological information and/or robustness considerations.

In addition to the temporal prior, we impose a spatial smoothing prior on $\boldsymbol{\theta}_n(\mathbf{r}_j, k)$ to improve the robustness of the reconstruction with respect to measurement noise and to incorporate *a priori* physiological information into image reconstruction. This model is given as

$$\tilde{\theta}_n(\mathbf{r}_j, k) = \sum_{l=1(j_l \neq j)}^M \tilde{\beta}_l \tilde{\theta}_n(\mathbf{r}_{j_l}, k) + \tilde{\zeta}_2(\mathbf{r}_j, k), \quad j = 1, \dots, N \quad (27)$$

where j_l , $l = 1, \dots, M$ ($j_l \neq j$) are the indices of the voxels in the neighborhood of the j^{th} voxel; $\tilde{\beta}_l$, $l = 1, \dots, M$

are the spatial weighting coefficients, which may be different for each pharmacokinetic-rate or volume fraction image; and $\tilde{\zeta}_2(\mathbf{r}_j, k)$, is a zero-mean Gaussian process with $E[\tilde{\zeta}_2(\mathbf{r}_1, k_1)\tilde{\zeta}_2(\mathbf{r}_2, k_2)] = \delta(\mathbf{r}_1 - \mathbf{r}_2)\delta(k_1 - k_2)z_2$, $z_2 > 0$.

The weighting coefficients $\tilde{\beta}_l$ may be spatially varying and can be chosen based on a variety of physiological information, i.e., tumor location, size or shape. In our numerical simulations and *in vivo* data processing, we assumed that no such specific information about the tumor is available and used equal weights, i.e., $\tilde{\beta}_l = 1/M$. This choice imposes an isotropic smoothing on the $\tilde{\theta}_n(\mathbf{r}_j, k)$ estimates.

Inserting the right-hand side of (27) for $\tilde{\theta}_n(\mathbf{r}_j, k)$ in (26), we obtain the following spatio-temporal model for each entry $\tilde{\theta}_n(\mathbf{r}_j, k)$ of the vector $\theta_n(\mathbf{r}_j, k)$:

$$\tilde{\theta}_n(\mathbf{r}_j, k+1) = \sum_{l=1(j_i \neq j)}^M \tilde{\beta}_l \tilde{\theta}_n(\mathbf{r}_{j_l}, k) + \tilde{\zeta}(\mathbf{r}_j, k), \quad k = 1, \dots, K, \quad j = 1, \dots, N, \quad (28)$$

where $\tilde{\zeta}(\mathbf{r}_j, k)$ is a zero-mean Gaussian process with $E[\tilde{\zeta}(\mathbf{r}_1, k_1)\tilde{\zeta}(\mathbf{r}_2, k_2)] = \delta(\mathbf{r}_1 - \mathbf{r}_2)\delta(k_1 - k_2)z$, $z > 0$, and z is a function of z_1 and z_2 . Figure ?? illustrates the resulting neighborhood system for 2D images for $M = 4$.

Note that it is possible to develop an alternative spatio-temporal neighborhood system taking into account the 4D nature of the parameter space.

To simplify our notation, we express (28) in vector notation for all entries of the vector $\theta_n(\mathbf{r}_j, k)$ as follows:

$$\theta_n(\mathbf{r}_j, k+1) = \beta_j(\theta_n(\mathbf{r}_{j_1}, k), \dots, \theta_n(\mathbf{r}_{j_M}, k)) + \varsigma(\mathbf{r}_j, k), \quad k = 1, \dots, K, \quad j = 1, \dots, N, \quad (29)$$

where β_j is a vector-valued linear function of $\theta_n(\mathbf{r}_{j_l}, k)$, $l = 1, \dots, M$ as defined in (28) and $\varsigma(\mathbf{r}_j, k)$ is formed by concatenating the $\tilde{\zeta}(\mathbf{r}_j, k)$ into a column vector. It is a zero-mean Gaussian process with $E[\varsigma(\mathbf{r}_1, k_1)\varsigma(\mathbf{r}_2, k_2)] = \delta(\mathbf{r}_1 - \mathbf{r}_2)\delta(k_1 - k_2)\mathbf{Z}_1$.

10) Estimation of Pharmacokinetic-Rate Images by Extended Kalman Filtering: Our objective is to estimate the fluorophore concentration images in different compartments, and pharmacokinetic-rate images. To do so, we first concatenate the concentration vectors $\mathbf{C}(\mathbf{r}_j, k)$ and the parameter vectors $\theta_n(\mathbf{r}_j, k)$ for all voxels, $j = 1, \dots, N$ and form the following vectors:

$$\mathbf{C}(k) = \begin{bmatrix} \mathbf{C}^T(\mathbf{r}_1, k) & \dots & \mathbf{C}^T(\mathbf{r}_N, k) \end{bmatrix}^T, \\ \theta_n(k) = \begin{bmatrix} \theta_n^T(\mathbf{r}_1, k) & \dots & \theta_n^T(\mathbf{r}_N, k) \end{bmatrix}^T.$$

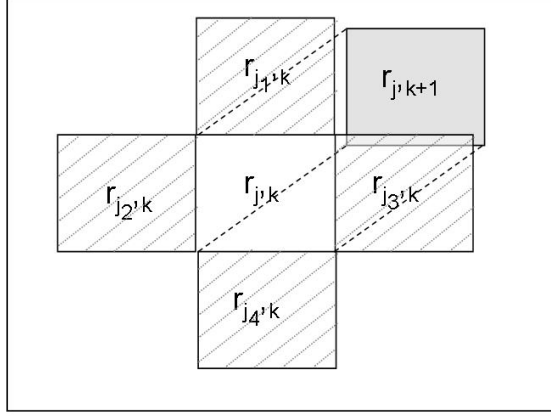


Fig. 3. An illustration of the spatio-temporal neighborhood system for 2-D pharmacokinetic-rate and volume fraction images for $M=4$. Based on the model in (28) to (30) the neighborhood of the voxel at $r_{j,k+1}$ (gray square) is given by the voxels at $r_{j1,k}$, $r_{j2,k}$, $r_{j3,k}$, and $r_{j4,k}$ denoted by gray-dashed squares.

Next, we concatenate the vectors $\mathbf{C}(k)$ and $\boldsymbol{\theta}_n(k)$ and form the new state-space model based on (21) and (29).

$$\begin{bmatrix} \mathbf{C}(k+1) \\ \boldsymbol{\theta}_n(k+1) \end{bmatrix} = \begin{bmatrix} \mathbf{K}(\boldsymbol{\theta}_n(k))\mathbf{C}(k) \\ \boldsymbol{\beta}(\boldsymbol{\theta}_n(k)) \end{bmatrix} + \begin{bmatrix} \boldsymbol{\xi}(k) \\ \boldsymbol{\varsigma}(k) \end{bmatrix} \quad (30)$$

$$\boldsymbol{\Psi}(k) = \begin{bmatrix} \mathbf{F}(\mathbf{V}(\boldsymbol{\theta}_n(k))\mathbf{C}(k)) & 0 \end{bmatrix} \begin{bmatrix} 1 \\ \boldsymbol{\theta}_n(k) \end{bmatrix} + \boldsymbol{\eta}(k) \quad (31)$$

$$\boldsymbol{\Psi}(k) = \begin{bmatrix} \ln 10 \epsilon_x \mathbf{WV}(\boldsymbol{\theta}_n(k))\mathbf{C}(k) & 0 \end{bmatrix} \begin{bmatrix} 1 \\ \boldsymbol{\theta}_n(k) \end{bmatrix} + \boldsymbol{\eta}(k), \quad k = 1, \dots, K \quad (32)$$

where

$$\begin{aligned} \mathbf{K}(\boldsymbol{\theta}_n(k))\mathbf{C}(k) &= \begin{bmatrix} \mathbf{K}(\boldsymbol{\theta}_n(\mathbf{r}_1, k))\mathbf{C}(\mathbf{r}_1, k) & \dots & \mathbf{K}(\boldsymbol{\theta}_n(\mathbf{r}_N, k))\mathbf{C}(\mathbf{r}_N, k) \end{bmatrix}^T \\ \boldsymbol{\beta}(\boldsymbol{\theta}_n(k)) &= \begin{bmatrix} \boldsymbol{\beta}_1(\boldsymbol{\theta}_n(\mathbf{r}_1, k), \dots) & \dots & \boldsymbol{\beta}_N(\boldsymbol{\theta}_n(\mathbf{r}_N, k), \dots) \end{bmatrix}^T \\ \mathbf{F}(\mathbf{V}(\boldsymbol{\theta}_n(k))\mathbf{C}(k)) &= \begin{bmatrix} \mathbf{F}(\mathbf{V}(\boldsymbol{\theta}_n(\mathbf{r}_1, k))\mathbf{C}(\mathbf{r}_1, k)) & \dots & \mathbf{F}(\mathbf{V}(\boldsymbol{\theta}_n(\mathbf{r}_N, k))\mathbf{C}(\mathbf{r}_N, k)) \end{bmatrix}^T \\ \boldsymbol{\xi}(k) &= \begin{bmatrix} \boldsymbol{\xi}(\mathbf{r}_1, k) & \dots & \boldsymbol{\xi}(\mathbf{r}_N, k) \end{bmatrix}^T \\ \boldsymbol{\varsigma}(k) &= \begin{bmatrix} \boldsymbol{\varsigma}(\mathbf{r}_1, k) & \dots & \boldsymbol{\varsigma}(\mathbf{r}_N, k) \end{bmatrix}^T \end{aligned} \quad (33)$$

where $\boldsymbol{\xi}(k)$ and $\boldsymbol{\varsigma}(k)$ are zero-mean Gaussian processes with covariance matrices \mathbf{Q} and \mathbf{Z} , respectively. $\boldsymbol{\eta}(k)$ is the zero-mean Gaussian process with covariance matrix \mathbf{R} as defined before.

Note that although β is linear in $\theta_n(\mathbf{r}_j, k)$, $j = 1, \dots, N$, (30) is non-linear in new states. Furthermore, the state equation (30) is not block diagonal.

We next utilize the EKF machinery to estimate the fluorophore concentration images in different compartments and pharmacokinetic-rates based on (30) to (33). Table I tabulates the steps of the EKF algorithm. The terms in Table I are defined as follows: $\hat{\mathbf{C}}(k|k-1)$ and $\hat{\boldsymbol{\theta}}_n(k|k-1)$ are the concentration and parameter estimates at time k given all the measurements up to time $k-1$, respectively. Similarly, $\hat{\mathbf{C}}(k)$ and $\hat{\boldsymbol{\theta}}_n(k)$ are the concentration and parameter estimate updates at time k , respectively. $\mathbf{P}_{k,k-1}$ denotes the error covariance propagation at time k given all the measurements up to time $k-1$; $\mathbf{P}_{k,k}$ is the error covariance update at time k . \mathbf{H}_k is the recursive Kalman gain matrix at time k and \mathbf{I} is the identity matrix. \mathbf{J}_{k-1} is the Jacobian matrix due to iterative linearization of the (30) around $\hat{\mathbf{C}}(k-1)$ and $\hat{\boldsymbol{\theta}}_n(k-1)$. $\boldsymbol{\Lambda}_{k|k-1}$ is the matrix formed by the discretized Fréchet derivatives of \mathcal{F} with respect to \mathbf{C} and $\boldsymbol{\theta}_n$ at the updates $\hat{\mathbf{C}}(k|k-1)$ and $\hat{\boldsymbol{\theta}}_n(k|k-1)$. In Table I, the EKF algorithm is presented for the non-linear case. For the linear case, the non-linear operator \mathbf{F} is simply replaced by the linear operator \mathbf{W} .

The first-order Fréchet derivative of \mathcal{F} (or $\mathcal{F}_{\mathbf{r}_d, \mathbf{r}_s}$) with respect to the fluorophore concentration a at the EKF total concentration estimate at the $(k|k-1)^{th}$ step is given by [44]–[46]

$$\begin{aligned} \partial \mathcal{F}_{\mathbf{r}_d, \mathbf{r}_s}(\delta a) = & \frac{\ln 10 \epsilon_x}{\Phi_x^{k|k-1}(\mathbf{r}_d, \mathbf{r}_s; \omega)} \left(\int_{\Omega} G_m^{k|k-1}(\mathbf{r}_d, \mathbf{r}; \omega) \Phi_x^{k|k-1}(\mathbf{r}, \mathbf{r}_s; \omega) \frac{1 - j\omega\tau(\mathbf{r})}{1 + [\omega\tau(\mathbf{r})]^2} \gamma \delta a(\mathbf{r}) d\mathbf{r} \right. \\ & - \int_{\Omega} G_m^{k|k-1}(\mathbf{r}_d, \mathbf{r}; \omega) \Phi_m^{k|k-1}(\mathbf{r}, \mathbf{r}_s; \omega) \frac{1 - j\omega\tau(\mathbf{r})}{1 + [\omega\tau(\mathbf{r})]^2} \frac{\epsilon_m}{\epsilon_x} \delta a(\mathbf{r}) d\mathbf{r} \\ & \left. - \int_{\Omega} G_{mx}^{k|k-1}(\mathbf{r}_d, \mathbf{r}; \omega) \Phi_x^{k|k-1}(\mathbf{r}, \mathbf{r}_s; \omega) \frac{1 - j\omega\tau(\mathbf{r})}{1 + [\omega\tau(\mathbf{r})]^2} \delta a(\mathbf{r}) d\mathbf{r} \right) \quad (34) \end{aligned}$$

where we define $\Phi_x^{k|k-1}(\mathbf{r}, \mathbf{r}_s; \omega)$ as the solution of (45) and (10), $\Phi_m^{k|k-1}(\mathbf{r}, \mathbf{r}_s; \omega)$ as the solution of (7) and (11), $G_m^{k|k-1}(\mathbf{r}_d, \mathbf{r}; \omega)$ as the Green's function of (7) and (11), and $G_{mx}^{k|k-1}(\mathbf{r}_d, \mathbf{r}; \omega)$ as the solution of (45) and (10) where $S(\mathbf{r}, \omega)$ in (45) is replaced by $\gamma \mu_{axf} G_m^{k|k-1}(\mathbf{r}_d, \mathbf{r}; \omega)$ given the EKF estimates of the fluorophore concentrations at different compartments at the $(k|k-1)^{th}$ step [44]. In (34), the first integral results from the right-hand side of (7), while the second and third integrals originate from the dependence of μ_{am} and μ_{ax} , respectively, on the unknown fluorophore absorption coefficient. We note that the kernels of the second and thirds integrals are much smaller than the kernel of the first integral. Therefore, the first integral in (34) dominates and the rest can be neglected. As a result, The first-order Fréchet derivative of \mathcal{F} (or $\mathcal{F}_{\mathbf{r}_d, \mathbf{r}_s}$) with respect to the fluorophore concentration a at the

TABLE I

EKF ALGORITHM FOR THE SIMULTANEOUS ESTIMATION OF FLUOROPHORE CONCENTRATION, PHARMACOKINETIC-RATE AND VOLUME FRACTION IMAGES.

| | |
|-------------------------------------|--|
| System Model | $\begin{bmatrix} \mathbf{C}(k+1) \\ \boldsymbol{\theta}_n(k+1) \end{bmatrix} = \begin{bmatrix} \mathbf{K}(\boldsymbol{\theta}_n(k))\mathbf{C}(k) \\ \beta(\boldsymbol{\theta}_n(k)) \end{bmatrix} + \begin{bmatrix} \boldsymbol{\xi}(k) \\ \varsigma(k) \end{bmatrix}$ |
| Measurement Model | $\boldsymbol{\Psi}(k) = \begin{bmatrix} \mathbf{F}(\mathbf{V}(\boldsymbol{\theta}_n(k))\mathbf{C}(k)) & 0 \end{bmatrix} \begin{bmatrix} 1 \\ \boldsymbol{\theta}_n(k) \end{bmatrix} + \boldsymbol{\eta}(k)$ |
| Initial Conditions | $\begin{bmatrix} \hat{\mathbf{C}}(1) \\ \hat{\boldsymbol{\theta}}_n(1) \end{bmatrix} = \begin{bmatrix} E(\mathbf{C}(1)) \\ \hat{\boldsymbol{\theta}}_n(1) \end{bmatrix}, \quad \mathbf{P}_{1,1} = \begin{bmatrix} Var(\mathbf{C}(1)) & 0 \\ 0 & \mathbf{Z} \end{bmatrix}$ |
| State Estimate Propagation | $\begin{bmatrix} \hat{\mathbf{C}}(k k-1) \\ \hat{\boldsymbol{\theta}}_n(k k-1) \end{bmatrix} = \begin{bmatrix} \mathbf{K}(\hat{\boldsymbol{\theta}}_n(k-1))\hat{\mathbf{C}}(k-1) \\ \beta(\hat{\boldsymbol{\theta}}_n(k-1)) \end{bmatrix}$ |
| Error Covariance Propagation | $\mathbf{P}_{k,k-1} = \mathbf{J}_{k-1}\mathbf{P}_{k-1,k-1}\mathbf{J}_{k-1}^T + \begin{bmatrix} \mathbf{Q} & 0 \\ 0 & \mathbf{Z} \end{bmatrix}$ |
| State Estimate Update | $\begin{bmatrix} \hat{\mathbf{C}}(k) \\ \hat{\boldsymbol{\theta}}_n(k) \end{bmatrix} = \begin{bmatrix} \hat{\mathbf{C}}(k k-1) \\ \beta(\hat{\boldsymbol{\theta}}_n(k k-1)) \end{bmatrix} + \mathbf{H}_k[\boldsymbol{\Psi}(k) - \mathbf{F}(\mathbf{V}(\hat{\boldsymbol{\theta}}_n(k k-1))\hat{\mathbf{C}}(k k-1))]$ |
| Error Covariance Update | $\mathbf{P}_{k,k} = [\mathbf{I} - \mathbf{H}_k\boldsymbol{\Lambda}_{k k-1}]\mathbf{P}_{k,k-1}$ |
| Kalman Gain | $\mathbf{H}_k = \mathbf{P}_{k,k-1}\boldsymbol{\Lambda}_{k k-1}^T[\boldsymbol{\Lambda}_{k k-1}\mathbf{P}_{k,k-1}\boldsymbol{\Lambda}_{k k-1}^T + \mathbf{R}]^{-1}$ |
| Definitions | $\mathbf{J}_{k-1} = \begin{bmatrix} \mathbf{K}(\hat{\boldsymbol{\theta}}_n(k-1)) & \frac{\partial}{\partial \boldsymbol{\theta}}(\mathbf{K}(\hat{\boldsymbol{\theta}}_n(k-1))\hat{\mathbf{C}}(k-1)) \\ \frac{\partial}{\partial \mathbf{C}}\beta(\hat{\boldsymbol{\theta}}_n(k-1)) & \frac{\partial}{\partial \boldsymbol{\theta}_n}\beta(\hat{\boldsymbol{\theta}}_n(k-1)) \end{bmatrix}$ |
| Non-linear Case | |
| | $\boldsymbol{\Lambda}_{k k-1} = \begin{bmatrix} \frac{\partial}{\partial \mathbf{C}}\mathbf{F}(\mathbf{V}(\hat{\boldsymbol{\theta}}_n(k k-1))\hat{\mathbf{C}}(k k-1)) & \frac{\partial}{\partial \boldsymbol{\theta}_n}\mathbf{F}(\mathbf{V}(\hat{\boldsymbol{\theta}}_n(k k-1))\hat{\mathbf{C}}(k k-1)) \end{bmatrix}$ |
| Linear Case | |
| | $\boldsymbol{\Lambda}_{k k-1} = \begin{bmatrix} \ln 10\epsilon_x \mathbf{W} \frac{\partial}{\partial \mathbf{C}}(\mathbf{V}(\hat{\boldsymbol{\theta}}_n(k k-1))\hat{\mathbf{C}}(k k-1)) & \ln 10\epsilon_x \mathbf{W} \frac{\partial}{\partial \boldsymbol{\theta}_n}(\mathbf{V}(\hat{\boldsymbol{\theta}}_n(k k-1))\hat{\mathbf{C}}(k k-1)) \end{bmatrix}$ |

EKF total concentration estimate at the $(k|k-1)^{th}$ step can be approximated by

$$\partial \mathcal{F}_{\mathbf{r}_d, \mathbf{r}_s}(\delta a) = \frac{\ln 10 \gamma \epsilon_x}{\Phi_x^{k|k-1}(\mathbf{r}_d, \mathbf{r}_s; \omega)} \int_{\Omega} G_m^{k|k-1}(\mathbf{r}_d, \mathbf{r}; \omega) \Phi_x^{k|k-1}(\mathbf{r}, \mathbf{r}_s; \omega) \frac{1 - j\omega\tau(\mathbf{r})}{1 + [\omega\tau(\mathbf{r})]^2} \delta a(\mathbf{r}) d\mathbf{r}, \quad (35)$$

Based on the assumptions *i)-iii)* in CTM map subsection, the terms in the kernel of (35) can be computed as follows: Based on the assumption *i)*, $\mu_{axe} \approx \mu_{ame}$. Furthermore, μ_{amf} and μ_{axf} are linearly dependent by (12). Thus, given the μ_{axe} reconstruction based on (45) and (10) at the k^{th} step, and μ_{amf} obtained via EKF estimates (fluorophore concentrations at different compartments and volume fractions) at the $(k|k-1)^{th}$ step, $G_m^{k|k-1}(\mathbf{r}_d, \mathbf{r}; \omega)$ can be computed using (7) and (11). Similarly, given the μ_{axe} reconstruction based on (45) and (10) at the k^{th} step, and μ_{axf} estimate obtained via the EKF estimates of fluorophore concentrations at different compartments and volume fractions at the $(k|k-1)^{th}$ step, $\Phi_x^{k|k-1}(\mathbf{r}_d, \mathbf{r}_s; \omega)$ can be computed as the solution of (45) and (10). Finally, we assume that $\frac{1-j\omega\tau(\mathbf{r})}{1+[\omega\tau(\mathbf{r})]^2}$ is known.

Note that the calculation of the Fréchet derivative can be simplified under some additional assumptions. If μ_{axe} does not vary with the slow-time variable k , and that $\mu_{amf} \ll \mu_{ame}$, then $G_m(\mathbf{r}_d, \mathbf{r}; \omega)$ can be computed with respect to μ_{axe} and remains invariant with respect to the slow-time variable k .

Using the chain rule, the first-order Fréchet derivative of $\mathcal{F}_{\mathbf{r}_d, \mathbf{r}_s}$ with respect to each element of \mathcal{C} is given by

$$\partial \mathcal{F}_{\mathbf{r}_d, \mathbf{r}_s}(\delta \mathcal{C}_i) = \frac{\ln 10 \gamma \epsilon_x}{\Phi_x^{k|k-1}(\mathbf{r}_d, \mathbf{r}_s; \omega)} \int_{\Omega} G_m^{k|k-1}(\mathbf{r}_d, \mathbf{r}; \omega) \Phi_x^{k|k-1}(\mathbf{r}, \mathbf{r}_s; \omega) \frac{1 - j\omega\tau(\mathbf{r})}{1 + [\omega\tau(\mathbf{r})]^2} \delta \mathcal{C}_i v_i(\mathbf{r}) d\mathbf{r}, \quad (36)$$

where $v_i, i = 1, 2, \dots, n$, denotes the volume fractions.

Similarly, the first-order Fréchet derivative of $\mathcal{F}_{\mathbf{r}_d, \mathbf{r}_s}$ with respect to each element of α_n is given by

$$\partial \mathcal{F}_{\mathbf{r}_d, \mathbf{r}_s}(\delta \alpha_n) = \frac{\ln 10 \gamma \epsilon_x}{\Phi_x^{k|k-1}(\mathbf{r}_d, \mathbf{r}_s; \omega)} \int_{\Omega} G_m^{k|k-1}(\mathbf{r}_d, \mathbf{r}; \omega) \Phi_x^{k|k-1}(\mathbf{r}, \mathbf{r}_s; \omega) \frac{1 - j\omega\tau(\mathbf{r})}{1 + [\omega\tau(\mathbf{r})]^2} \delta v_i(\mathbf{r}) \mathcal{C}_i(\mathbf{r}) d\mathbf{r}. \quad (37)$$

Note that α_n contains both pharmacokinetic-rate and volume fraction parameters. However, the Fréchet derivative of \mathcal{F} with respect to pharmacokinetic-rates is zero since \mathcal{F} depends only on the volume fractions.

In our numerical simulations, we used finite elements with piece-wise linear first-order Lagrange polynomials to discretize the domain Ω and thus to discretize the Fréchet derivatives given in (36) and (37).

The EKF algorithms for the estimation of concentration and parameter images are different for the linear and non-linear measurement models given in (13) and (16). When the linearized measurement model (16) is employed, the operator \mathcal{W} is assumed to be constant throughout the dynamic update of the fluorophore concentration. This leads to the inherent assumption that the dynamic changes in the fluorophore concentration can be modeled as a perturbation on the endogenous chromophore concentrations. For the non-linear measurement model (13), on the

other hand, the Fréchet derivative is updated at every iteration of the EKF algorithm based on the $(k|k-1)^{th}$ update of the concentration and volume fraction estimates. While computationally more intense, the EKF algorithm based on the non-linear measurement model eliminates the limiting assumption of restricting the dynamic changes to perturbations from a constant endogenous chromophore concentration.

11) Convergence and Initialization of EKF: The convergence properties of the EKF has been studied in the literature [49], [50], [53]–[55]. In general for the joint estimation of parameters and states the estimates may be biased or divergent.

The main cause of divergence in EKF is due to the fact that there is no coupling term between \mathbf{H}_k and $\boldsymbol{\theta}_n$ [50], [53]. This lack of coupling between \mathbf{H}_k and $\boldsymbol{\theta}_n$ may lead to divergence of the estimates. To overcome this issue, for improved asymptomatic convergence properties, the EKF algorithm can be modified using the proposed method given in [53]. However, as stated in [50] and [53] this modification imposes a high computational load to the algorithm. Hence, in practical applications with large size matrices, instead of using the proposed method, manual adjustments of the noise covariances matrices \mathbf{Z} , \mathbf{Q} , and \mathbf{R} can be used to improve the converge properties of the EKF which is called the “tuning of the filter” [50], [53]. In our work, as proposed in [50] and [53], we regard the initial values of these matrices (which are nothing but the multiples of identity matrix, i.e., $\sigma\mathbf{I}$) as tuning parameters.

The asymptotic convergence-rate of EKF depends the initialization of $\boldsymbol{\theta}_n$ and \mathbf{C} , and proper selection of the noise covariance matrices \mathbf{Z} , \mathbf{Q} , and \mathbf{R} [49], [50], [53]. The covariance matrix \mathbf{R} is the most important term that controls the convergence-rate of the EKF [49]. It has been shown in [49] that with an appropriate choice of the covariance matrix \mathbf{R} , the asymptotic convergence-rate of the EKF may be improved significantly.

In this work, we change the values of covariance matrices \mathbf{R} , \mathbf{Q} and \mathbf{Z} matrices and choose the values that lead to minimum norm of error covariance matrix within biological limits.

Theoretically, the state estimates can be initialized at the expected value of the ICG concentrations, i.e. $E[\mathbf{C}(1)]$. One approach to the initialization of the parameters is to utilize the state-space presentation given in (21)–(23). Since $E(\boldsymbol{\Psi}(1)) = \epsilon\mathbf{W}\mathbf{V}_d(\boldsymbol{\theta}_n(1))E[\mathbf{C}(1)]$, $\boldsymbol{\Psi}(1) - \epsilon\mathbf{W}\mathbf{V}(\boldsymbol{\theta}_n(1))E[\mathbf{C}(1)]$ is a zero-mean random vector. If we express the variance of the measurement $\boldsymbol{\Psi}(1)$ in terms of the variance of $\mathbf{C}(1)$ using the measurement model in (23), and solve for $\boldsymbol{\theta}_n$, we get the estimate $\hat{\boldsymbol{\theta}}_n(1)$ as the most appropriate value for initialization.

In this work, we change the initial values of concentrations, pharmacokinetic-rates, volume fractions within biological limits and pick the values that lead to minimum norm of error covariance matrix.

In depth discussion on the convergence properties of the EKF, and the initialization of parameters and covariance matrices can be found in [37], [49], [50], [53]–[55].

12) Computational Complexity of the EKF based Reconstruction Algorithms: In this subsection, we derive the computational complexity of the EKF based direct reconstruction algorithms based on the linear and non-linear models in (31) and (32) under the assumptions outlined in sections VI-A and VI-B. We next derive the computational complexity of the EKF based voxel-by-voxel pharmacokinetic-rate and concentration image reconstruction algorithm that we introduced in [41] and compare it with the computational complexity of the algorithms introduced in this paper.

The computational complexity of one recursion of the EKF is $\mathcal{O}(2m^2h) + \mathcal{O}(2mh^2) + \mathcal{O}(m^3) + \mathcal{O}(h^3)$, where m denotes the dimension of the measurement vector, and h denotes the dimension of the states [56].

For the EKF based direct reconstruction algorithm based on the linear measurement model (32), the number of states h is $n(n+2)N$, where n is the number of compartments, and N is the number of voxels. Typical values of n , K , N , and m are tabulated in Table VI. Thus, assuming that $2m^2n(n+2) \sim N^2$, $2mn^2(n+2)^2 \sim N^{3/2}$, $m^3 \sim N^{5/2}$, and $n^3(n+2)^3 \sim N$, the computational complexity of direct reconstruction algorithm for one recursion of the EKF algorithm is given by $\mathcal{O}(N^3) + \mathcal{O}(N^3) + \mathcal{O}(N^2) + \mathcal{O}(N^4)$, which is dominated by the $\mathcal{O}(N^4)$ term. For the non-linear measurement model (31), the Fréchet derivative of \mathcal{F} has to be computed at every recursion, which has a computational complexity of $\mathcal{O}(N_d N^2 + N_s N^2)$ [61]. Assuming that N_d and $N_s \ll N^2$, the computational complexity of every recursion of the EKF algorithm using the non-linear measurement model is $\mathcal{O}(N^4)$. Hence, the EKF based direct reconstruction algorithms using either the non-linear or linear measurement model have the computational complexity of $\mathcal{O}(N^4)$.

TABLE II

POSSIBLE RANGE OF VALUES OF THE PARAMETERS USED FOR COMPLEXITY ANALYSIS

| | |
|---------------------------------|-----------|
| Number of compartments, n | 2 – 4 |
| Total number of voxels, N | 576 – 649 |
| Size of measurement vector, m | 128 – 256 |
| Total number of steps, K | 50 – 100 |

For the EKF based voxel-by-voxel construction algorithm that we introduced in [41], the number of states, h , is $n(n+2)$ and $m = 1$. In this algorithm, the absorption coefficient images are reconstructed prior to pharmacokinetic-rate images. In general, the computational complexity of this step is $\mathcal{O}(N^3 K)$ for a linear reconstruction algorithm,

where K is the number of slow-time steps. Assuming that, $2n(n+2) \sim N^{1/2}$, $2n^2(n+2)^2 \sim N$, and $n^3(n+2)^3 \sim N^{3/2}$, the computational complexity of the voxel-by-voxel reconstruction algorithm for one recursion of the EKF is given by $\mathcal{O}(N^3K) + \mathcal{O}(N^{3/2}) + \mathcal{O}(N^2) + \mathcal{O}(N) + \mathcal{O}(N^{5/2})$, which is dominated by the $\mathcal{O}(N^3K)$ term. For the non-linear measurement model, the computational complexity of reconstructing the absorption images of fluorophore is $\mathcal{O}(N^3Kp)$ where p is the number of iterations performed in Born-type non-linear iterative reconstruction schemes. Clearly, if the number of slow-time samples multiplied with the iteration number, Kp , is of higher order than the total number of voxels, N , then, the computational complexity of the direct reconstruction algorithm is smaller than that of the voxel-by-voxel algorithm. However, for the current dynamic imaging systems, Kp , is smaller than N . On the other hand, the EKF based direct reconstruction algorithms offer a number advantages that may justify such an increase in computational requirements.

The algorithm stores three covariance matrices \mathbf{Q} , \mathbf{R} , and \mathbf{Z} with size $nN \times nN$, $m \times m$, and $n(n+1)N \times n(n+1)N$, respectively. For each iteration, the algorithm stores a measurement matrix of size $m \times 1$, stores and updates the error covariance matrix, \mathbf{P} , of size $n(n+2)N \times n(n+2)N$, Kalman gain matrix, \mathbf{H} , of size $n(n+2)N \times m$, \mathbf{A} matrix of size $m \times n(n+2)N$, and \mathbf{J} matrix of size $n(n+2)N \times n(n+2)N$. The algorithm also stores all the updates of the concentrations and parameters which are of size $n(n+2)N \times 1$.

13) Numerical Simulations and Pharmacokinetic-rate Image Reconstruction from in vivo Breast Data: We tested the performance of our approach using simulated data, and *in vivo* data acquired from three patients with breast tumor. We first present the numerical simulations and compare the performance of direct reconstruction algorithm (for both the linear and non-linear measurement models) with that of voxel-by-voxel reconstruction algorithm presented in [41]. Next, we present the pharmacokinetic-rate images reconstructed from *in vivo* breast data.

14) Numerical Simulations: We performed a simulation study using the two-compartment model for ICG pharmacokinetics and the light propagation model. Using physiologically relevant values for the pharmacokinetic rates, k_{in} , k_{out} , k_{elm} , and volume fractions, v_e , v_p , given in Table III, we simulated the boundary measurements, $\Psi(k)$, $k = 1, \dots, K$, for a tissue-like 2-D phantom. The maximum transition rates of k_{in} and k_{out} are simulated at the center of the image and smoothly decreased towards the boundaries based on the results given in [38], [41]. The fluorescence quantum efficiency and lifetime of ICG are assumed to be constant and set to 0.016 and 0.56 ns, respectively. The modulation frequency was set to 300 MHz. The physical dimension of the 2-D phantom was chosen 6 cm by 6 cm. The image domain was discretized into 24 by 24 pixels each of size 0.25cm by 0.25 cm. As a prior model, we employed a four-pixel neighborhood model $\beta = 1/4$ due to rectangular nature of the geometry.

24 sources and 24 detectors along the boundary of the phantom were used to generate simulated data as shown in Figure 4. The values of k_{elm} , v_e and v_p in Table III correspond to the average values of the heterogeneities from the 24 by 24 pixel phantom images.

TABLE III
PHYSIOLOGICAL VALUES FOR NUMERICAL SIMULATIONS

| | |
|----------------------------|---------------------------|
| Maximum value of k_{in} | 0.037 sec^{-1} |
| Maximum value of k_{out} | 0.029 sec^{-1} |
| k_{elm} | 0.0054 sec^{-1} |
| v_e | 0.3 |
| v_p | 0.04 |
| μ_{axe} | 0.05 cm^{-1} |
| μ_{sx} | 8 cm^{-1} |

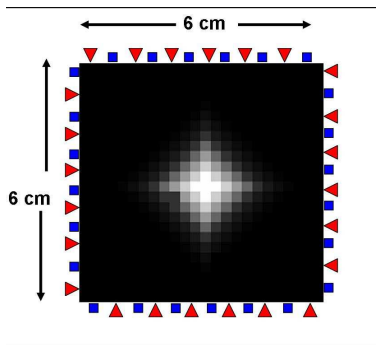


Fig. 4. The source detector configuration for the numerical phantom. Rectangular shapes present the detectors and the triangular ones present the sources.

We tested the EKF based direct reconstruction algorithm based on both the non-linear (31) and linear (32) measurement models. In the linear model, we computed the matrix \mathbf{W} based on the background $\mu_{ax,m}$, and assumed that it is constant throughout the dynamic update of the fluorophore concentrations. For the non-linear model, we updated the Fréchet derivative of \mathbf{F} , at every iteration of the EKF algorithm based on the $(k|k-1)^{th}$ update of the concentration and volume fraction estimates as defined in (35)-(37). In the update of the Fréchet derivatives, we assumed that μ_{axe} is constant, and $\mu_{ame} \gg \mu_{amf}$. As a result, we computed $G_m(\mathbf{r}_d, \mathbf{r}; \omega)$ once, and did not update at every recursion, but updated the $\Phi_x^{k|k-1}(\mathbf{r}, \mathbf{r}_s; \omega)$ at every recursion.

Fig. 5a and Fig. 6a show the phantom images of the pharmacokinetic-rates k_{in} and k_{out} . Fig. 5b and Fig. 6b display the corresponding k_{in} and k_{out} images reconstructed by the EKF based direct reconstruction algorithm with

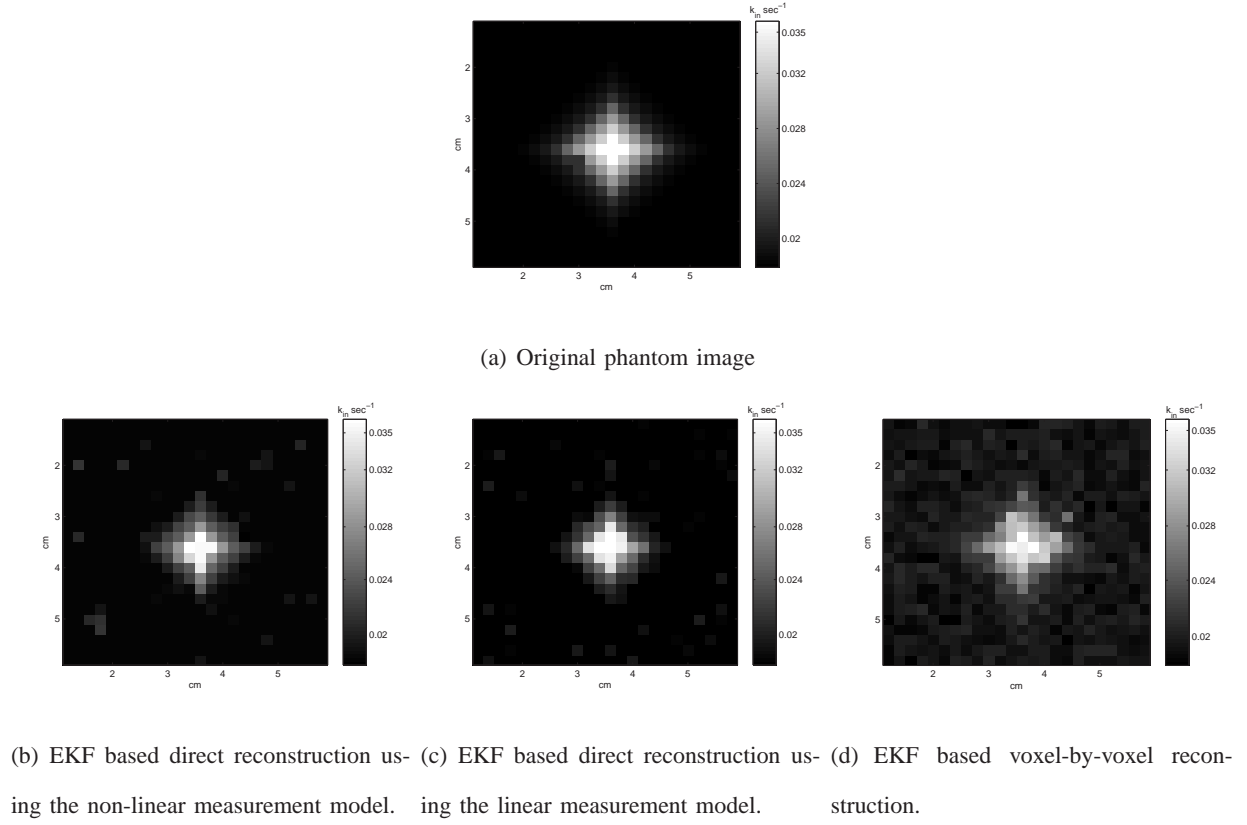


Fig. 5. Pharmacokinetic-rate images of k_{in} for three different reconstruction algorithms.

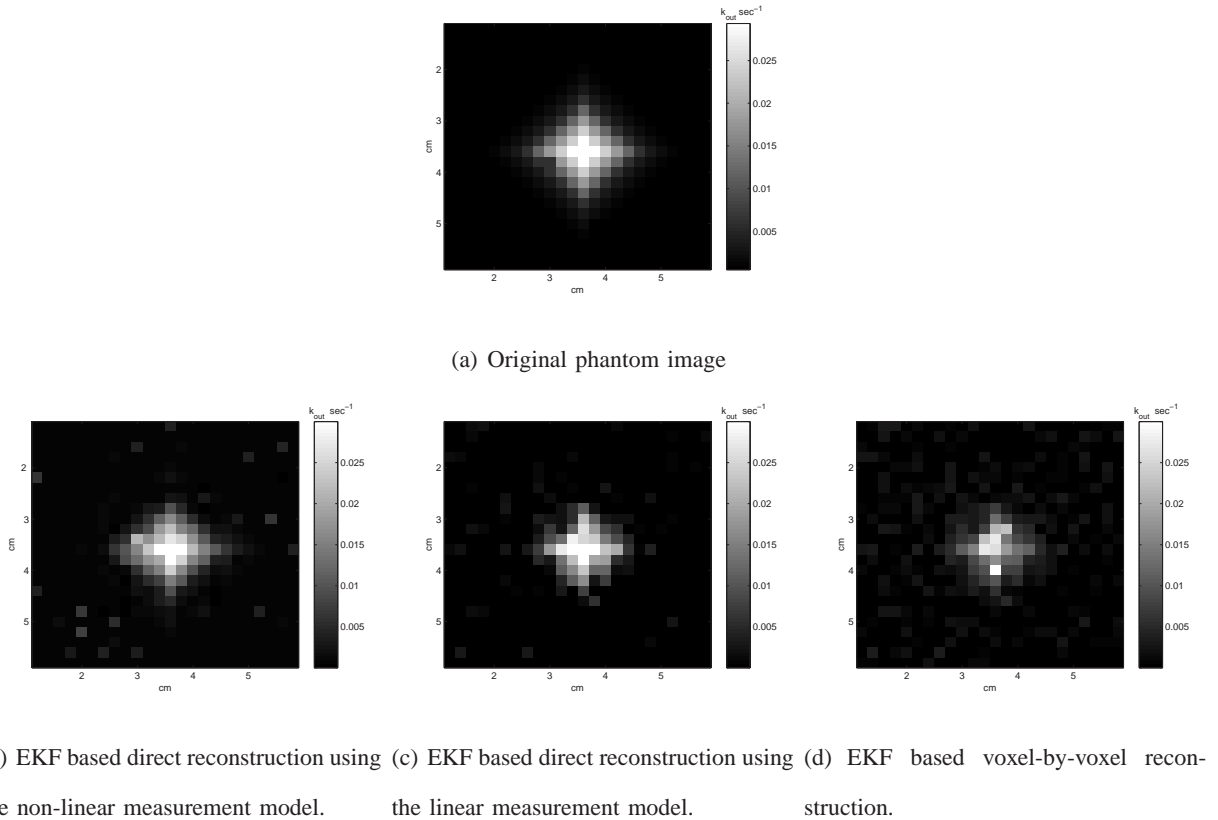


Fig. 6. Pharmacokinetic-rate images of k_{out} for three different reconstruction algorithms.

the non-linear measurement model. Fig. 5c and Fig. 6c display the corresponding k_{in} and k_{out} images obtained by the direct reconstruction with the linear measurement model. Figures 5d and 6d display the corresponding k_{in} and k_{out} images using the voxel-by-voxel algorithm introduced in [41]. We observe that there is a good agreement between the true and the estimated images in terms of localization of the heterogeneities. In all three reconstruction algorithms, the center of the heterogeneity is consistent with the ones in the original phantom images. Visual inspection of reconstructed images shows that the EKF based direct reconstruction algorithm leads to smoother and less noisy images than that of the voxel-by-voxel reconstruction.

To quantify the difference between the reconstructed and true images, we used the normalized mean square error (NMSE):

$$\text{NMSE} = 20\log_{10} \frac{\|X_{recon} - X_{true}\|^2}{\|X_{true}\|^2}.$$

Note that $\text{NMSE} = -\text{SNR}$ where SNR stands for signal-to-noise-ratio. Table ?? tabulates the NMSE values for k_{in} and k_{out} images for three different reconstruction methods. For the direct reconstruction algorithm with the non-linear measurement model, the NMSE for k_{in} and k_{out} images are -19.77 dB and -18.49 dB, respectively. For the direct reconstruction algorithm with the linear measurement model, the NMSE for k_{in} and k_{out} images are -18.45 dB and -17.65 dB, respectively. Finally, for the voxel-by-voxel construction algorithm, the error for k_{in} and k_{out} images are -16.88 dB and -15.90 dB, respectively.

Next, we studied the effect of measurement noise in the performance of the direct reconstruction algorithm and compared it with that of the voxel-by-voxel algorithm. We added zero-mean white Gaussian noise with standard deviation equal to 5% to 15% of the average of the measurements with a step size of 2.5%. We generated 15 realizations of the Gaussian noise at each level and determined NMSE based on 15 reconstructions. Fig. 7(a) and (b) show the NMSE versus the measurement noise for 5 different noise levels for k_{in} and k_{out} images, respectively. Clearly, the NMSE in the reconstructed k_{in} and k_{out} images increases as the measurement noise increases. The pharmacokinetic-rate images obtained with the direct reconstruction algorithm (both linear and non-linear cases) together with the *a priori* information results in smaller error values as compared to the voxel-by-voxel reconstruction algorithm. Moreover, the direct reconstruction algorithm using the non-linear measurement model resulted in smaller error values as compared to the direct reconstruction algorithm with the linear measurement model.

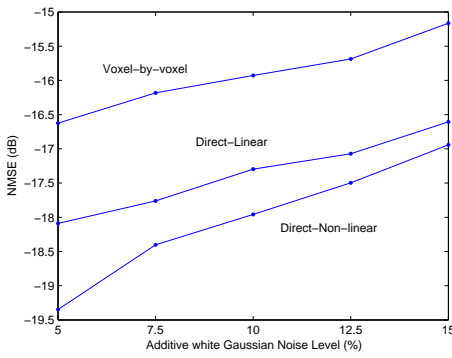
We also studied, the effect of initialization of the covariance matrices \mathbf{R} , \mathbf{Q} , and \mathbf{Z} in the reconstructed pharmacokinetic-rate images. We chose the initial values of concentrations, pharmacokinetic-rates, volume fractions and \mathbf{R} , \mathbf{Q} and \mathbf{Z} matrices that lead to minimum norm of error covariance matrix within biological limits. Let $\mathbf{R} = \alpha_1 \mathbf{I}$, $\mathbf{Q} = \alpha_2 \mathbf{I}$, and

$\mathbf{Z} = \alpha_3 \mathbf{I}$, where \mathbf{I} is an identity matrix, and $\alpha = [\alpha_1 \ \alpha_2 \ \alpha_3]$. Table IV presents the norm of the error covariance matrix for k_{in} and k_{out} for different values of α using both linear and non-linear direct reconstruction algorithms. The optimal α is $[0.012 \ 0.051 \ 0.0025]$. We observed that optimal α results in visually better quality images than that of other α values.

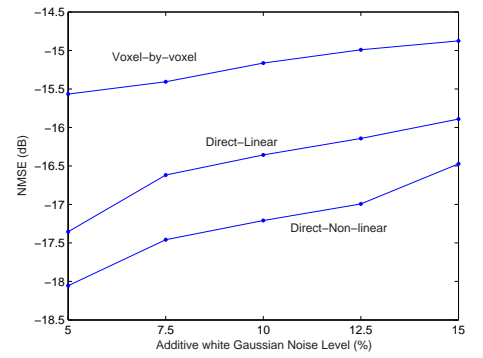
TABLE IV
NORM OF THE ERROR COVARIANCE MATRIX, $\alpha = [0.012 \ 0.051 \ 0.0025]$

| | LINEAR RECON | NON-LINEAR RECON |
|-------------|--------------|------------------|
| $\alpha/10$ | 224.54 | 215.93 |
| $\alpha/5$ | 152.40 | 143.36 |
| $\alpha/2$ | 104.34 | 97.34 |
| α | 77.18 | 63.45 |
| 2α | 107.91 | 95.39 |
| 3α | 148.29 | 140.70 |

In general, the improvements in the direct reconstructed images can be attributed to; (i) the use of spatio-temporal prior model for the pharmacokinetic-rate images which leads to more robust algorithms and smoother images; (ii) efficient use of the inherent temporal correlations in NIR measurements by combining spatial (photon propagation) and temporal (compartmental) models.



(a)



(b)

Fig. 7. NMSE vs measurement noise levels for the direct and voxel-by-voxel reconstruction algorithms (a) k_{in} images, (b) k_{out} images.

15) *Pharmacokinetic-rate Images from in vivo Breast Data:* We used *in vivo* breast data acquired by a continuous wave (CW) NIR imaging apparatus to reconstruct the pharmacokinetic-rate images of ICG. The apparatus has 16 light sources and 16 detectors located on a circular holder at an equal distance from each other with 22.5 degrees

apart. Sources and detectors were collocated and were in the same plane. The breast was arranged in a pendular geometry with the source-detector probes gently touching its surface. A set of measurement for each source was collected at every 500 ms. The total time for the whole scan of the breast including 16 sources and 16 detectors was 8.8 seconds. The detectors used the same positions as the sources to collect the light originating from one source at a time. Only the measurements from the farthest 11 detectors with high SNR were used in image reconstruction. This resulted in approximately 115 viable measurements out of 256 measurements collected at each time instant. ICG was injected intravenously by bolus with a concentration of 0.25 mg per kg of body weight. Data acquisition started before the injection of ICG and continued for 10 minutes.

Three patients with different tumor types were included in the study. First case, Case 1, is a fibroadenoma, which corresponds to a mass estimated to be 1–2 cm in diameter, and located 1 cm below the skin. Second case, Case 2, is an adenocarcinoma corresponding to a tumor estimated to be 2–3 cm in diameter, and located approximately 2 cm below the skin. Third case, Case 3, is an invasive ductal carcinoma, which corresponds to a mass estimated to be 3–4 cm in diameter, and located 2 cm below the skin. Diagnostic information was obtained by biopsy after data acquisition. A more detailed explanation of the apparatus, the data collection protocol and tumor information can be found in [40].

We used a two-compartment model for the ICG pharmacokinetics as described in (3), (4) and (5). We combined the two-compartment model with the linear measurement model (16). For computational tractability, we used a 2-D diffusion model for both direct and voxel-by-voxel reconstruction. (See [68]–[71] for a detailed discussion of errors resulting from using 2-D diffusion model for 3-D light propagation in breast tissue.) We made the following simplifying assumptions: The diffusion coefficient D_x is constant and is equal to 0.0416 cm. The endogenous absorption coefficient at the excitation and emission wavelength are approximately the same, $\mu_{ame} \approx \mu_{axe}$. Thus, we determined G_m^e and ϕ_x^e based on (7) using the excitation measurements prior to ICG injection. We next set the left hand side of (16) to excitation measurements after the ICG injection and reconstructed two-dimensional ICG pharmacokinetic-rate and concentration images based on (30) and (32). The resulting measurement model is known as the differential diffuse optical tomography model. A more detailed description of the model can be found in [40], [41], [62]. As a prior model, we employed a six-pixel neighborhood model $\beta = 1/6$ due to circular nature of the geometry. The initial values for the pharmacokinetic-rates and covariance matrices were regarded as tuning parameters and the values that lead to minimum norm error covariance matrix were chosen as initial values.

The resulting ICG pharmacokinetic-rate images are shown in Fig. 8, 9 and 10. The images show that there is a good

agreement with the location of the heterogeneity in the images and the physical location of the tumors. Our results show that the pharmacokinetic-rates are higher around the tumor region agreeing with the fact that permeability increases around the tumor region due to compromised capillaries of tumor vessels [63], [64]. Additionally, we reconstructed the ICG concentration images for plasma and the EES compartments. Figures 11-16 show the ICG concentration in plasma and the EES for 3 different time instants for Case 1, 2, and 3, respectively. We observed that the ICG concentrations in plasma and the EES compartments are higher around the tumors agreeing with the hypothesis that around the tumor region ICG leaks out of damaged capillaries of tumor vessels.

Although the number of available patient data is limited, our results indicate that the pharmacokinetic-rate imaging may provide new approaches to evaluate and improve breast cancer diagnosis, staging, and treatment monitoring. Such approaches may include extraction of new quantitative features from ICG pharmacokinetic-rate images, and statistical analysis of spatial distribution of pharmacokinetic-rates.

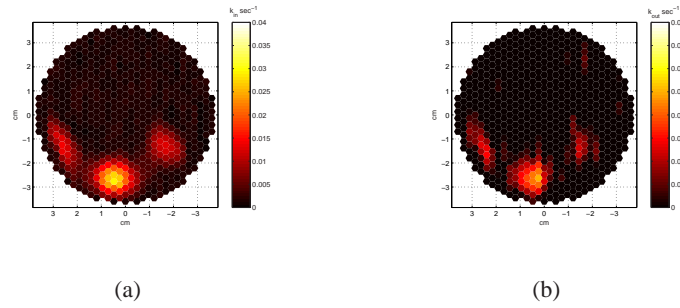


Fig. 8. Case 1: Direct reconstructed pharmacokinetic-rate images of (a) k_{in} , (b) k_{out} .

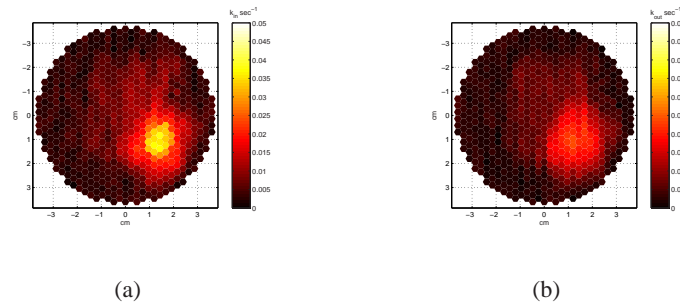


Fig. 9. Case 2: Direct reconstructed pharmacokinetic-rate images of (a) k_{in} , (b) k_{out} .

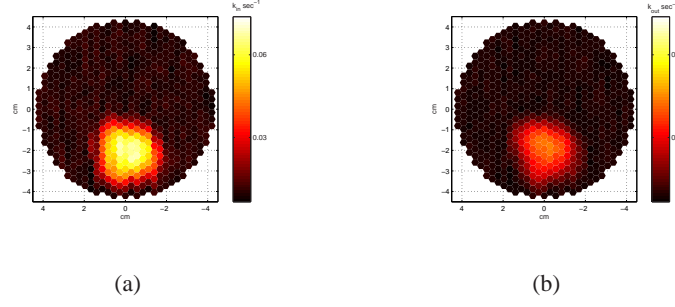


Fig. 10. Case 3: Direct reconstructed pharmacokinetic-rate images of (a) k_{in} , (b) k_{out} .

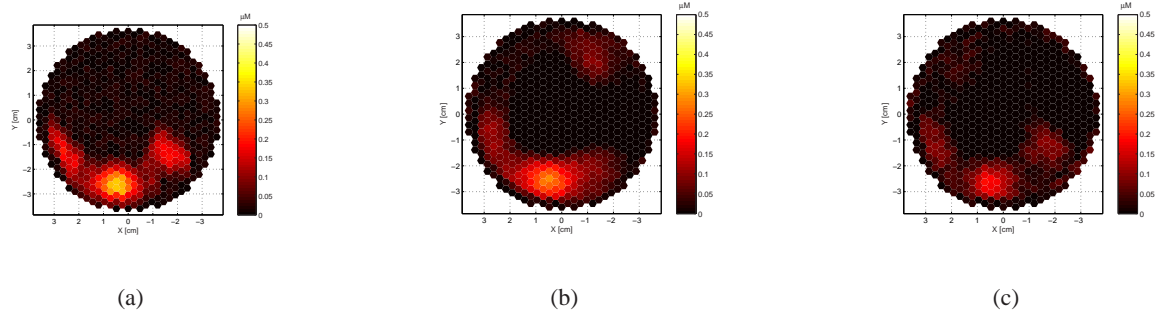


Fig. 11. Direct reconstructed ICG concentration images in plasma for Case 1 for (a) 246.4^{th} , (b) 334.4^{th} , and (c) 422.4^{th} seconds.

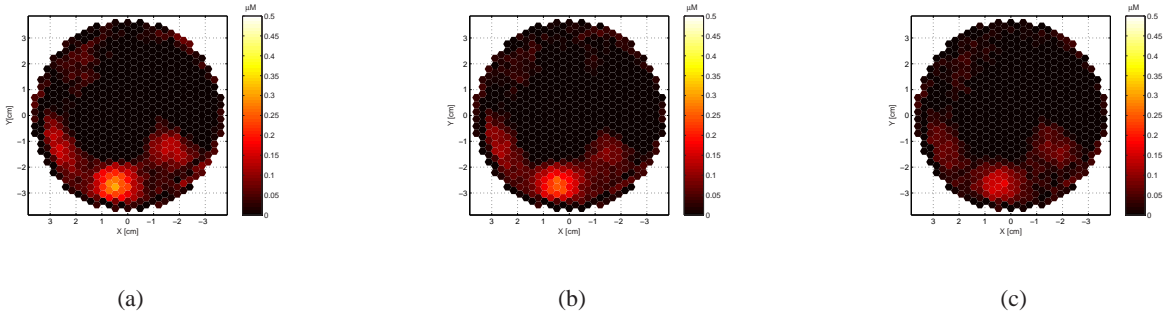


Fig. 12. Direct reconstructed ICG concentration images in the EES for Case 1 for (a) 246.4^{th} , (b) 334.4^{th} , and (c) 422.4^{th} seconds.

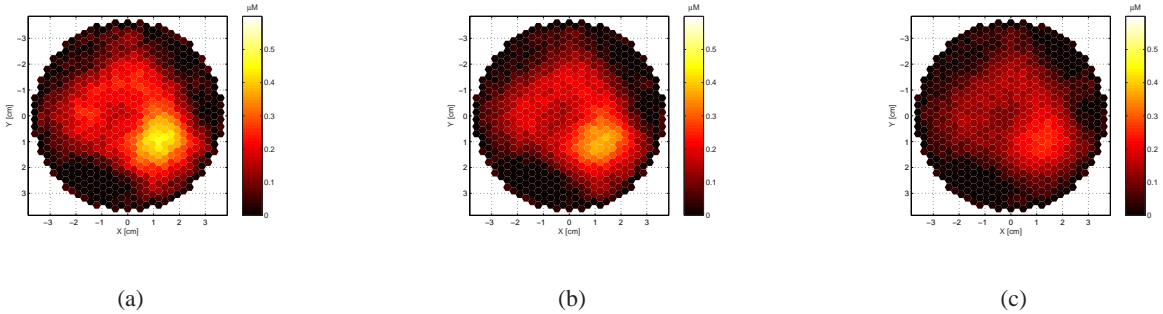


Fig. 13. Direct reconstructed ICG concentration images in plasma for Case 2 for (a) 228.8^{th} , (b) 316.8^{th} , and (c) 404.8^{th} seconds.

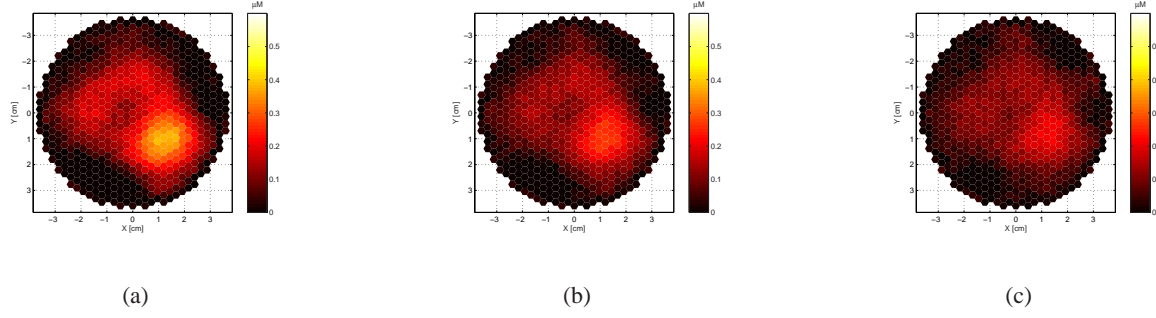


Fig. 14. Direct reconstructed ICG concentration images in the EES for Case 2 for (a) 228.8th, (b) 316.8th, and (c) 404.8th seconds.

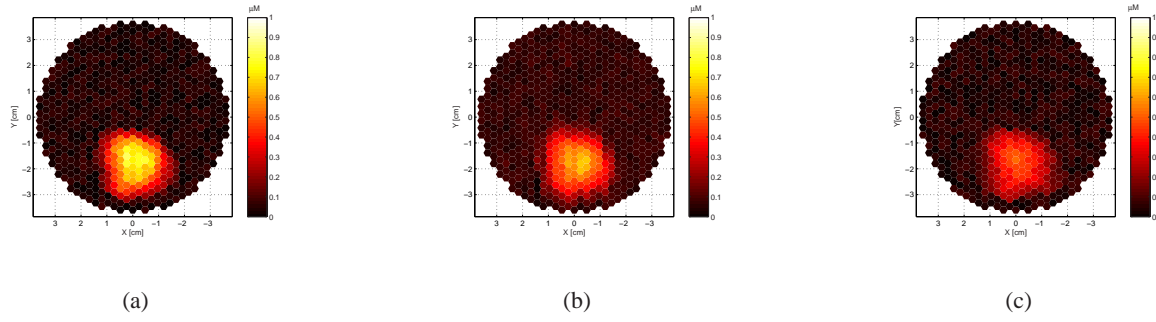


Fig. 15. Direct reconstructed ICG concentration images in the plasma for Case 3 for (a) 246.4th, (b) 378.4th, and (c) 510.4th seconds.

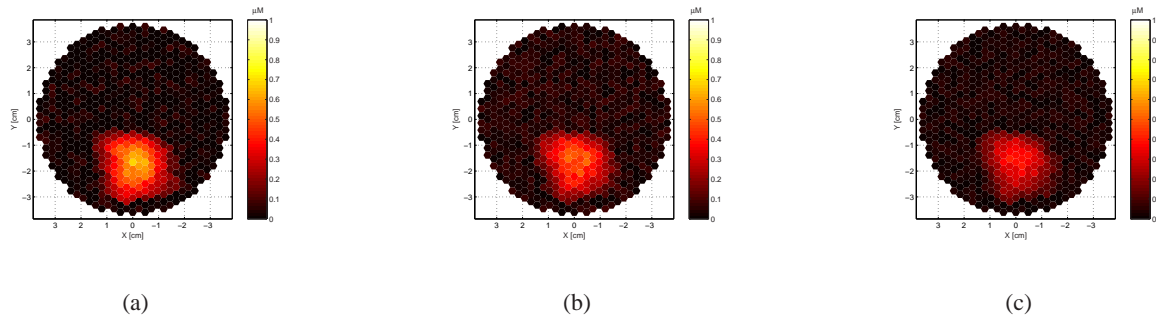


Fig. 16. Direct reconstructed ICG concentration images in the EES for Case 3 for (a) 246.4th, (b) 378.4th, and (c) 510.4th seconds.

B. AIM 3 - Evaluation of NIR Optical Features for Breast Cancer Diagnosis using *in vivo* Patient Data

The SOW with regard to Aim 3 includes the following specific tasks:

- Task 1. Determine statistical variability of each NIR feature inside and outside the suspected tumor in an individual and evaluate the statistical significance of the measured difference with the instrumentation precision. *12-18th month*
- Task 2. Design statistical classifiers to determine the ROC of each NIR feature for an individual. *18-24th month*
- Task 3. Evaluate the ROC, positive predicted value (PPV) and negative predicted value (NPV) of various combinations of the NIR features for an individual. *24-27th month*
- Task 4. Investigate the significance of the measured difference between malignant and benign tumor patient groups for single and combined NIR features. *27-30th month*

This work presents the evaluation of a set of optical features extracted from *in vivo* near-infrared spectroscopy data obtained from 116 patients with breast tumors for breast cancer diagnosis. The *in vivo* data was collected from 44 patients with malignant and 72 patients with benign tumors. Three features, relative blood volume concentration, oxygenation desaturation and the size of the tumor, are used to differentiate benign and malignant tumors. The diagnostic capability of these features are evaluated using different classifiers including nearest mean, neural network, support vector machine, Parzen, and normal density-based classifiers. The area under the receiver operating characteristics curve of the nearest mean classifier using the three features yields the best value of 0.91. This result suggests that relative blood volume concentration, oxygenation desaturation and size information can differentiate malignant and benign breast tumors with a relatively high precision.

1) *Apparatus:* In this study, a continuous wave (CW) near infrared spectrometer (NIRS) was used in collecting the *in vivo* data [94]. The apparatus includes a probe. The probe consists of one multi-wavelength (730nm, 805nm, and 850nm) LED as a light source at the center of the probe, and 8 silicon diodes as detectors arranged in a circular geometry with 4 cm radius as shown in Fig. 17. The light intensity from the detectors was adjusted to be approximately 1 volt and calibrated with a phantom with known absorption and scattering coefficients ($\mu_a=0.04$ to 0.07 cm^{-1} and $\mu'_s= 8 \text{ cm}^{-1}$).

2) *Patients and Protocol:* The *in vivo* data was collected at two centers, the Abramson Family Cancer Research Institute, Department of Radiology of the Hospital of University of Pennsylvania (HUP), and the Department of Gynecology of Leipzig University (DGLU). HUP provided 24 patients with malignant and 64 patients with benign

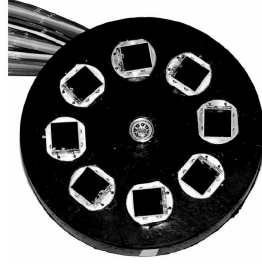


Fig. 17. The NIR probe with a multi-wavelength LED and 8 silicon diodes as detectors.

tumors. DGLU provided 20 patients with malignant and 8 patients with benign tumors.

The measurements were taken on the tumor-free contralateral breast to include the mirror image location of the suspected tumor. The probe was then transferred to the breast with suspected tumor. The detectors giving the largest changes with respect to the contralateral breast were assumed to be related to tumor and used for diagnosis.

3) *Optical Features:* In this study, three features, namely, relative blood volume concentration, ΔBV , oxygenation desaturation, $\Delta Deoxy$, and the size of the tumor, S , are used.

ΔBV , and $\Delta Deoxy$ values are obtained based on a lipid blood oxygen model [94]. Thus, the change in BV and $Deoxy$ are relative to the contralateral breast:

$$\Delta BV = \Delta BV_{tumor} - \Delta BV_{contra} \quad (38)$$

$$\Delta Deoxy = \Delta Deoxy_{tumor} - \Delta Deoxy_{contra} \quad (39)$$

where ΔBV_{tumor} , ΔBV_{contra} are relative blood volume concentration in the tumor breast with respect to the contralateral breast, respectively, and $\Delta Deoxy_{tumor}$, $\Delta Deoxy_{contra}$ are relative oxygenation desaturation in the tumor breast with respect to the contralateral breast, respectively.

The relative blood volume concentration, ΔBV , and the oxygenation desaturation, $\Delta Deoxy$, can be approximated at two different wavelengths by

$$\Delta BV \propto \gamma \Delta OD_{730} + \Delta OD_{850} \quad (40)$$

$$\Delta Deoxy \propto \beta \Delta OD_{730} + \Delta OD_{850} \quad (41)$$

where ΔOD_{730} , and ΔOD_{850} denote the relative changes in optical density at 730 nm and 850 nm, respectively, $\gamma = 0.3$, and $\beta = 1.3$ are the matching constants, and ΔOD is the differential optical density given by

$$\Delta OD = \log \frac{I_0}{I} \quad (42)$$

where I is light intensity after absorption and scattering, and I_0 is the baseline light intensity obtained from the contralateral breast.

To demonstrate the utility of equations (40) and (41), and obtain the matching constants, ΔBV and $\Delta Deoxy$ were calculated using:

$$\Delta BV \propto \Delta[Hb] + \Delta[HbO_2] \quad (43)$$

$$\Delta Deoxy \propto \Delta[HbO_2] - \Delta[Hb] \quad (44)$$

where $\Delta[Hb]$ and $\Delta[HbO_2]$ denote the relative change in deoxyhemoglobin (Hb) and oxyhemoglobin (HbO₂) with respect to the collateral breast.

The concentrations of $\Delta[Hb]$ and $\Delta[HbO_2]$ were calculated using:

$$\Delta OD = \varepsilon \Delta C \Delta L \quad (45)$$

where OD is the optical density, ε is the known extinction coefficients of Hb, HbO₂, C is the concentration, L is the mean path-length of photons. Here, $\varepsilon \approx 1 \text{ cm}^{-1}$, and $\Delta L = 4 \text{ cm}$ for a differential path-length factor of 7-8 [94], [95].

4) Feature Analysis and Tumor Classification: In this section, we present the classifiers, training techniques, statistical analysis of the dataset, and the malignancy differentiation criteria. Before we begin our discussion, note that, in our context, dataset is the set which contains all malignant and benign cases; training and test sets are subsets of the dataset.

Figure 18 shows the distribution of the three features for 116 patients. Blue circles indicate malignant cases and pink circles indicates benign cases. Note that the malignant class has a large spread as compared to benign class.

5) Classifiers: We evaluate the malignancy differentiation capability of the individual features and various combinations of the these features using 5 different classifiers, namely, Parzen density-based classifier (PAR), neural network classifier (NEURC), support vector classifier (SVC), normal densities-based quadratic classifier (NDC), scaled nearest mean classifier (NMSC) [96]–[100].

In Parzen density-based classification technique, given a kernel function, the probability distribution of the training set is approximated via a linear combination of kernels and a test set is assigned to the class with maximal posterior probability [100].

The support vector classifiers are based on support vector machines. In support vector machine based classification, each data point in the dataset is represented by a k -dimensional vector. Assuming, each data point belongs to only

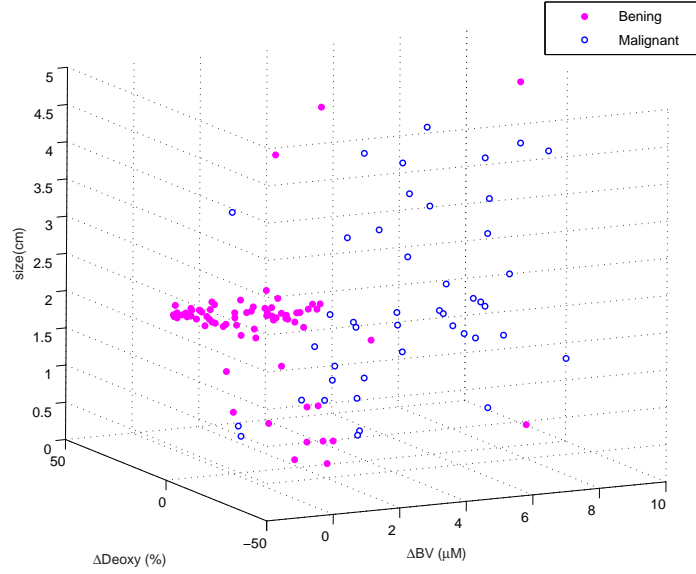


Fig. 18. Distribution of three features, ΔBV , $\Delta Deoxy$, and S for 116 patients. Blue circles indicate malignant cases and pink circles indicates benign cases.

one of two classes, the support vector classifier separate the dataset with a "k minus 1" dimensional hyperplane with maximum separation between the two classes. In other words, the nearest distance between a data point in one hyperplane and a data point in the other hyperplane is maximized [96]–[98].

The NDC is based on computation of a quadratic discriminant functional for the classes in the dataset using normal densities. Similarly, NMSC uses a linear discriminant functional for the classes in the dataset assuming equal class variances [100].

6) *Classifier Training Techniques:* The classifiers are trained by using three different training techniques, namely, hold-out, n -fold cross validation, and leave-one-out techniques [91], [99], [100]. In hold-out technique the original dataset (malignant and benign cases) is split into training and test sets randomly. The training set is used for generating the classification model and the test set is used to test the classification performance of the classifier. To obtain more reliable results for hold-out training technique, we repeated the classification with different sub-samples, i.e., in each repetition, a certain proportion is randomly selected for training, the rest of data is used for testing. The error rates on different repetitions are averaged to yield an overall performance of the classifier. In the hold-out technique different test sets overlap hence it is not optimal. In order to prevent overlapping, we used the n -fold cross-validation training technique with training set size equal to $N - N/n$ and test set size N/n . Here n is the number of subsets and N is the total number of the cases including both malignant and benign cases. In this

technique, we split the total number of cases into $n = 10$ subsets of equal size and use each subset for testing and the remainder subset for training. The results are then averaged to get an overall classification performance. To improve our results further, we use a special case of cross-validation technique, the leave-one-out technique, with $n = N$. In this technique, one sample is used for testing, and the remaining $N-1$ samples are used for training the classifier. More detailed discussions on these classifiers and training techniques can be found in [91], [99], [100].

We evaluated the malignancy differentiation capability of the following individual (ΔBV , $\Delta Deoxy$, S) and combined features (ΔBV - $\Delta Deoxy$, ΔBV - $\Delta Deoxy$ - S).

III. STATISTICAL ANALYSIS OF CLINICAL DATA

We evaluated the diagnostic capability of different combinations of optical features based on receiver operating characteristics (ROC) methodology using different classifiers and training techniques [81]–[83]. The ROC curve is obtained by plotting the probability of false positive rate versus the probability of detection. The evaluation of classification method is done using area under the ROC curve (AUC).

First, we evaluated the classification performance of all three features combined. Table V presents the AUC values for 5 different classifiers using three different training techniques. The AUC values of 5 different classifiers using leave-one-out training technique range from 0.8864 to 0.9098 with NMSC performing the best.

TABLE V

AUC VALUES FOR DIFFERENT CLASSIFIERS FOR ΔBV - $\Delta Deoxy$ - S

| | NMSC | PAR | SVC | NDC | NEURC |
|------------------|------------------------|----------------|---------------|---------------|---------------|
| Leave-one-out | 0.9098 ± 0.0065 | 0.9041± 0.0048 | 0.9011±0.0057 | 0.8984±0.0038 | 0.8864±0.0051 |
| Cross-validation | 0.8905 ±0.0044 | 0.8863±0.0039 | 0.8802±0.0066 | 0.8737±0.0029 | 0.8709±0.0072 |
| Hold-out | 0.8839 ±0.0040 | 0.8785±0.0058 | 0.8743±0.0027 | 0.8705±0.0062 | 0.8681±0.0066 |

TABLE VI

AUC VALUES FOR DIFFERENT CLASSIFIERS FOR ΔBV - $\Delta Deoxy$

| | NMSC | PAR | SVC | NDC | NEURC |
|------------------|-----------------------|---------------|---------------|---------------|---------------|
| Leave-one-out | 0.9001 ±0.0029 | 0.8993±0.0043 | 0.8902±0.0026 | 0.8908±0.0073 | 0.8792±0.0048 |
| Cross-validation | 0.8896 ±0.0054 | 0.8853±0.0070 | 0.8830±0.0019 | 0.8847±0.0062 | 0.8703±0.0071 |
| Hold-out | 0.8802 ±0.0048 | 0.8761±0.0055 | 0.8712±0.0091 | 0.8698±0.0047 | 0.8622±0.0063 |

Next, we evaluated the performance of the two features measured by NIR spectroscopy, namely ΔBV and

$\Delta Deoxy$. Table VI presents the AUC values for 5 different classifiers. The AUC values of 5 different classifiers range from 0.8792 to 0.9001 using leave-one-out training technique. Figure 19 show the distribution of features ΔBV , and $\Delta Deoxy$ extracted from benign and malignant tumors together with 5 different classifiers.

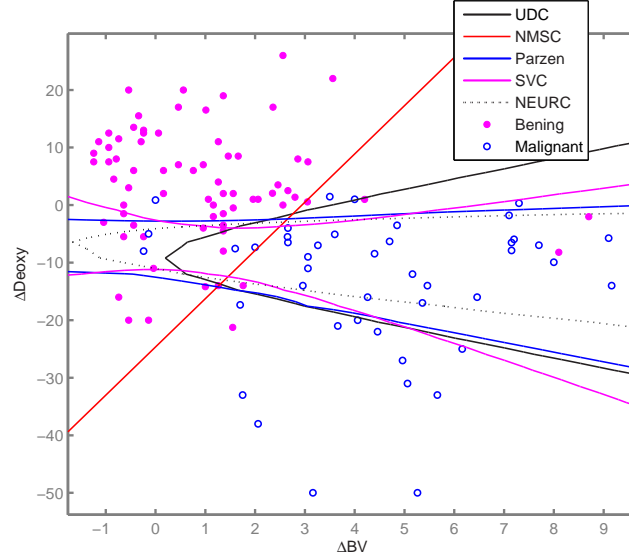


Fig. 19. 5 different classifiers and ΔBV - $\Delta Deoxy$ 2-D data clustering.

We next evaluated the individual classification performance of the three features. Table VII presents the AUC values for 5 different classifiers for the feature ΔBV . The NMSC has the best performance in terms of classification with a AUC value of 0.8817. Table VIII presents the results 5 different classifiers for the feature $\Delta Deoxy$. The NMSC has the best performance in terms of classification with a AUC value of 0.8787. Table IX presents the

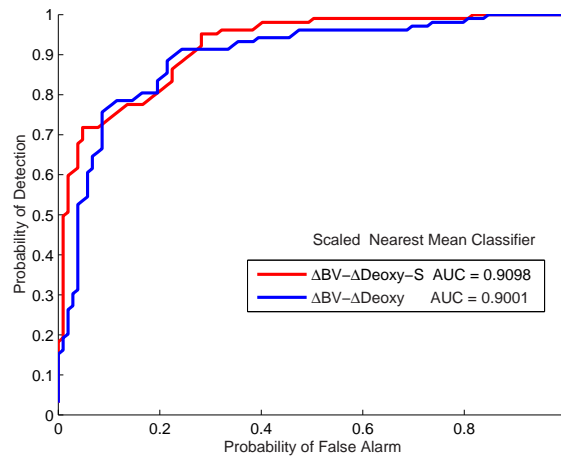


Fig. 20. ROC curves for ΔBV - $\Delta Deoxy$ -S and ΔBV - $\Delta Deoxy$ using NMSC classifier.

results of 5 different classifiers for the feature S . The NDC has the best performance in terms of classification with a AUC value of 0.5612.

As it can be seen from Table V, the best performing feature set is the combination of the three features. However, the combination set of optical features, obtained using optical spectroscopy, can differentiate breast tumors with a relatively high precision with a AUC value of 0.9001 (Table VI). Similarly, optical features, ΔBV and $\Delta Deoxy$, also performed well with AUC values of 0.8817 and 0.8787, respectively (Tables VII and VIII). We can also conclude from Table IX that, the tumor size alone is not informative in differentiating benign and malignant tumors.

TABLE VII

AUC VALUES FOR DIFFERENT CLASSIFIERS FOR ΔBV

| | NMSC | PAR | SVC | NDC | NEURC |
|------------------|----------------------------|---------------------|---------------------|---------------------|---------------------|
| Leave-one-out | 0.8817 \pm 0.0036 | 0.8802 \pm 0.0060 | 0.8794 \pm 0.0047 | 0.8779 \pm 0.0032 | 0.8513 \pm 0.0051 |
| Cross-validation | 0.8742 \pm 0.0058 | 0.8719 \pm 0.0069 | 0.8715 \pm 0.0061 | 0.8693 \pm 0.0070 | 0.8461 \pm 0.0038 |
| Hold-out | 0.8703 \pm 0.0021 | 0.8657 \pm 0.0042 | 0.8634 \pm 0.0018 | 0.8617 \pm 0.0081 | 0.8399 \pm 0.0067 |

TABLE VIII

AUC VALUES FOR DIFFERENT CLASSIFIERS FOR $\Delta Deoxy$

| | NMSC | PAR | SVC | NDC | NEURC |
|------------------|----------------------------|---------------------|---------------------|---------------------|---------------------|
| Leave-one-out | 0.8787 \pm 0.0044 | 0.8764 \pm 0.0053 | 0.8730 \pm 0.0069 | 0.8711 \pm 0.0032 | 0.8491 \pm 0.0060 |
| Cross-validation | 0.8703 \pm 0.0032 | 0.8688 \pm 0.0048 | 0.8604 \pm 0.0076 | 0.8598 \pm 0.0059 | 0.8412 \pm 0.0082 |
| Hold-out | 0.8656 \pm 0.0056 | 0.8602 \pm 0.0041 | 0.8567 \pm 0.0058 | 0.8504 \pm 0.0071 | 0.8389 \pm 0.0046 |

Figure 20 presents, the ROC curves for all three features, and the best two features, namely, $\Delta Deoxy$ and ΔBV using the scaled nearest mean classifier. The observed area under the ROC curve for ΔBV - $\Delta Deoxy$ - S , and ΔBV - $\Delta Deoxy$ are 0.9098, and 0.9001, respectively. Figure 21 presents the ROC curves for individual features ΔBV , and $\Delta Deoxy$ using the scaled nearest mean classifier. The observed AUC for ΔBV , and $\Delta Deoxy$ are 0.8817 and 0.8787, respectively.

Next, we checked whether the AUC values obtained for different combinations of features are statistically different or not. If so, we can declare that some combination of features are more informative than the others for diagnostic purposes. To check the statistical difference in performance, we set up a two class hypothesis testing problem. The null hypothesis corresponds to the case of $AUC_1 = AUC_2$ while the alternative hypothesis corresponds to ($AUC_1 \neq AUC_2$). The hypothesis test described above is reexpressed as follows:

TABLE IX

AUC VALUES FOR DIFFERENT CLASSIFIERS FOR S

| | NMSC | PAR | SVC | NDC | NEURC |
|------------------|---------------|---------------|---------------|-----------------------|---------------|
| Leave-one-out | 0.5123±0.0101 | 0.5292±0.0088 | 0.5291±0.0074 | 0.5612 ±0.0081 | 0.5382±0.0092 |
| Cross-validation | 0.5057±0.0069 | 0.5233±0.0084 | 0.5204±0.0069 | 0.5585 ±0.0072 | 0.5301±0.0113 |
| Hold-out | 0.5001±0.0078 | 0.5184±0.0061 | 0.5178±0.0091 | 0.5478 ±0.0046 | 0.5267±0.0082 |

$H_0 : \implies \text{AUC}_1 = \text{AUC}_2$ (No difference in performance)

$H_1 : \implies \text{AUC}_1 \neq \text{AUC}_2$ (Statistical difference in performance)

We assume that the features are jointly Gaussian distributed and computed the z -statistics as:

$$z = \frac{\text{AUC}_1 - \text{AUC}_2}{\sqrt{\sigma_1^2 + \sigma_2^2 - 2r\sigma_1\sigma_2}} \quad (46)$$

where r is the correlation coefficient of AUC_1 and AUC_2 , σ_1^2 , and σ_2^2 are the variance of AUC_1 and AUC_2 , respectively.

Next, we calculated the p-value based on the z -statistics [92], [93]. We reject the null hypothesis H_0 if the p-value is smaller than 0.05 (a predefined significance level), otherwise we accept the null hypothesis.

We first compared the AUC values of combined features ΔBV - $\Delta Deoxy$ - S , $\text{AUC}(\Delta BV - \Delta Deoxy - S)$, with $\text{AUC}(\Delta BV - \Delta Deoxy)$ obtained by using the NMSC classifier trained with leave-one-out technique. The p-value is calculated to be 0.144. Using the hypothesis test described above, we conclude that there is no significant difference in performance using the tumor size information together with the optical features, ΔBV and $\Delta Deoxy$. We next compared the AUC values of $\text{AUC}(\Delta BV)$ and $\text{AUC}(\Delta Deoxy)$ obtained by using NMSC classifier. The p-value is calculated to be 0.361. Again, we found out that there is no significant difference between the diagnostic capability of ΔBV and $\Delta Deoxy$. We also compared the values of $\text{AUC}(\Delta BV - \Delta Deoxy)$ with that of $\text{AUC}(\Delta BV)$ and $\text{AUC}(\Delta Deoxy)$. The p-values are 0.0371, and 0.0401. Using these values, based on the hypothesis testing, we can conclude that combination of optical features has better diagnostic capability than that of individual features ΔBV and $\Delta Deoxy$. Finally, we compared the AUC values of $\text{AUC}(\Delta BV)$ and $\text{AUC}(\Delta Deoxy)$ with the AUC value of $\text{AUC}(S)$ obtained by using NMSC classifier. The p-values are 0.0103 and 0.0178, respectively. Using the hypothesis test, there is a significant difference in the classification performance of the optical features, ΔBV and $\Delta Deoxy$, when compared to the tumor size information.

Using the same hypothesis testing problem defined above, we compared the performances of different classifiers in terms of the AUC values obtained using three features trained with leave-one-out technique. The AUC value of

NMSC classifier is statistically different from the AUC values of PAR, SVC, NDC, and NEURC classifiers with p-values of 0.0312, 0.0274, 0.0201, 0.0113, respectively. We also compared the performance of PAR classifier with SVC, NDC, and NEURC classifiers. The AUC values of PAR and SVC classifiers are not statistically different in terms of classification of three features, with a p-value of 0.182. However, the AUC value of PAR classifier is statistically different from the AUC values of NDC and NEURC classifiers with p-values of 0.0234, 0.0217, respectively. Similarly, the AUC value of SVC classifier is statistically different from NDC and NEURC classifiers with p-values of 0.0118, 0.0152, respectively. Finally, we compared the performances of NDC and NEURC classifiers. The AUC value of NDC classifier is statistically different from the AUC value of NEURC classifier with a p-value of 0.0385.

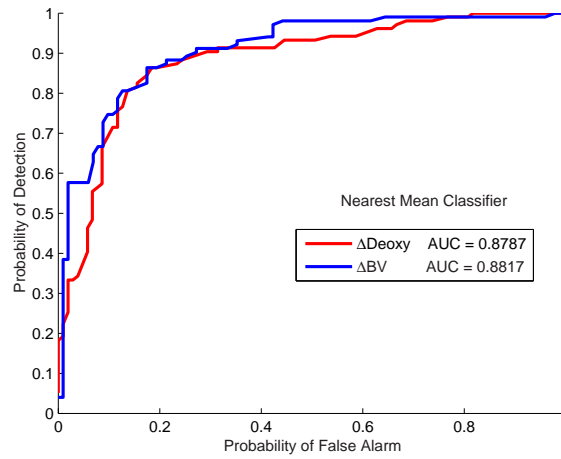


Fig. 21. ROC curves for ΔBV and $\Delta Deoxy$ using NMSC Classifier.

IV. KEY RESEARCH ACCOMPLISHMENTS

- 1) We demonstrated, for the first time in the literature, the value of spatially resolved pharmacokinetic-rates as opposed to bulk-rates using in vivo breast patient data. This work was published as a journal paper in *Physics in Medicine and Biology* (1). *The paper was downloaded more than 250 times within the first three months after its publication and was ranked among the top 10% of all papers published by the Institute of Physics.*
- 2) We developed methods of reconstructing pharmacokinetic-rate images directly from NIR boundary measurements and applied our technique to in vivo breast cancer data. The results show that the technique is robust and provides better signal-to-noise ratio images. We submitted our results to *IEEE Transactions in Medical Imaging*.
- 3) We further analyze the NIR parameters collected from 116 patients using NIR spectroscopy. This work is currently being prepared as a journal paper.

V. REPORTABLE OUTCOMES

Complete list of outcomes is given below:

- 1) B. Alacam, B. Yazici, X. Intes, B. Chance, S. Nokia, "Pharmacokinetic-rate Images of Indocyanine Green for Breast Tumors using Near Infrared Optical Methods, *Physics in Medicine and Biology*, Vol. 53, No: 4, pp: 837-859, 2008.
- 2) B. Alacam, B. Yazici, X. Intes, B. Chance, Direct Reconstruction of Spatially Resolved Pharmacokinetic Rate Images of Optical Fluorophores from NIR Measurements, submitted to *IEEE Transactions in Medical Imaging*.
- 3) B. Alacam, B. Yazici, B. Chance, S. Nioka, "Evaluation of NIR Optical Features for Breast Cancer Diagnosis using *in vivo* Patient Data," to be submitted to *IEEE Transactions in Biomedical Engineering*.
- 4) B. Alacam, B. Yazici, B. Chance, S. Nioka, "Characterization of Breast Tumors with NIR Methods using Optical Indices, in *Proc. of IEEE EMBS-29th Anniversary Conference*, pp. 5186-5189, Lyon, France, August 2007.
- 5) M.Guven, B. Yazici, E. Giladi, "Effect of discretization error and adaptive mesh generation for simultaneous reconstruction of scattering and absorption images in diffuse optical tomography, *Proceedings of SPIE Photonics West*, Vol. 6850, 68500W, January 2008.

- 6) L. Reilly-Raska, M. Guven, B. Yazici, “Effect of discretization error and adaptive mesh generation for fluorescence diffuse optical tomography, *Proceedings of SPIE Photonics West*, Vol. 6850, 68500B, January 2008.
- 7) L. Zhou, B. Yazici, V. Ntziachristos, “Fluorescence Molecular Tomography Reconstruction with a priori Anatomical Information, *Proceedings of SPIE Photonics West*, vol. 6868, 68680O, January 2008.
- 8) M. Guven, B. Yazici, K. Kwon, E. Giladi, X. Intes, Effect of discretization error and adaptive mesh generation in diffuse optical absorption imaging: Part II,” *Inverse Problems*, Vol. 23, pp: 1135-1160, May 2007.
- 9) M. Guven, B. Yazici, K. Kwon, E. Giladi, X. Intes, Effect of discretization error and adaptive mesh generation in diffuse optical absorption imaging: Part I,” *Inverse Problems*, Vol. 23, pp: 1115-1133, May 2007.
- 10) M. Guven, B. Yazici, E. Giladi, and X. Intes, “Adaptive mesh generation for diffuse optical tomography, *4th IEEE International Symposium on Biomedical Imaging: From Nano to Macro*, pp: 1380-1383, 2007.
- 11) M. Guven, B. Yazici and V. Ntziachristos, “Fluorescence diffuse optical Image reconstruction with a priori information, *Proceedings of SPIE Photonics West 2007*, Vol. 6431, pp: 643107, 2007.
- 12) Murat Guven, who was partly supported by this grant, received his PhD degree in December 2007.
- 13) Burak Alacam, who was partly supported by this grant received his PhD degree in June 2008.

VI. CONCLUSIONS

In January 2008, we published our results on ICG pharmacokinetic-rate imaging applied to three in vivo patient data with breast tumors in *Physics in Medicine and Biology*. Our paper is downloaded more than 250 times within the next three months of its publication. We have received a note from Institute of Physics that our paper is ranked among the top 10% among all journal papers published by Institute of Physics. The reviewer comments also pointed out to the novelty of our work.

We continued our work on the reconstruction of pharmacokinetic-rate images from NIR boundary measurements. Instead of the two-step decoupled approach described in our *Physics in Medicine and Biology* publication, this time we studied the reconstruction of pharmacokinetic-rate images directly from the optical boundary measurements. This approach couples the reconstruction of ICG concentration images and pharmacokinetic-rate images. As a result, it takes advantage of inherent temporal and spatial correlations between consecutive optical boundary measurements. This results in higher SNR than the pharmacokinetic-rate images obtained from absorption images. We assessed the value of this approach in *in vivo* data obtained from three patients with breast tumors and showed that they

result in higher SNR than the images obtained with the two-step decoupled approach. We submitted our results to IEEE Transactions in Medical Imaging.

We continued to analyze the 116 breast cancer patient data obtained using NIR spectroscopy and refine our imaging algorithms. The *in vivo* data was collected from 44 patients with malignant and 72 patients with benign tumors. We used three features, relative blood volume concentration, oxygenation desaturation and the size of the tumor, to differentiate benign and malignant tumors. We evaluated the diagnostic capability of these features using different classifiers including nearest mean, neural network, support vector machine, Parzen, and normal density-based classifiers. The area under the receiver operating characteristics curve of the nearest mean classifier using the three features yields the best value of 0.91. This result suggests that relative blood volume concentration, oxygenation desaturation and size information can differentiate malignant and benign breast tumors with a relatively high precision. This work will be submitted as a journal paper to IEEE Transactions in Biomedical Imaging.

Murat Guven and Burak Alacam, who were partly supported by this grant, received their Ph.D. degrees in December 2007, and June 2008, respectively.

We applied for a “No Cost Extension” for our grant to complete the Aim 4 of our project. The main impediment to our progress has been the retirement of our collaborator, Prof. Britton Chance of University of Pennsylvania. His retirement interrupted the MR-NIR patient data collection. The novel concurrent imager is now taken over by Prof. Arjun Yodh of University of Pennsylvania. We reached an agreement with Prof. Yodh to collaboratively collect data in the next one year and analyze it. We are confident that we will complete Aim 4 of our project and submit a final report in the next reporting cycle.

REFERENCES

- [1] Folkman, J., Tumor angiogenesis: therapeutic implications. *N. Engl. J. Med.*, 1971. 285(21): p. 1182-6.
- [2] Folkman, J., What is the evidence that tumors are angiogenesis dependent? *J. Natl. Cancer inst.*, 1990. 82(1): p. 4-6.
- [3] Blood, C. H. and B. R. Zetter, Tumor interactions with the vasculature: angiogenesis and tumor metastasis. *Biochem. Biophys. Acta*, 1990. 1032(1): p. 89-118.
- [4] Vaupel, P., et al., Current status of knowledge and critical issues in tumor oxygenation. Results from 25 years research in tumor pathophysiology. *Adv. Exp. Med. Biol.*, 1998. 454: p. 591-602.
- [5] Vaupel, P., et al., Oxygenation of human tumors: evaluation of tissue oxygen distribution in breast cancers by computerized O₂ tension measurements. *Cancer Res.*, 1991. 51(12): p. 3316-22.
- [6] Runkel, S., et al., Oxygenations of mammary tumors as evaluated by ultrasound-guided computerized-pO₂-histography. *Adv. Exp. Med. Biol.*, 1994. 345: p. 451-8.
- [7] Pogue, B. W., et al., Quantitative hemoglobin tomography with diffuse near-infrared spectroscopy: pilot results in the breast. *Radiology*, 2001. 218(1): 261-6.
- [8] Gurfinkel M et al 2000 Pharmacokinetics of ICG and HPPH-car for the detection of normal and tumour tissue using fluorescence, near-infrared reflectance imaging: a case study *Photochem. Photobiol.* 72 94-102
- [9] Harms S E. Breast magnetic resonance imaging. *Seminars in Ultrasound, CT & MR* 1998; 19:104-120.
- [10] Harms SE, Flamig DP, Hesley KL, et al. MR imaging of the breast with rotating delivery of excitation off resonance: clinical experience with pathologic correlation. *Radiology* 1993; 187:493-501.
- [11] Williams MB, Pisano ED, Schnall MD, Fajardo LL. Future directions in imaging of breast diseases. *Radiology* 1998; 206:297-300.
- [12] Swift M, Morrell D, Massey RB, Chase CL. Incidence of cancer in 161 families affected by ataxia-telangiectasia. *New England Journal of Medicine* 1991; 325:1831-1836.
- [13] Esserman L, Hylton N, Yassa L, et al. Utility of magnetic resonance imaging in the management of breast cancer: Evidence for improved preoperative staging. *J Clin Oncol* 1999; 17:110-119.
- [14] Robinson, K. J., C. J. Kotre and K. Faulkner. "The use of contrast-detail test objects in the optimization of optical density in mammography." *Br. J. Radiol.* 68: 277-282, 1995.
- [15] Moran, G. R. and F. S. Prato. "Modeling tissue contrast agent concentration: a solution to the tissue homogeneity model using a simulated arterial input function." *Mag. Res. Med.* 45:42-45, 2001.
- [16] Fantini S, Hueber D, Franceschini MA, Gratton E, Rosenfeld W, Stubblefield PG, Maulik D, Stankovic MR., "Non-invasive optical monitoring of the newborn piglet brain using continuous-wave and frequency-domain spectroscopy," *Phys. Med. Biol.*, Vol. 44, pp. 1543-1563, 1999.
- [17] L. A. Bauer, *Applied Clinical Pharmacokinetics*, McGraw-Hill, New York, 2001.
- [18] C. W. Tornoe, "Grey-Box PK/PD Modeling of Insulin," M.S. Thesis, June 28, 2002.
- [19] D. H. Anderson, *Lecture Notes in Biomathematics*, Springer-Verlag, Berlin, 1983.
- [20] J. A. Jacquez, *Compartmental analysis in biology and medicine, Kinetics of distribution of tracer-labeled materials*, Elsevier Pub. Co., New York, 1972.

- [21] C. C. Martin, R. F. Williams, J. H. Gao, L. D. Nickerson, J. Xiong, P. T. Fox, "The pharmacokinetics of hyperpolarized xenon: implications for cerebral MRI," *J Magn Reson Imaging*, vol. 7, no. 5, pp. 848-854, 1997.
- [22] G. R. Moran, F. S. Prato, "Modeling (1H) exchange: an estimate of the error introduced in MRI by assuming the fast exchange limit in bolus tracking," *Magn Reson Med.*, vol. 51, no. 4, pp. 816-827, 2004.
- [23] R. Srikanchana, D. Thomasson, P. Choyke, A. Dwyer, "A Comparison of Pharmacokinetic Models of Dynamic Contrast Enhanced MRI," *7th IEEE Symposium on Computer-Based Medical Systems*, pp.361, 2004.
- [24] M. J. Eppstein, D. E. Dougherty, T. Troy, E. M. Sevick-Muraca, "Biomedical optical tomography using dynamic parametrization and Bayesian conditioning on photon migration measurements." *Applied Optics*, vol. 38-10, pp. 2138-2150, 2001.
- [25] V. Kolehmainen, S. Prince, S. R. Arridge, and J. P. Kaipio, "State-estimation approach to the nonstationary optical tomography problem," *J. Opt. Soc. Am.*, vol. A 20, pp. 876889, 2003.
- [26] S. Prince, V. Kolehmainen, J. P. Kaipio, M. A. Franceschini, D. Boas, and S. R. Arridge, "Time-series estimation of biological factors in optical diffusion tomography," *Phys. Med. Biol.* Vol. 48, 1491-1504, 2003.
- [27] R. E. Carson and K. Lange, "The EM parametric image reconstruction algorithm," *J. Am. Statist. Assoc.*, vol. 80, no. 389, pp. 2022, 1985.
- [28] M. A. Limber, M. N. Limber, A. Cellar, J. S. Barney, and J. M. Borwein, "Direct reconstruction of functional parameters for dynamic SPECT," *IEEE Trans. Nucl. Sci.*, vol. 42, no. 4, pp. 1249-1256, 1995.
- [29] S. R. Meikle, J. C. Matthews, V. J. Cunningham, D. L. Bailey, L. Livieratos, T. Jones, and P. Price, "Parametric image reconstruction using spectral analysis of PET projection data," *Phys. Med. Biol.*, vol. 43, pp. 651666, 1998.
- [30] W. Reutter, G.T. Gullberg and R.H. Huesman, "Kinetic parameter estimation from attenuated SPECT projection measurements," *IEEE Trans Nucl Sci*, vol. 45, pp. 1340-1344, 1998.
- [31] O. Langer, R. Karch, U. Mller, G. Dobrozemsky, A. Abraham, M. Zeitlinger, E. Lackner, C. Joukhadar, R. Dudczak, K. Kletter, M. Mller, M. Brunner, "Combined PET and Microdialysis for In Vivo Assessment of Intracellular Drug Pharmacokinetics in Humans," *Journal of Nuclear Medicine*, vol. 46, no. 11, pp. 1835-1841, 2005.
- [32] M. Kamasak, C. A. Bouman, E. D. Morris, and K. Sauer, "Direct Reconstruction of Kinetic Parameter Images from Dynamic PET Data," *IEEE Trans Med Imag*, vol. 24, pp. 636-650, 2005.
- [33] A. B. Milstein, K. J. Webb, and C. A. Bouman, "Estimation of kinetic model parameters in fluorescence optical diffusion tomography," *J. Opt. Soc. Am.*, Vol. 22, No. 7, pp. 1357-1368, 2005.
- [34] D. Hansen, A. Spence, T. Carski, and M. Berger, "Indocyanine green (ICG) staining and demarcation of tumor margins in a rat glioma model," *Surg. Neurol.*, vol. 40, pp. 451-456, 1993.
- [35] H. Shinohara, A. Tanaka, T. Kitai, N. Yanabu, T. Inomoto, S. Satoh, Hatano, Y. Yamaoka, and K. Hirao, "Direct measurement of hepatic Indocyanine Green clearance with near-infrared spectroscopy: separate evaluation of uptake and removal," *Hepatology*, vol. 23, pp. 137-144, 1996.
- [36] A. ElDeosky, A. Seifalian, M. Cope, D. Delpy, and B. Davidson, "Experimental study of liver dysfunction evaluated by direct Indocyanine green clearance using near infrared spectroscopy," *Br. J. Surg.*, vol. 86, pp. 1005-1011, 1999.
- [37] B. Alacam, B. Yazici, X. Intes, B. Chance, "Extended Kalman Filtering for the Modeling and Analysis of ICG Pharmacokinetics in Cancerous Tumors using NIR Optical Methods", *Transactions in IEEE Biomedical Engineering*, vol. 53, no. 10, pp. 1861-1871, 2006.
- [38] M. Gurfinkel, A. B. Thompson, W. Ralston, T. L. Troy, A. L. Moore, T. A. Moore, J. D. Gust, D. Tatman, J. S. Reynolds, B. Muggenburg,

- K. Nikula, R. Pandey, R. H. Mayer, D. J. Hawrysz, and E. M. Sevick-Muraca, "Pharmacokinetics of ICG and HPPH-car for the detection of normal and tumor tissue using fluorescence, near-infrared reflectance imaging: a case study," *Photochem. Photobiol.*, vol. 72, 2000, pp. 94-102.
- [39] D.J. Cuccia, F. Bevilacqua, A. J. Durkin, S. Merritt, B. J. Tromberg, G. Gulsen, H. Yu, J. Wang, and O. Nalcioglu, "In vivo quantification of optical contrast agent dynamics in rat tumors by use of diffuse optical spectroscopy with magnetic resonance imaging coregistration," *Applied Optics*, vol. 42, no. 1, June 2003.
- [40] X. Intes, J. Ripoll, Y. Chen, S. Nioka, A. G. Yodh, B. Chance, "In vivo continuous-wave optical breast imaging enhanced with Indocyanine Green," *Med. Phys.*, vol. 30-6, pp. 1039-1047, 2003.
- [41] B. Alacam, B. Yazici, X. Intes, B. Chance, "Spatially Resolved Pharmacokinetic Rate Images of ICG using Near Infrared Optical Methods," *Journal of Physics of Medicine and Biology*, Vol. 53-4, pp. 837-859, 2008.
- [42] Sevick-Muraca, E.M., Lopez, G., Troy, T.L., Reynolds, J.S., and Hutchinson, C.L., "Fluorescence and absorption contrast mechanisms for biomedical optical imaging using frequency-domain techniques," *Photochem. Photobiol.*, vol. 66, no. 55, 1997.
- [43] M. L. J. Landsman, G. Kwant, G. A. Mook, W. G. Zijlstra, "Light- absorbing properties, stability, and spectral stabilization of indocyanine green," *J. Appl. Physiol.*, vol. 40, 575-583, 1976.
- [44] F. Fedele, J. P. Laible, M. J. Eppstein, "Coupled complex adjoint sensitivities for frequency-domain fluorescence tomography: theory and vectorized implementation," *Journal of Computational Physics*, vol. 187-2, pp. 597-619, 2003.
- [45] M. J. Eppstein, F. Fedele, J.P. Laible, C. Zhang, A. Godavarty and E.M. Sevick-Muraca, "A comparison of exact and approximate adjoint sensitivities in fluorescence tomography," *IEEE Transactions on Medical Imaging*, vol. 22-10, pp. 1215-1223, 2003.
- [46] S. R. Arridge, "Optical tomography in medical imaging: topical review," *Inverse Problems*, vol.15, pp. R4193, 1999.
- [47] A. Soubret, and V. Ntziachristos, "Fluorescence molecular tomography in the presence of background fluorescence," *Phys. Med. Biol.*, Vol. 51, pp. 3983-4001, 2006.
- [48] C. Chen, *Linear System Theory and Design*, Oxford University Press, New York, 1999.
- [49] M. Boutayeb, H. Rafaralahy, M. Darouach, "Convergence analysis of the Extended Kalman Filter used as an observer for nonlinear deterministic discrete-time systems," *IEEE Transactions on Automatic Control*, vol. 42, no. 4, pp. 581-586. 1997.
- [50] B. J. Schnekenburger, "An extended Kalman filter as a parameter estimator for linear discrete time systems" M.S. thesis, University of NJIT, Newark, NJ, USA, 1988.
- [51] A. B. Milstein, S. Oh, K. J. Webb, C. A. Bouman, Q. Zhang, D. A. Boas, and R. P. Millane, "Fluorescence optical diffusion tomography," *Appl. Opt.* 42, 3081-3094, 2003.
- [52] A. B. Milstein, J. J. Stott, S. Oh, D. A. Boas, R. P. Millane, C. A. Bouman, and K. J. Webb, "Fluorescence optical diffusion tomography using multiple-frequency data," *J. Opt. Soc. Am. A* 21, 10351049 (2004).
- [53] L. Ljung, "Asymptotic Behavior of the Extended Kalman Filter as a Parameter Estimator for Linear Systems," *IEEE Tran. Automa. Control*, vol. AC-24, no. 1, pp. 36-50, 1979.
- [54] B. F. La Scala, and R. R. Bitmead, "Design of an extended Kalman filter frequency tracer," *IEEE Tran. on Sig. Proc*, vol. 44, no. 3, pp. 739-742, March 1996.
- [55] C.K.Chui, G. Chen, *Kalman Filtering with real time applications*, Springer, Berlin, 1999.
- [56] M.J. Gorris, D. A. Gray, I.M.Y Mareels, "Reducing the computational load of a Kalman filter," *IEEE Electronic Letters*, vol. 33-18, pp. 1539-1541, 1997.

- [57] H. Dehghani, B. W. Pogue, J. Shudong, B. Brooksby, and K. D. Paulsen. "Three-Dimensional Optical Tomography: Resolution in Small-Object Imaging," *Applied Optics*, Vol. 42, Issue 16, pp. 3117-3128.
- [58] B. W. Pogue Brian, S. Xiamoei SONG, T. D. Tosteston Tor, T. O. McBride Troy, J. Shudong, K. D. Paulse Keith, "Statistical analysis of nonlinearly reconstructed near-infrared tomographic images: Part I: Theory and simulations," *IEEE transactions on medical imaging*, vol. 21, no7, pp. 753-764, 2002.
- [59] B. W. Pogue Brian, S. Xiamoei SONG, T. D. Tosteston Tor, T. O. McBride Troy, J. Shudong, K. D. Paulse Keith, "Statistical analysis of nonlinearly reconstructed near-infrared tomographic images: Part II: Experimental Interpretation," *IEEE transactions on medical imaging*, vol. 21, no7, pp. 764-772, 2002.
- [60] M. E. Eames, Matthew, B. W. Pogue, C. M. Carpenter, H. Dehghani, "Three dimensional near infrared tomography of the breast", *Proceedings of the SPIE*, Volume 6629, pp. 66291K-1, 2007.
- [61] M. O'Leary, "Imaging with Diffuse Photon Density Waves," in PhD Thesis, Dept. Physics & Astronomy, U. of Pennsylvania, May 1996.
- [62] V. Ntziachristos, B. Chance, and A. Yodh, "Differential diffuse optical tomography," *Opt. Express*, vol. 5, pp. 230-242, 1999.
- [63] J. M. Brown, A. J. Giaccia, "The unique physiology of solid tumors: opportunities (and problems) for cancer therapy," *Cancer Res.* Vol. 58(7), pp. 1408-16, 1998.
- [64] H. Hashizume, P. Baluk, S. Morikawa, J. W. McLean, G. Thurston, S. Roberge, R. K. Jain, and D. M. McDonald, "Openings between Defective Endothelial Cells Explain Tumor Vessel Leakiness," *Am J Pathol.*, vol. 156(4), pp. 1363-1380, 2000.
- [65] K. Licha, "Contrast agents for optical imaging," *Topics in Current Chemistry*, vol. 222, pp. 1-29, 2002.
- [66] Y. Chen, G. Zheng, Z. Zhang, D. Blessington, M. Zhang, H. Li, "Metabolism Enhanced Tumor Localization by Fluorescence Imaging: In Vivo Animal Studies," *Optics Letters*, vol. 28, pp. 2070-2072, 2003.
- [67] R. Weissleder, C. H. Tung, U. Mahmood, A. Bogdanov, "In vivo imaging with protease-activated near-infrared fluorescent probes," *Nat. Biotech.*, vol. 17, pp. 375-378, 1999.
- [68] H. Dehghani, B. W. Pogue, J. Shudong, B. Brooksby, and K. D. Paulsen. "Three-Dimensional Optical Tomography: Resolution in Small-Object Imaging," *Applied Optics*, Vol. 42, Issue 16, pp. 3117-3128.
- [69] B. W. Pogue Brian, S. Xiamoei SONG, T. D. Tosteston Tor, T. O. McBride Troy, J. Shudong, K. D. Paulse Keith, "Statistical analysis of nonlinearly reconstructed near-infrared tomographic images: Part I: Theory and simulations," *IEEE transactions on medical imaging*, vol. 21, no7, pp. 753-764, 2002.
- [70] B. W. Pogue Brian, S. Xiamoei SONG, T. D. Tosteston Tor, T. O. McBride Troy, J. Shudong, K. D. Paulse Keith, "Statistical analysis of nonlinearly reconstructed near-infrared tomographic images: Part II: Experimental Interpretation," *IEEE transactions on medical imaging*, vol. 21, no7, pp. 764-772, 2002.
- [71] M. E. Eames, Matthew, B. W. Pogue, C. M. Carpenter, H. Dehghani, "Three dimensional near infrared tomography of the breast", *Proceedings of the SPIE*, Volume 6629, pp. 66291K-1, 2007.
- [72] American cancer society, <http://www.cancer.org/>, Breast Cancer Facts. 2008.
- [73] National Cancer Institute, <http://www.cancer.gov/>, Breast Cancer, 2008.
- [74] A. M. Leitch, G. D. Dodd, M. Costanza, "American Cancer Society guidelines for the early detection of breast cancer," *CA Cancer J Clin*, Vol. 47, pp. 50-153, 1997.
- [75] K. Kerlikowske, J. Barclay, "Outcomes of modern screening mammography," *J Natl Cancer Inst Monogr*, vol. 22, pp. 105-111.

- [76] B. Alacam, B. Yazici, N. Bilgutay et al, Breast Tissue Characterization using FARMA Modeling of RF Echo, *Journal of Ultrasound in Medicine and Biology*, vol.30-10, pp. 1397-1407, 2004.
- [77] J. W. Tian, L. T. Sun, Y. H. Guo, H. D., Zhang Y.T., "Computerized-aid diagnosis of breast mass using ultrasound image," *Medical Physics*, vol. 34-8, 3158-3164, 2007.
- [78] L. Liberman, E. A. Morris, D. D. Dershaw et al, "MR imaging of the ipsilateral breast in women with percutaneously proven breast cancer," *AJR Am J Roentgenol.*, vol. 180, pp. 901-910, 2003.
- [79] M. Van Goethem, K. Schelfout, L. Dijkmans, J. C. Van Der Auwera, J. Weyler, I. Verslegers, I. Biltjes and A. De Schepper, " MR mammography in the pre-operative staging of breast cancer in patients with dense breast tissue: comparison with mammography and ultrasound," *European Radiol*, vol. 14(5), pp. 809-816, 2004.
- [80] Report of the Joint Working Group on Quantitative In Vivo Functional Imaging in Oncology, Sponsored by the *U.S. Public Health Services Office on Womens Health and National Cancer Institute*, 1999.
- [81] J. A. Swets, "ROC Analysis applied to the evaluation of medical imaging techniques," *Investigative Radiology*, vol. 14, pp. 109-121, 1979.
- [82] C. E. Metz, "ROC methodology in radiologic imaging," *Investigative Radiology*, vol. 21, pp. 720-733, 1986.
- [83] D. D. Dorfman, K. S. Berbaum, C. E. Metz, "Receiver operating characteristics rating analysis: generalization of the population of readers and patients with the jackknife method," *Invest Radiol*, vol. 27, pp. 723-731, 1992.
- [84] B. W. Pogue, S. Jiang, H. Dehghani, C. Kogel, S. Soho, S. Srinivasan, X. Song, T. D. Tosteson, S. P. Poplack, K. D. Paulsen, "Characterization of hemoglobin, water, and NIR scattering in breast tissue: analysis of intersubject variability and menstrual cycle changes," *Journal of Biomedical Optics*, Vol. 9(3), pp. 541-552, 2004.
- [85] D. Grosenick, H. Wabnitz, K. T. Moesta, J. Mucke, M. Mller, C. Stroszczyński, J. Stel, B. Wassermann, P. M. Schlag, and H. Rinneberg, "Concentration and oxygen saturation of hemoglobin of 50 breast tumours determined by time-domain optical mammography," *Phys. Med. Biol.* Vol. 49 No. 7, pp. 1165-1181, 2004.
- [86] M. Khayat, Z. Ichalalene, N. Mincu, F. Leblond, O. Guilman, and S. Djeziri, "Optical tomography as adjunct to x-ray mammography: methods and results," *Proc. of SPIE*, Vol. 6431 64310F-1, 2007.
- [87] R. X. Xu, D. C. Young, J. J. Mao, S. P. Povoski, "A prospective pilot clinical trial evaluating the utility of a dynamic near-infrared imaging device for characterizing suspicious breast lesions," *Breast Cancer Research*, Vol. 9-6, pp. 1-12, 2007.
- [88] B. J. Tromberg, N. Shah, R. Lanning, A. Cerussi, J. Espinoza, T. Pham, L. Svaasand, and J. Butler, "Non-invasive in vivo characterization of breast tumors using photon migration spectroscopy," *Neoplasia* Vol. 2 (12), pp. 2640, 2000.
- [89] V. Ntziachristos, B. Chance, "Probing physiology and molecular function using optical imaging: applications to breast cancer," *Breast Cancer Res.*, Vol. 3, pp. 41-46, 2001.
- [90] P. Vaupel, A. Mayer, S. Briest, and M. Hockel, "Oxygenation gain factor: a novel parameter characterizing the association between hemoglobin level and the oxygenation status of breast cancers," *Cancer Res.*, Vol. 63, pp. 7634-7637, 2003.
- [91] B.D. Ripley, *Pattern Recognition and Neural Networks*, Cambridge:Cambridge University Press,1996.
- [92] J. A. Hanley, B. J. McNeil, "The meaning and use of the area under a receiver operating characteristic (ROC) curve," *Radiology*, vol. 143, pp. 29-36, 1982.
- [93] J. A. Hanley, B. J. McNeil, "A method of comparing the areas under receiver operating characteristic curves derived from the same cases," *Radiology*, vol. 148, pp. 839-843, 1983.

- [94] B. Chance, S. Nioka, J. Zhang, E. F. Conant, E. Hwang, S. Briest, S. G. Orel, M. D. Schnall, B. J. Czerniecki, "Breast cancer detection based on incremental biochemical and physiological properties of breast cancers: a six-year, two-site study," *Academic Radiology*, Vol. 12, Issue 8, pp. 925-933, 2005.
- [95] S. Fantini, D. Hueber, M. A. Franceschini, E. Gratton, W. Rosenfeld, P. G. Stubblefield, D. Maulik, M. R. Stankovic, "Non-invasive optical monitoring of the newborn piglet brain using continuous-wave and frequency-domain spectroscopy," *Phys. Med. Biol.*, Vol. 44, pp. 1543-1563, 1999.
- [96] D. Fradkin and I. Muchnik "Support Vector Machines for Classification", *DIMACS Series in Discrete Mathematics and Theoretical Computer Science*, vol. 70, pp. 13-20, 2006.
- [97] P. H. Chen, C. J. Lin, and B. Scholkopf, "A tutorial on support vector machines," *Appl. Stoch. Models. Bus. Ind.* vol. 21, pp. 111-136, 2005.
- [98] N. Cristianini and J. Shawe-Taylor, *An Introduction to Support Vector Machines*, Cambridge: Cambridge University Press, 2000.
- [99] K. Fukunaga, *Introduction to Statistical Pattern Recognition*, New York: Academic Press, 1990.
- [100] R. O. Duda, P. E. Hart, D. G. Stork, *Pattern Classification*, New York: Wiley-Interscience, 2000.

Appendix

Key Publications

Pharmacokinetic-rate images of indocyanine green for breast tumors using near-infrared optical methods

Burak Alacam¹, Birsen Yazici^{1,2}, Xavier Intes², Shoko Nioka³ and Britton Chance³

¹ Department of Electrical, Computer, and Systems Engineering, Rensselaer Polytechnic Institute, Troy, NY, USA

² Department of Biomedical Engineering, Rensselaer Polytechnic Institute, Troy, NY, USA

³ Department of Biophysics and Biochemistry, University of Pennsylvania, PA, USA

E-mail: yazici@ecse.rpi.edu

Received 12 October 2007, in final form 30 November 2007

Published 15 January 2008

Online at stacks.iop.org/PMB/53/837

Abstract

In this paper, we develop a method of forming pharmacokinetic-rate images of indocyanine green (ICG) and apply our method to *in vivo* data obtained from three patients with breast tumors. To form pharmacokinetic-rate images, we first obtain a sequence of ICG concentration images using the differential diffuse optical tomography technique. We next employ a two-compartment model composed of plasma, and extracellular–extravascular space (EES), and estimate the pharmacokinetic rates and concentrations in each compartment using the extended Kalman filtering framework. The pharmacokinetic-rate images of the three patient show that the rates from the tumor region and outside the tumor region are statistically different. Additionally, the ICG concentrations in plasma, and the EES compartments are higher around the tumor region agreeing with the hypothesis that around the tumor region ICG may act as a diffusible extravascular flow in compromised capillary of cancer vessels. Our study indicates that the pharmacokinetic-rate images may provide superior information than single set of pharmacokinetic rates estimated from the entire breast tissue for breast cancer diagnosis.

(Some figures in this article are in colour only in the electronic version)

1. Introduction

Near-infrared (NIR) diffuse optical imaging offers several advantages over other imaging modalities (Arridge 1999, Boppart *et al* 2004, Gu *et al* 2004, Intes and Chance 2005, Mahmood *et al* 1999, Sevick-Muraca *et al* 1997, Yodh and Chance 1995). NIR techniques are minimally invasive, easy to use, relatively inexpensive and can be made portable. Moreover, optical

techniques, when coupled with contrast agents, have the potential to provide molecular/cellular level information, which can improve cancer detection, staging and treatment monitoring (Alacam *et al* 2006, Cuccia *et al* 2003, Intes *et al* 2003, Mahmood *et al* 1999, Sevick-Muraca *et al* 1997).

Among many commercially available optical contrast agents, only indocyanine green (ICG) is approved for use in humans by the Food and Drug Administration (ElDeosky *et al* 1999, Hansen *et al* 1993, Shinohara *et al* 1996). ICG is a blood pooling agent that has different delivery behavior between normal and cancer vasculature. In normal tissue, ICG acts as a blood flow indicator in tight capillaries of normal vessels. However in tumors, ICG may act as a diffusible (extravascular) flow in leaky capillary of vessels (Alacam *et al* 2006, Cuccia *et al* 2003, Ntziachristos *et al* 2000, Vaupel *et al* 1991). Therefore, pharmacokinetics of ICG has the potential to provide new tools for tumor detection, diagnosis and staging.

One approach to analyze pharmacokinetics of contrast agents is the compartmental modeling (Anderson 1983, Jacquez 1972, Tornøe 2002). A number of studies using compartmental modeling were reported to show the feasibility of ICG pharmacokinetics in tumor characterization (Alacam *et al* 2006, Cuccia *et al* 2003, Intes *et al* 2003). Cuccia *et al* (2003) presented a study of the dynamics of ICG in an adenocarcinoma rat tumor model using a two-compartment model. Intes *et al* (2003) presented the uptake of ICG in breast tumors using a continuous wave diffuse optical tomography apparatus using a two-compartment model. We recently introduced the extended Kalman filtering (EKF) framework to model and estimate the ICG pharmacokinetics and tested three different compartmental models for the ICG pharmacokinetics using the *in vivo* NIR data collected from Fischer rats with cancerous tumors (Alacam *et al* 2006). Our study suggests that the pharmacokinetic rates out of the vasculature are higher in edematous tumors as compared to necrotic tumors.

In all the studies described above, the pharmacokinetic rates are assumed to be constant over a tissue volume that may be as large as the entire imaging domain. However, pharmacokinetic rates are expected to be different in healthy and tumor tissue as reported in positron emission tomography (PET) and magnetic resonance imaging (MRI) literature. It was shown that the spatially resolved pharmacokinetic-rate analysis provides increased sensitivity and specificity for breast cancer diagnosis (Mussurakis *et al* 1997, Su *et al* 2005, Sun *et al* 2006). For example, Sun *et al* (2006) showed that FAU (1-2'-deoxy-2'-fluoro- β -D-arabinofuranosyl urasil, a PET contrast agent) accumulation in tumor regions is significantly higher when compared to normal breast tissue based on pharmacokinetic-rate images. Mussurakis *et al* (1997) showed that the pharmacokinetics of gadolinium-DTPA (an MRI contrast agent) can be used to differentiate between malignant and benign breast tumors with a high accuracy. It has also been shown that the spatially resolved image interpretation is superior to the isolated use of quantitative pharmacokinetic rates.

In the area of diffuse NIR spectroscopy and imaging, a number of studies on spatially resolved pharmacokinetic rates has been reported (Gurfinkel *et al* 2000, Milstein *et al* 2005). Gurfinkel *et al* (2000) presented *in vivo* NIR reflectance images of ICG pharmacokinetics to discriminate canine adenocarcinoma (located at 0.5–1 cm depth) from normal mammary tissue. These images were generated by a non-tomographic technique using a CCD camera that is suitable only for imaging tumors close to surface. Milstein *et al* (2005) presented a Bayesian tomographic image reconstruction method to form pharmacokinetic-rate images of optical fluorophores based on fluorescence diffuse optical tomography. Numerical simulations show that the method provides good contrast. However, no real data experiments were presented to study the diagnostic value of spatially resolved pharmacokinetic rates.

In this paper, we present a method of forming pharmacokinetic-rate images and report spatially resolved pharmacokinetic rates of ICG using *in vivo* NIR data acquired from three

patients with breast tumors. To the best of our knowledge, our work is the first study presenting the pharmacokinetic-rate images of an optical contrast agent using *in vivo* breast data based on tomographic techniques. We first develop a set of spatio-temporally resolved ICG concentration images based on differential diffuse optical tomography. We model the ICG pharmacokinetics by a two-compartment model composed of plasma and extracellular-extravascular space (EES) compartments. We then estimate the ICG pharmacokinetic rates and the concentrations in different compartments based on the EKF framework (Alacam *et al* 2006). We show that the pharmacokinetic rates from the tumor region and outside the tumor region are statistically different. We also estimate a single set of pharmacokinetic rates (bulk pharmacokinetic rates) for the entire breast tissue. Our study indicates that spatially resolved pharmacokinetic rates provide more consistent and superior diagnostic information as compared to the bulk pharmacokinetic rates.

The rest of the paper is organized as follows. In section 2, we present the reconstruction of ICG concentration images. In section 3, we present modeling and estimation of ICG pharmacokinetic-rate images using the EKF framework. In section 4, we present the spatially resolved ICG pharmacokinetic-rate analysis of *in vivo* breast data. Section 5 summarizes our results and conclusion.

2. Reconstruction of bulk ICG concentration images

In our data collection process, a sequence of boundary measurements are collected over a period of time. Each set of measurements are used to form a frame of the ICG concentration images. The resulting sequence of ICG concentration images are then used to form pharmacokinetic-rate images. To reconstruct each frame of the ICG concentration images, we follow a static reconstruction approach and use differential diffuse optical tomography (DDOT) technique (Intes *et al* 2003, Ntziachristos *et al* 1999).

In DDOT, two sets of excitation measurements are collected corresponding to before and after the ICG injection, and the ICG concentration is determined by the perturbation method (Intes *et al* 2003, Ntziachristos *et al* 1999). The photon propagation before and after the injection is modeled by the following diffusion equations:

$$\nabla \cdot D_x(r) \nabla \Phi_x^\pm(r, \omega) - (\mu_{ax}^\pm(r) + j\omega/c) \Phi_x^\pm(r, \omega) = 0, \quad r \in \Omega \subset R^3, \quad (1)$$

with Robin-type boundary conditions:

$$2D_x(r) \frac{\partial \Phi_x^\pm(r, \omega)}{\partial \nu} + \rho \Phi_x^\pm(r, \omega) = -S(r, \omega), \quad r \in \partial\Omega, \quad (2)$$

where x stands for the excitation, c is the speed of light inside the medium Ω ; ω denotes the modulation frequency of the source, $\mu_{ax}^-(r)$ and $\mu_{ax}^+(r)$ are the absorption coefficients before and after the ICG injection, D_x is the diffusion coefficient which is assumed independent of μ_{ax}^\pm , known but not necessarily constant, $\Phi_x^\pm(r, \omega)$ denotes optical field at location r before and after the ICG injection. Here, ν denotes the outward normal to the boundary $\partial\Omega$ of Ω , ρ is a constant representing the refractive index mismatch between the two regions separated by $\partial\Omega$ and $S(r, \omega)$ is the excitation source on the boundary.

The absorption coefficients after the injection μ_{ax}^+ are modeled as a sum of the absorption coefficient of the medium before the ICG injection μ_{ax}^- and the perturbation caused by the ICG $\Delta\mu_{ax}(r)$:

$$\Delta\mu_{ax}(r) = \mu_{ax}^+(r) - \mu_{ax}^-(r), \quad r \in \Omega \subset R^3. \quad (3)$$

In the forward model, the analytical solutions of the heterogenous diffusion equation given in (1) is derived using first-order Rytov approximation (Intes *et al* 2003). The sample volume

is divided into a set of voxels and the measurements are related to the relative absorption coefficients of each voxel by a system of linear equations. The shape of the breast was approximated as a cylinder and the Kirchhoff approximation (Ripoll *et al* 2001a, 2001b) for diffuse waves was used to model the interaction of light with boundaries. In order to minimize optode-tissue coupling mismatch due to breathing motion, the forward model was augmented with the coupling coefficient technique as described in Boas *et al* (2001).

Here, the Rytov-type measurements, which are defined by the natural logarithm of the ratio of the post-ICG measurements to the pre-ICG measurements were used (Ntziachristos *et al* 1999). Let $\Psi_x(\omega; r_d; r_s)$ denote the Rytov-type measurements at location r_d due to source at r_s . The linearized relationship between the differential absorption coefficient and measurements is given by O’Leary (1996)

$$\Psi_x(\omega; r_d; r_s) = -\frac{1}{\Phi_x^-(\omega; r_d; r_s)} \int_{\Omega} G_x^-(r, \omega; r_d) I_x(r) \Phi_x^-(r, \omega; r_s) d^3r, \quad (4)$$

where $\Phi_x^-(r, \omega; r_s)$ is the photon density obtained at the excitation wavelength before ICG injection, $I_x(r) = c\Delta\mu_{ax}(r)/D_x$, and $G_x^-(r, \omega; r_d)$ is the Green’s function of (1) for a source at r_s before the injection.

We address the inverse problem of recovering $\Delta\mu_{ax}$ from Rytov measurements Ψ_x based on the forward model (4) using the singular-value decomposition of the Moore–Penrose generalized system. We use a zeroth-order Tikhonov regularization to stabilize the inversion procedure. The regularization parameter was determined by L -curve analysis (Hansen and O’Leary 1993) using the data obtained from a phantom study previously employed to validate the apparatus (Intes *et al* 2003). The optimal regularization parameter was found to be 6×10^{-4} and set to be the same for all patient images and time instances. A detailed discussion of the forward and inverse models used for the reconstruction of differential absorption coefficients ($\Delta\mu_{ax}$) can be found in Intes *et al* (2003).

To construct a set of ICG concentration images, we use the linear relationship between the differential absorption coefficients and ICG concentrations (Landsman *et al* 1976),

$$\Delta\mu_a(r) = \ln 10 \epsilon_{\lambda} m(r), \quad (5)$$

where ϵ_{λ} is the extinction coefficient of ICG at the wavelength 805 nm, $m(r)$ is the bulk ICG concentration in the tissue and $\Delta\mu_a(r)$ is as defined in (3).

Note that the method described here is applicable for frequency domain case but for simplicity we set the frequency to zero, i.e. $\omega = 0$.

3. Modeling and estimation of ICG pharmacokinetics

3.1. Two-compartment model of ICG pharmacokinetics

Using the method outlined in section 2, we reconstruct a sequence of ICG concentration images. As an example, figures 1–3 show a set of images reconstructed from *in vivo* breast data.

Our objective is to model the pharmacokinetics of ICG at each voxel of ICG concentration images using compartmental modeling. To do so, we first extracted the time varying ICG concentration curves for each voxel from the sequence of ICG concentration images. An example of such a curve is shown in figure 4. We next fit a two-compartment model to each ICG concentration curve (Alacam *et al* 2006, Gurfinkel *et al* 2000).

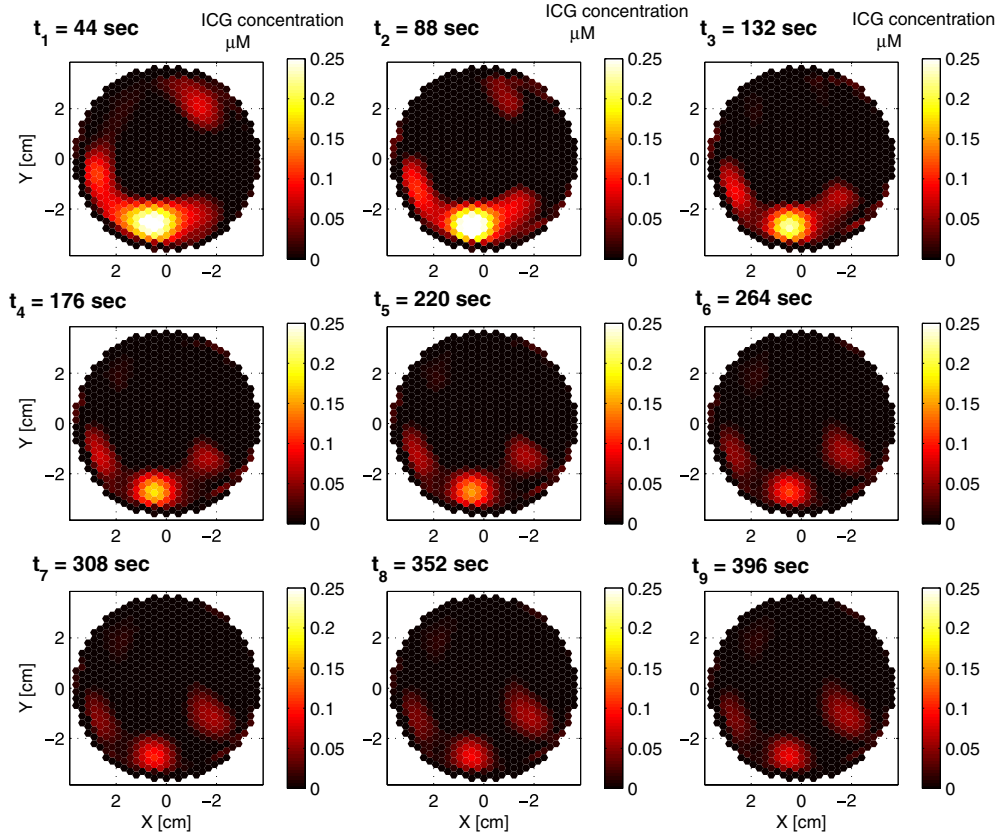


Figure 1. ICG concentration images for a set of time instants for case 1.

Using the two-compartment model introduced by Alacam *et al* (2006), ICG transition between plasma and extracellular–extravascular space (EES) can be modeled as follows:

$$\begin{bmatrix} \dot{C}_e(t) \\ \dot{C}_p(t) \end{bmatrix} = \begin{bmatrix} -k_{out} & k_{in} \\ k_{out} & -(k_{in} + k_{elm}) \end{bmatrix} \begin{bmatrix} C_e(t) \\ C_p(t) \end{bmatrix} + \omega(t), \quad t \in [T_0, T_1], \quad (6)$$

where $C_p(t)$ and $C_e(t)$ represent the ICG concentrations in plasma and EES at time t , respectively. The rates k_{in} , k_{out} and k_{elm} have a unit of sec^{-1} . They are defined as the permeability surface area products given by $PS\gamma$, where P is the capillary permeability constant, S is the capillary surface area and γ is the tissue density. k_{in} and k_{out} govern the leakage into and the drainage out of the EES. The parameter k_{elm} describes the ICG elimination from the body through kidneys and liver. Here, $\omega(t)$ is uncorrelated zero-mean Gaussian process with covariance matrix \mathbf{Q} representing the model mismatch.

The actual total ICG concentration in the tissue is a linear combination of plasma and the EES ICG concentrations, and modeled as

$$m(t) = \begin{bmatrix} v_e & v_p \end{bmatrix} \begin{bmatrix} C_e(t) \\ C_p(t) \end{bmatrix} + \eta(t), \quad t \in [T_0, T_1], \quad (7)$$

where $m(t)$, $C_e(t)$ and $C_p(t)$ are defined in (5) and (6), v_p and v_e are plasma and the EES volume fractions, respectively, and $\eta(t)$ is uncorrelated zero-mean Gaussian process with covariance matrix \mathbf{R} , representing the measurement noise.

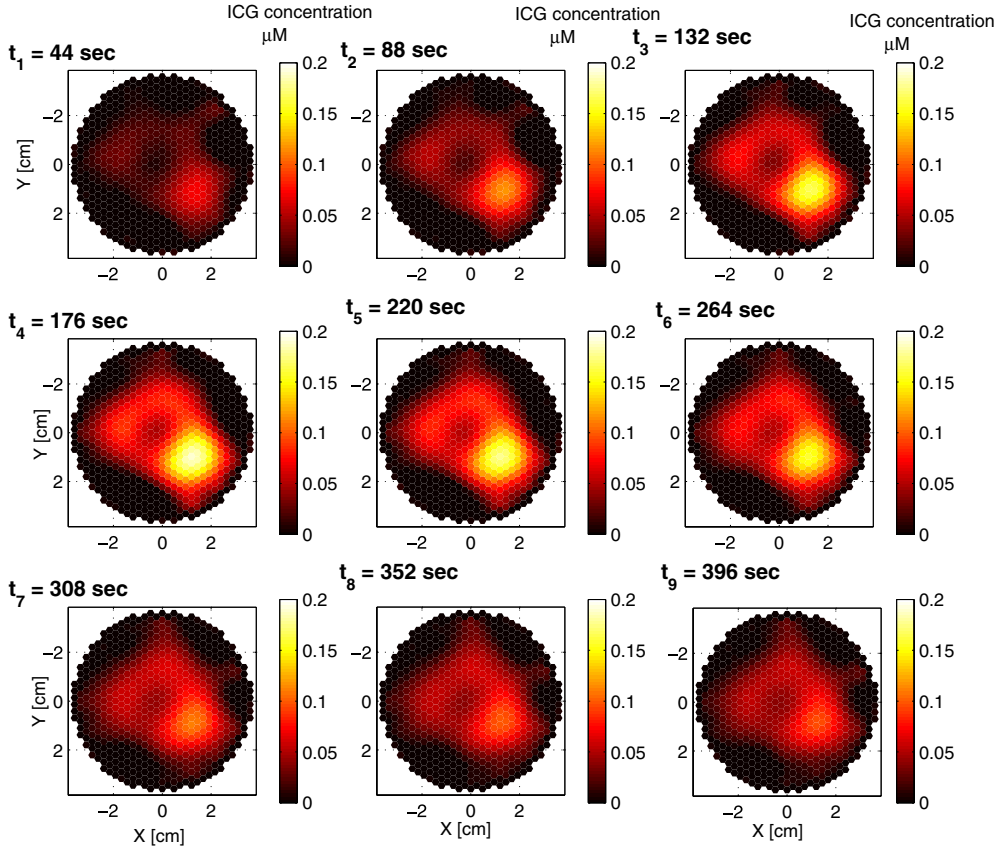


Figure 2. ICG concentration images for a set of time instants for case 2.

3.2. Estimation of ICG pharmacokinetics using extended Kalman filtering

In matrix–vector notation, (6) and (7) can be expressed as

$$\dot{\mathbf{C}}(t) = \mathbf{K}(\alpha)\mathbf{C}(t) + \omega(t), \quad m(t) = \mathbf{V}(\alpha)\mathbf{C}(t) + \eta(t), \quad (8)$$

where $\mathbf{C}(t)$ denotes the concentration vector with elements $C_e(t)$, and $C_p(t)$; $\mathbf{K}(\alpha)$ is the system matrix, $\mathbf{V}(\alpha)$ is the measurement matrix as defined in equation (7) and α is the parameter vector given by

$$\alpha = [k_{\text{out}} \quad k_{\text{in}} \quad k_{\text{elm}} \quad v_e \quad v_p]^T. \quad (9)$$

The ICG measurements in (8) are collected at discrete time instances, $t = kT$, $k = 0, 1, \dots$, where T is the sampling period. Therefore, the continuous model described in (8) is discretized. We can express the discrete compartmental model as follows:

$$\mathbf{C}_d(k+1) = \mathbf{K}_d(\theta)\mathbf{C}_d(k) + \omega_d(k), \quad \mathbf{m}(k) = \mathbf{V}_d(\theta)\mathbf{C}_d(k) + \eta_d(k), \quad (10)$$

where $\mathbf{K}_d(\theta) = e^{\mathbf{K}(\alpha)T}$ is the discrete time system matrix; $\mathbf{V}_d(\theta) = \mathbf{V}(\alpha)$ is the discrete measurement matrix; $\omega_d(k)$ and $\eta_d(k)$ are zero-mean Gaussian white noise processes with covariances matrix \mathbf{Q}_d and variance \mathbf{R}_d , respectively. The vector θ is composed of parameters τ_{ij} which are functions the pharmacokinetic rates and volume fractions:

$$\theta = [\tau_{11} \quad \tau_{12} \quad \tau_{21} \quad \tau_{22} \quad v_e \quad v_p]^T. \quad (11)$$

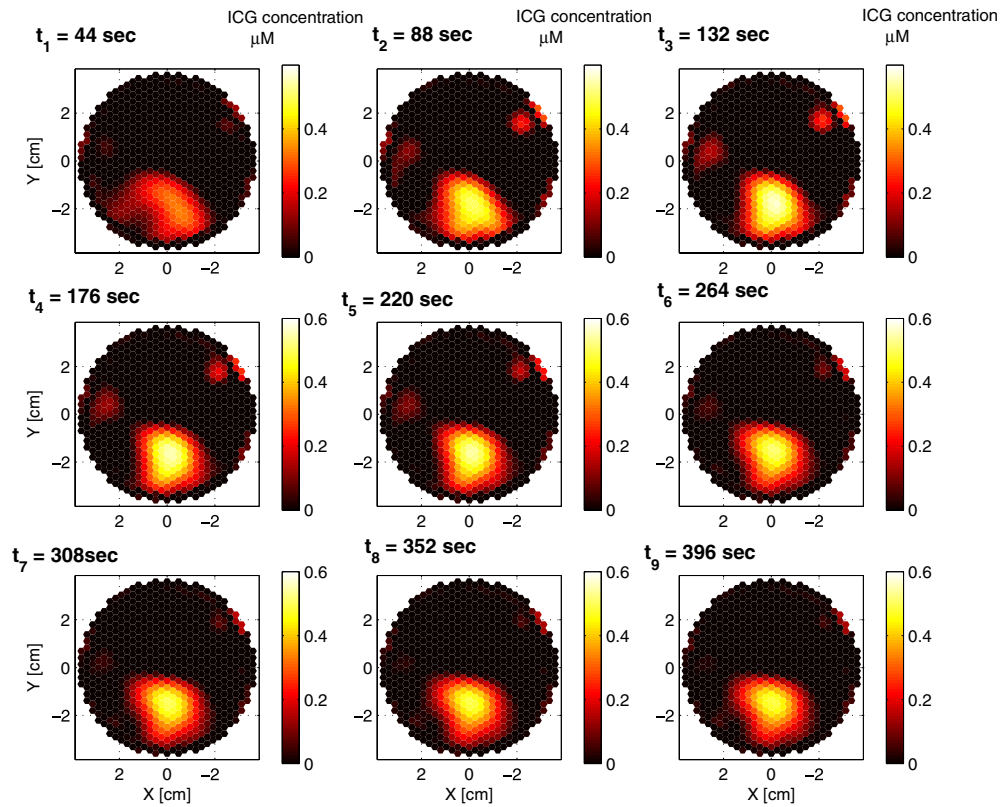


Figure 3. ICG concentration images for a set of time instants for case 3.

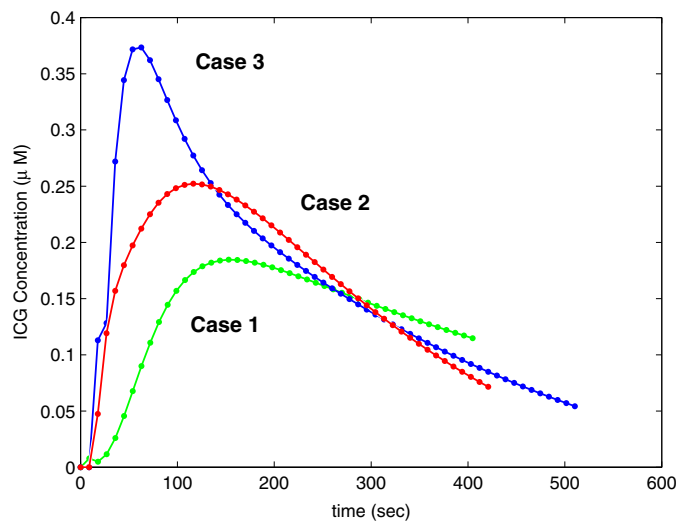


Figure 4. Time course of ICG concentration curves for a specific voxel, 65th, 276th, 188th voxel for cases 1, 2 and 3, respectively.

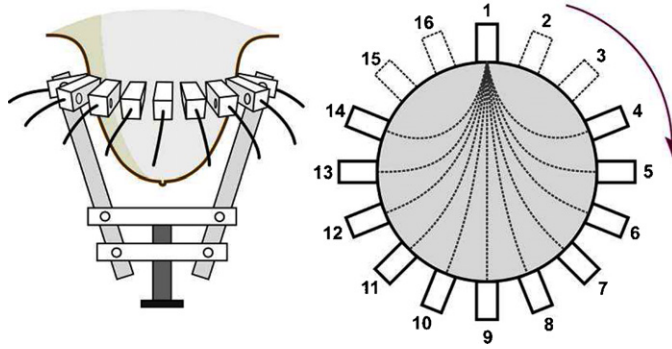


Figure 5. (Left) Schematic diagram. (Right) The cut section of the CW NIR imaging apparatus with 16 sources and detectors.

We first estimate τ_{ij} , $i, j = 1, 2$ and then compute the pharmacokinetic rates k_{in} , k_{out} and k_{elm} (Alacam *et al* 2006, Chen 1999). The explicit form of the discrete state-space model is given as follows:

$$\begin{aligned} \begin{bmatrix} C_e(k+1) \\ C_p(k+1) \end{bmatrix} &= \begin{bmatrix} \tau_{11} & \tau_{12} \\ \tau_{21} & \tau_{22} \end{bmatrix} \begin{bmatrix} C_e(k) \\ C_p(k) \end{bmatrix} + \omega_d(k) \\ m(k) &= \begin{bmatrix} v_e & v_p \end{bmatrix} \begin{bmatrix} C_e(k) \\ C_p(k) \end{bmatrix} + \eta_d(k). \end{aligned} \quad (12)$$

We estimate the parameter vector θ and concentration vector C_d by using the EKF framework. The EKF is a recursive modeling and estimation method with numerous advantages in ICG pharmacokinetic modeling (Alacam *et al* 2006). These include effective modeling of multiple compartments, and multiple measurement systems in the presence of measurement noise and uncertainties in the compartmental model dynamics, simultaneous estimation of model parameters and ICG concentrations in each compartment, statistical validation of estimated concentrations and error bounds on the model parameter estimates, and incorporation of available a priori information about the initial conditions of the permeability rates into the estimation procedure.

When both states (ICG concentrations) and model parameters (pharmacokinetic rates and volume fractions) are unknown, a linear state-space model can be regarded as a nonlinear model; the linear system parameters and states combine to form the new states of the nonlinear model. This system is then linearized and the new unknown states are found using the EKF estimator (Alacam *et al* 2006, Ljung 1979, Togneri and Deng 2003, Nelson and Stear 1976). In EKF framework, θ can be treated as a random process with the following model:

$$\theta(k+1) = \theta(k) + \varsigma_d(k), \quad (13)$$

where $\varsigma_d(k)$ is a zero-mean Gaussian process with covariance matrix S_d .

Table 1 summarizes the joint estimation of pharmacokinetic rates and ICG concentration in different compartments. In table 1, $\hat{C}_d(k|k-1)$ is the state estimate propagation at step k given all the measurements up to step $k-1$, $\hat{C}_d(k)$ is the state estimate update at step k , $P_{k,k-1}$ denotes the error covariance propagation at step k given all the measurements up to step $k-1$, $P_{k,k}$ is the error covariance update at step k , S_d is the preassigned covariance matrix of $\varsigma_d(k)$, J_k is the Jacobian matrix due to iterative linearization of the state equation at step k , G_k is the recursive Kalman gain at step k , R_d is the covariance matrix of the measurements, Q_d is the covariance matrix of the concentration vector and I is the identity matrix. A detailed

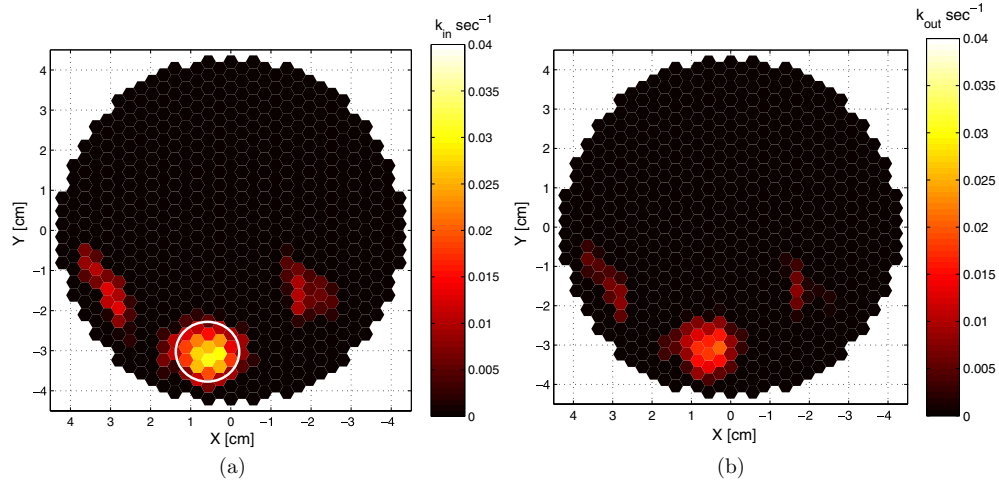


Figure 6. Pharmacokinetic rate images, (a) k_{in} and (b) k_{out} for case 1. The k_{in} images are shown with approximate tumor location and size.

Table 1. EKF algorithm for simultaneous estimation of states and parameters.

| | |
|------------------------------|--|
| Initial conditions | $\begin{bmatrix} \hat{\mathbf{C}}_d(0) \\ \hat{\boldsymbol{\theta}}(0) \end{bmatrix} = \begin{bmatrix} E(\mathbf{C}_d(0)) \\ \hat{\boldsymbol{\theta}}(0) \end{bmatrix}, \mathbf{P}_{0,0} = \begin{bmatrix} Var(\mathbf{C}_d(0)) & 0 \\ 0 & \mathbf{S}_d \end{bmatrix}$ |
| State estimate propagation | $\begin{bmatrix} \hat{\mathbf{C}}_d(k k-1) \\ \hat{\boldsymbol{\theta}}(k k-1) \end{bmatrix} = \begin{bmatrix} \mathbf{K}_d(\hat{\boldsymbol{\theta}}(k-1))\hat{\mathbf{C}}_d(k-1) \\ \hat{\boldsymbol{\theta}}(k-1) \end{bmatrix}$ |
| Error covariance propagation | $\mathbf{P}_{k,k-1} = \mathbf{J}_{k-1}\mathbf{P}_{k-1,k-1}\mathbf{J}_{k-1}^T + \begin{bmatrix} \mathbf{Q}_d & 0 \\ 0 & \mathbf{S}_d \end{bmatrix}$ |
| State estimate update | $\begin{bmatrix} \hat{\mathbf{C}}_d(k) \\ \hat{\boldsymbol{\theta}}(k) \end{bmatrix} = \begin{bmatrix} \hat{\mathbf{C}}_d(k k-1) \\ \hat{\boldsymbol{\theta}}(k k-1) \end{bmatrix} + \mathbf{G}_k(\mathbf{m}(k) - \mathbf{V}_d(\hat{\boldsymbol{\theta}}(k k-1))\hat{\mathbf{C}}_d(k k-1))$ |
| Error covariance update | $\mathbf{P}_{k,k} = [\mathbf{I} - \mathbf{G}_k\Lambda_{k k-1}]\mathbf{P}_{k,k-1}$ |
| Kalman gain | $\mathbf{G}_k = \mathbf{P}_{k,k-1}\Lambda_{k k-1}^T[\Lambda_{k k-1}\mathbf{P}_{k,k-1}\Lambda_{k k-1}^T + \mathbf{R}_d]^{-1}$ |
| Definitions | $\mathbf{J}_k = \begin{bmatrix} \mathbf{K}_d(\hat{\boldsymbol{\theta}}(k)) & \frac{\partial}{\partial \boldsymbol{\theta}}[\mathbf{K}_d(\hat{\boldsymbol{\theta}}(k))\hat{\mathbf{C}}_d(k)] \\ \mathbf{0} & \mathbf{I} \end{bmatrix}$ $\Lambda_{k k-1} = \begin{bmatrix} \mathbf{V}_d(\hat{\boldsymbol{\theta}}(k k-1)) \\ 0 \end{bmatrix}^T$ |

discussion of the extended Kalman filtering algorithm, and the initialization of the parameters, concentrations and covariance matrices can be found in Alacam *et al* (2006).

4. Spatially resolved ICG pharmacokinetic rate analysis of *in vivo* breast data

4.1. Apparatus

In this work, we use the data collected with a continuous wave (CW) NIR imaging apparatus. The apparatus has 16 light sources, which are tungsten bulbs with less than 1 W of output power. They are located on a circular holder at an equal distance from each other with 22.5°

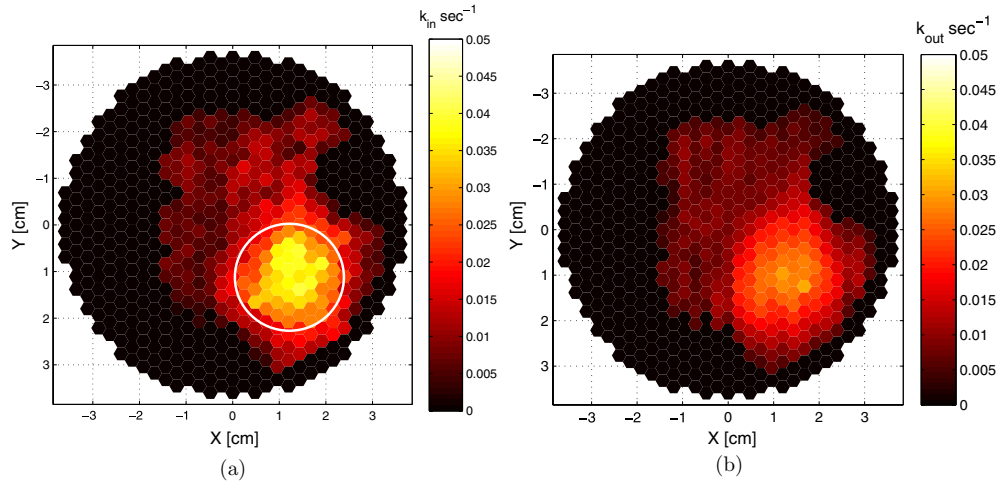


Figure 7. Pharmacokinetic-rate images, (a) k_{in} and (b) k_{out} for case 2. The k_{in} images are shown with approximate tumor location and size.

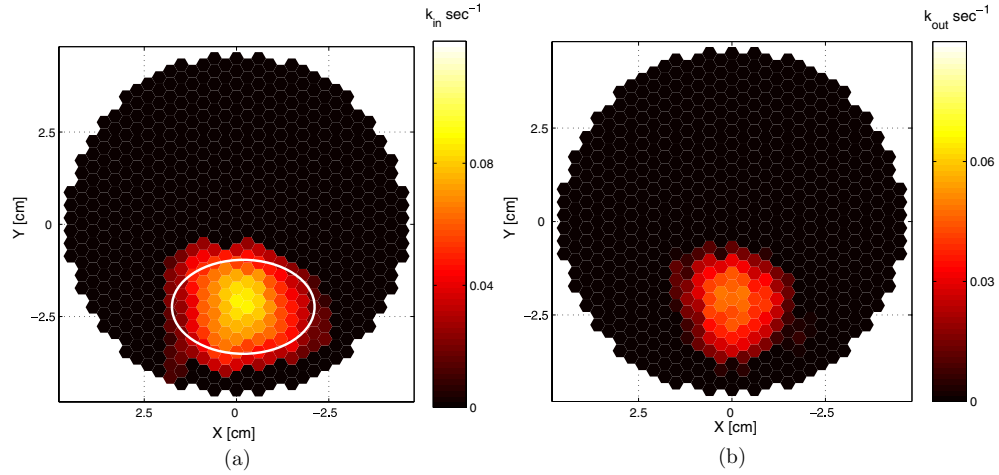


Figure 8. Pharmacokinetic-rate images, (a) k_{in} and (b) k_{out} for case 3. The k_{in} images are shown with approximate tumor location and size.

apart. Sixteen detectors, namely silicon photodiodes, are situated in the same plane. The breast is arranged in a pendular geometry with the source-detector probes gently touching its surface. Figure 5 illustrates the configuration of the apparatus and the configuration of the detectors and the sources in a circular plane. Note that sources and detectors are co-located. The detectors use the same positions as the sources to collect the light originating from one source at a time. Only the signals from the farthest 11 detectors are used in the analysis. For example, when source 1 is on, the data are collected using detectors 4–14. This provides sufficient number of source-detector readings (176 readings) to reconstruct $\Delta\mu_a$ images at each time instant. A band pass filter at 805 nm, the absorption peak of ICG, is placed in front of the sources to select the desired wavelength. A set of data for one source is collected every

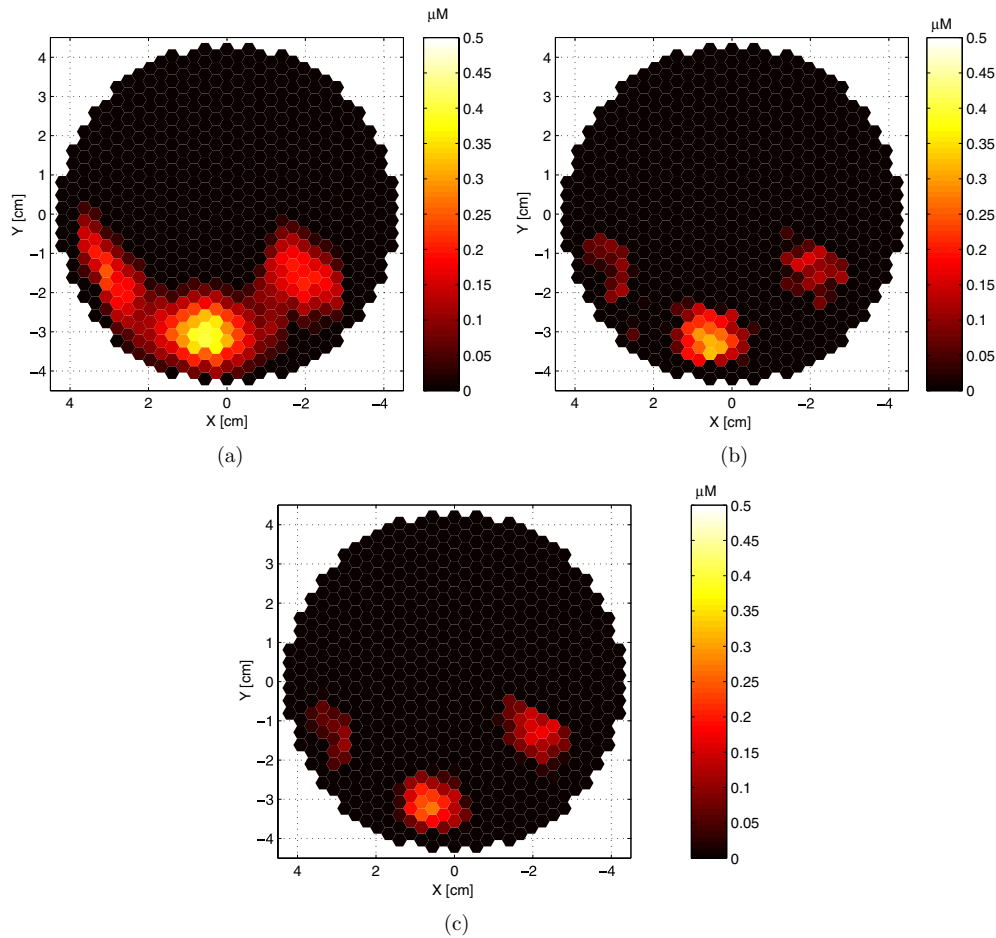


Figure 9. ICG concentration images in plasma for case 1 for (a) 246.4th, (b) 334.4th and (c) 422.4th s.

~500 ms. The total time for a whole scan of the breast including 16 sources and 16 detectors is ~8.8 s. A more detailed explanation of the apparatus and the data collection procedure can be found in (Nioka *et al* 1997).

4.2. Tumor information and protocol

Three different patients with different tumor types are included in this study. Measurements are made before the biopsy to avoid modification of the blood volume and flow in the tumor region. First case (case 1) is fibroadenoma, which corresponds to a mass estimated to be 1–2 cm in diameter within a breast of 9 cm diameter located at 6–7 o'clock. Second case (case 2) is adenocarcinoma corresponding to a tumor estimated to be 2–3 cm in diameter within a breast of 7.7 cm diameter located at 4–5 o'clock. The third case (case 3) is invasive ductal carcinoma, which corresponds to a mass estimated to be 4 cm by 3 cm located at 6 o'clock. Table 2 describes the tumor information for each patient. *A priori* information on the location and size of the tumor was obtained by palpation and the diagnostic information

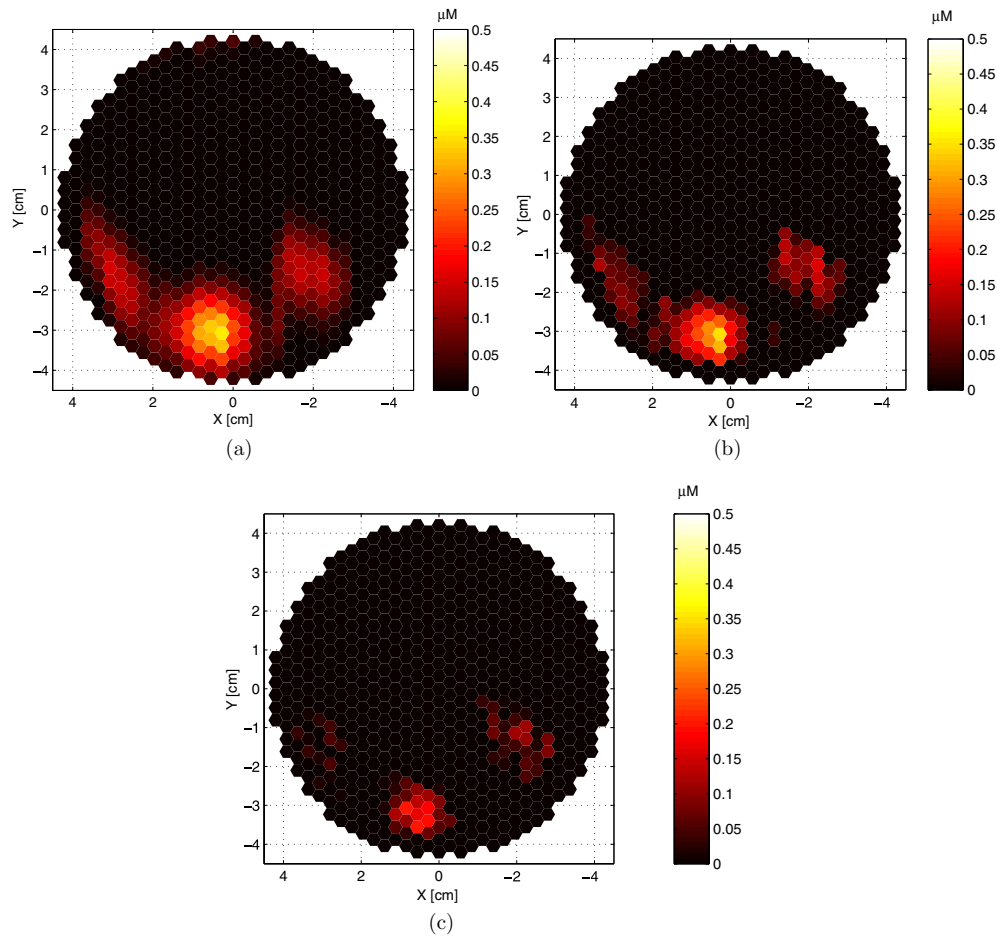


Figure 10. ICG concentration images in the EES for case 1 for (a) 246.4th, (b) 334.4th and (c) 422.4th s.

Table 2. Tumor information for each patient.

| | Tumor type | Tumor size | Tumor location |
|--------|---------------------------|--------------|----------------|
| Case 1 | Fibroadenoma | 1–2 cm | 6–7 o'clock |
| Case 2 | Adenocarcinoma | 2–3 cm | 4–5 o'clock |
| Case 3 | Invasive ductal carcinoma | 4 cm by 3 cm | 6 o'clock |

was derived *a posteriori* from biopsy and surgery. ICG is injected intravenously by bolus with a concentration of 0.25 mg kg^{-1} of body weight. Data acquisition started before the injection of ICG and continued for 10 min.

4.3. Results and discussion

Using the CW imager described above, source–detector readings were collected from different angles for each patient. Differential absorption coefficient images were reconstructed based

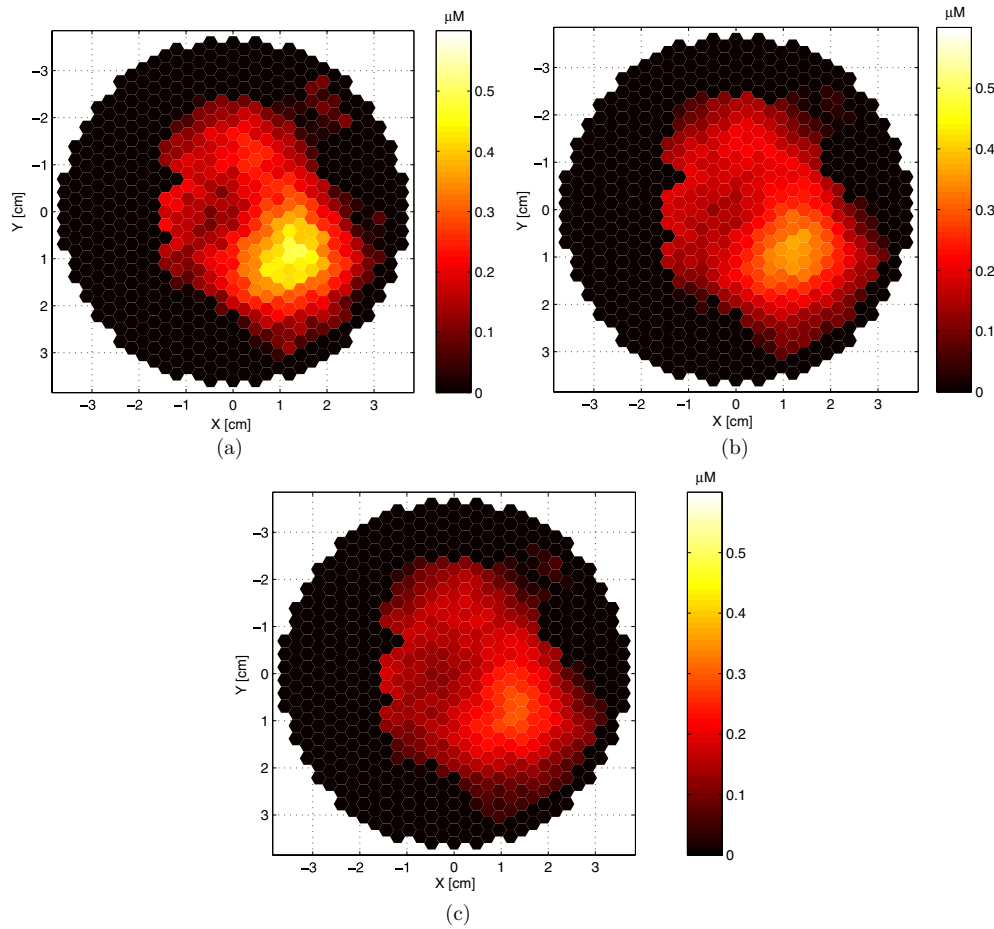


Figure 11. ICG concentration images in plasma for case 2 for (a) 228.8th, (b) 316.8th and (c) 404.8th s.

on DDOT forward model given in equations (1)–(4) with ω set to zero. Using the linear relationship (5) between ICG concentration and absorption coefficient, ICG concentration images were obtained for each case. A sample set of ICG concentration images for the selected time instants are shown in figures 1–3 for cases 1–3, respectively. Although only nine images are displayed, there are approximately 50 images for each case, each corresponding to a different time instant. Each image is composed of 649 voxels. Note that the ICG concentration images in figures 1–3 represent the bulk ICG concentrations in the tissue, not the ICG concentrations in plasma or the EES compartments.

We next extracted the time course of ICG concentration for each voxel. As an example, figure 4 shows the time course of ICG concentrations for all three cases for a specific voxel in the tumor region (65th, 276th, 188th voxel for cases 1, 2 and 3, respectively). We then fit the two-compartment model to each time course data using the EKF framework; and estimated k_{in} , k_{out} , k_{elim} , and the ICG concentrations in plasma and the EES. We chose initial values within the biological limits that lead to minimum norm error covariance matrix. The images of k_{in} and k_{out} for each case are shown in figures 6(a)–(b), and 7(a)–(b), 8(a)–(b), respectively. Additionally, we constructed the ICG concentration images for plasma and

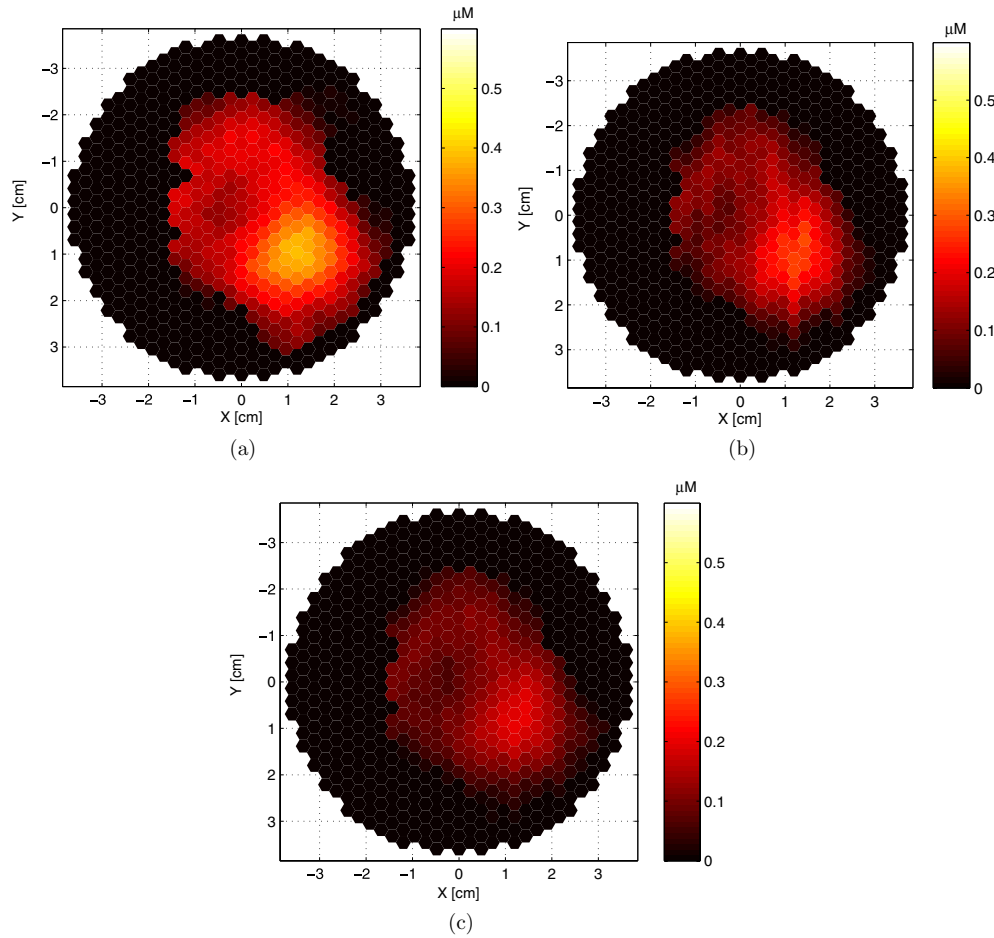


Figure 12. ICG concentration images in the EES for case 2 for (a) 228.8th, (b) 316.8th and (c) 404.8th s.

the EES compartments. Figures 9–14 show the ICG concentration in plasma and the EES for three different time instants for cases 1, 2 and 3, respectively. Our results show that the pharmacokinetic rates are higher around the tumor region agreeing with the fact that permeability increases around the tumor region due to compromised capillaries of tumor vessels. We also observed that ICG concentrations in plasma and the EES compartments are higher around the tumors agreeing with the hypothesis that around the tumor region ICG may act as a diffusible extravascular flow in leaky capillary of tumor vessels.

Using the *a priori* and *a posteriori* information on the location, and the size of the tumors, we plotted an ellipse (or a circle) to identify the approximate location and size of the tumor in the pharmacokinetic-rate images. We note that the radii of the ellipses were chosen large enough to include the tumor boundaries. Figures 6(a), 7(a) and 8(a) present the k_{in} images with approximate tumor location and size for cases 1, 2 and 3, respectively. The consistency of the bright regions in the k_{in} images, and circular/elliptical regions drawn based on the *a priori* and *a posteriori* information shows that the pharmacokinetic-rate images may provide good localization of tumors.

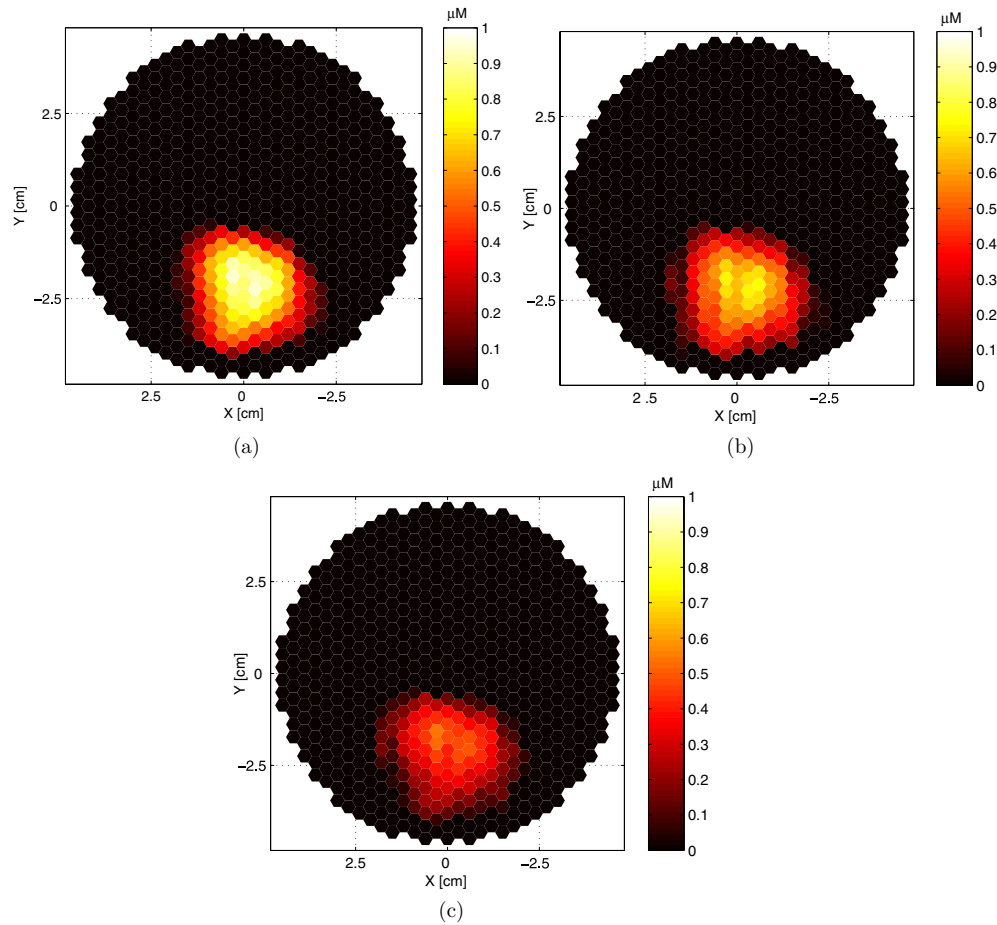


Figure 13. ICG concentration images in plasma for case 3 for (a) 246.4th, (b) 378.4th and (c) 510.4th s.

Table 3. Mean and standard deviation of pharmacokinetic rates for the tumor region and outside the tumor region.

| | $k_{in} (\text{sec}^{-1} 10^{-2})$ | | $k_{out} (\text{sec}^{-1} 10^{-2})$ | | $k_{elm} (\text{sec}^{-1} 10^{-3})$ | |
|--------|------------------------------------|------------------|-------------------------------------|------------------|-------------------------------------|------------------|
| | Inside | Outside | Inside | Outside | Inside | Outside |
| Case 1 | 2.14 ± 0.018 | 0.73 ± 0.011 | 1.24 ± 0.069 | 0.43 ± 0.013 | 4.11 ± 0.057 | 3.87 ± 0.012 |
| Case 2 | 2.92 ± 0.076 | 1.14 ± 0.052 | 1.58 ± 0.051 | 0.65 ± 0.036 | 3.94 ± 0.081 | 4.12 ± 0.047 |
| Case 3 | 6.87 ± 0.093 | 3.06 ± 0.015 | 4.96 ± 0.048 | 1.66 ± 0.072 | 4.49 ± 0.056 | 4.46 ± 0.081 |

The histograms of k_{in} and k_{out} images for the tumor region (as indicated by circular/elliptical regions) and outside the tumor region are shown in figures 15(a)–(c) and figures 16(a)–(c), respectively. Note that all nonzero voxels outside the elliptical region constitute ‘outside the tumor region’. The solid curves in figures 15 and 16 show the Gaussian fit. The histograms and their Gaussian fits in figures 15 and 16 show that the mean and the standard deviation of k_{in} and k_{out} values are different for the tumor and outside the tumor region. Table 3 tabulates the mean values (\pm spatial standard deviation) of the pharmacokinetic rates

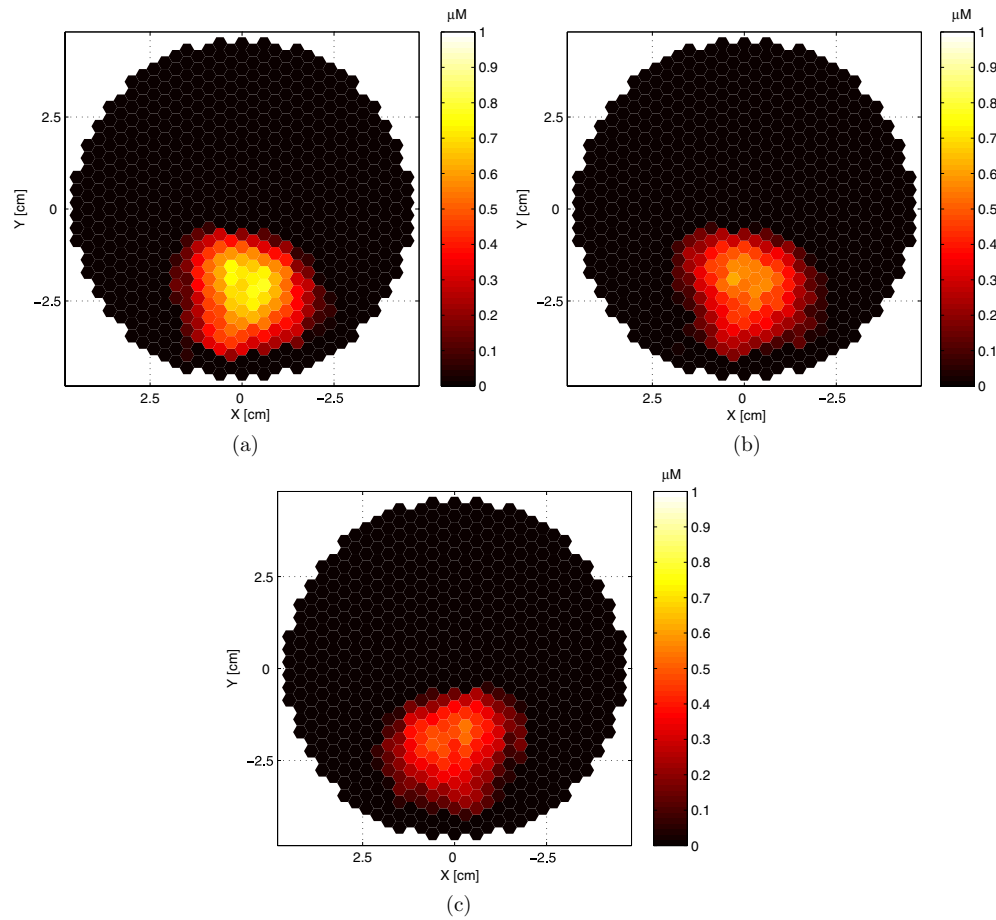


Figure 14. ICG concentration images in the EES for case 3 for (a) 246.4th, (b) 378.4th and (c) 510.4th s.

Table 4. Bulk pharmacokinetic rates extracted from the entire breast tissue.

| | $k_{in} (\text{sec}^{-1} 10^{-2})$ | $k_{out} (\text{sec}^{-1} 10^{-2})$ | $k_{elm} (\text{sec}^{-1} 10^{-3})$ |
|--------|------------------------------------|-------------------------------------|-------------------------------------|
| Case 1 | 0.84 ± 0.013 | 0.62 ± 0.017 | 3.66 ± 0.042 |
| Case 2 | 2.01 ± 0.022 | 0.83 ± 0.012 | 4.01 ± 0.054 |
| Case 3 | 4.06 ± 0.072 | 3.36 ± 0.051 | 4.37 ± 0.052 |

for the tumor region and outside the tumor region for all three cases. The pharmacokinetic rates are higher for case 3 (invasive ductal carcinoma), for both the tumor region and outside the tumor region as compared to case 2 (adenocarcinoma). Similarly, the kinetic rates are higher for case 2 (adenocarcinoma), as compared to case 1 (fibroadenoma) for both the tumor region and outside the tumor region. This observation shows that high mean values of k_{in} and k_{out} may be indicative of tumor aggressiveness.

To understand the value of pharmacokinetic rate imaging as compared to the bulk pharmacokinetic rate analysis, we averaged the concentration images spatially, and obtained

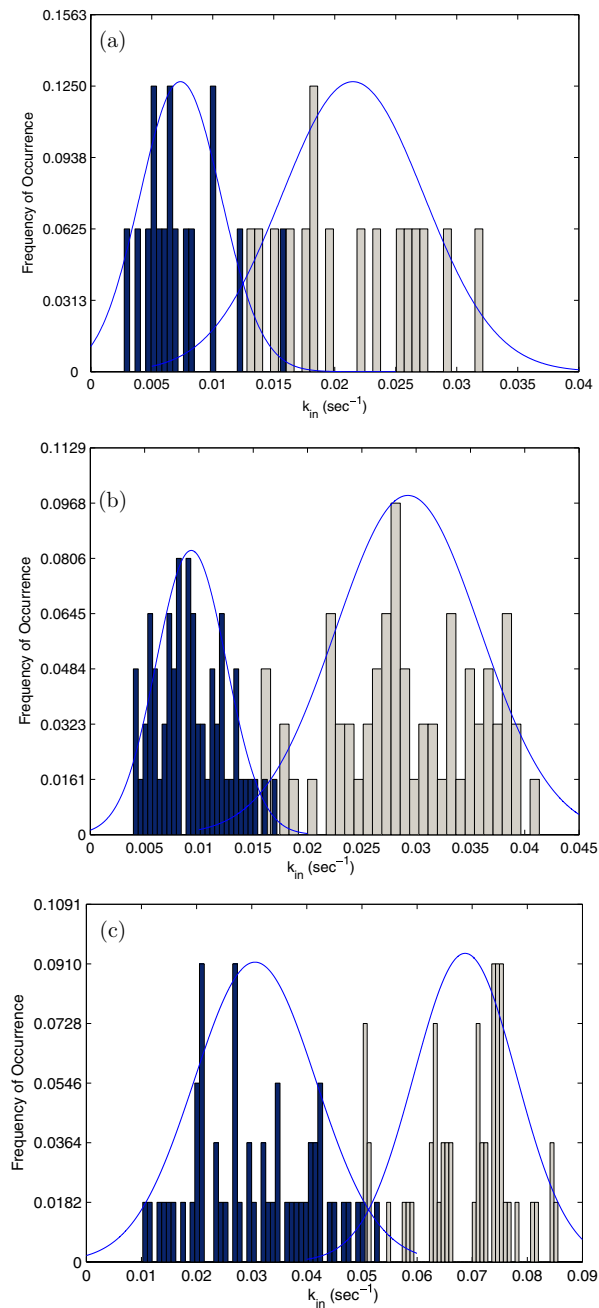


Figure 15. The histograms of k_{in} for (a) case 1, (b) case 2, (c) case 3 for the tumor region (light gray) and outside (blue/dark gray) the tumor region (as indicated by circular/elliptical regions). The solid lines in figures show the Gaussian fit.

a bulk concentration value for each time instant. We then formed a time curve for the bulk ICG concentrations. Next, we fit the two-compartment model to the resulting time curves and estimated the bulk pharmacokinetic rates. Table 4 tabulates the bulk pharmacokinetic rates

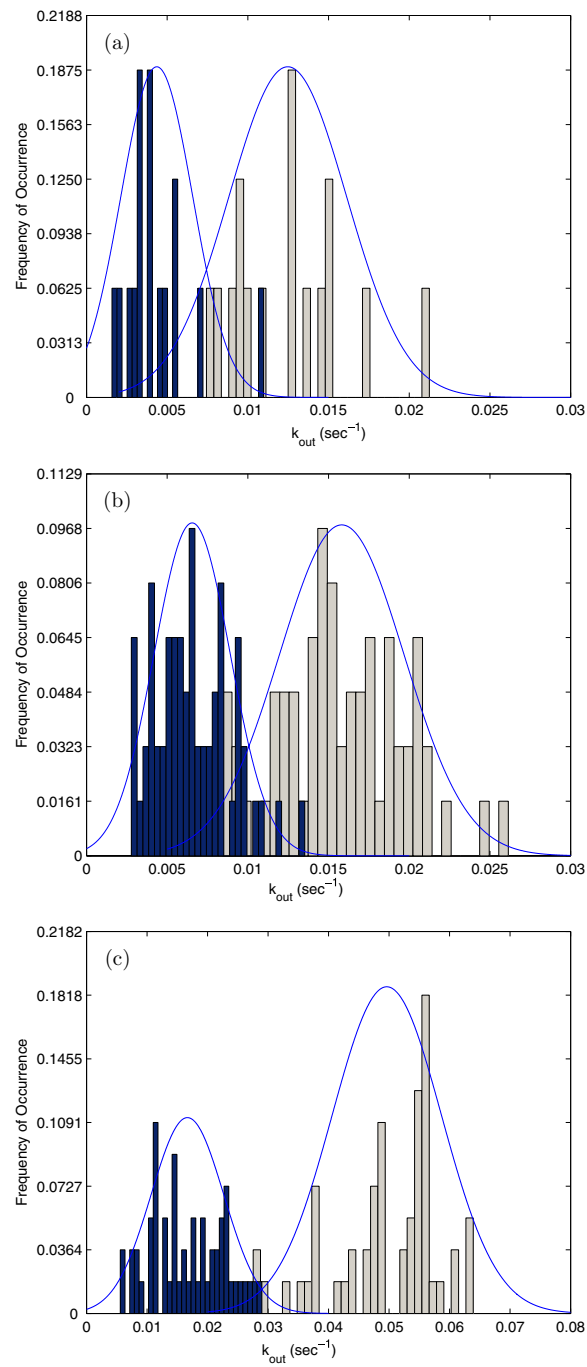


Figure 16. The histograms of k_{out} for (a) case 1, (b) case 2, (c) case 3 for the tumor region (light gray) and outside (blue/dark gray) the tumor region (as indicated by circular/elliptical regions). The solid lines in figures show the Gaussian fit.

for each patient. To compare the bulk rates with spatially resolved rates, in figures 17 and 18, the bulk pharmacokinetic rates are overlaid on the histograms of the pharmacokinetic rate

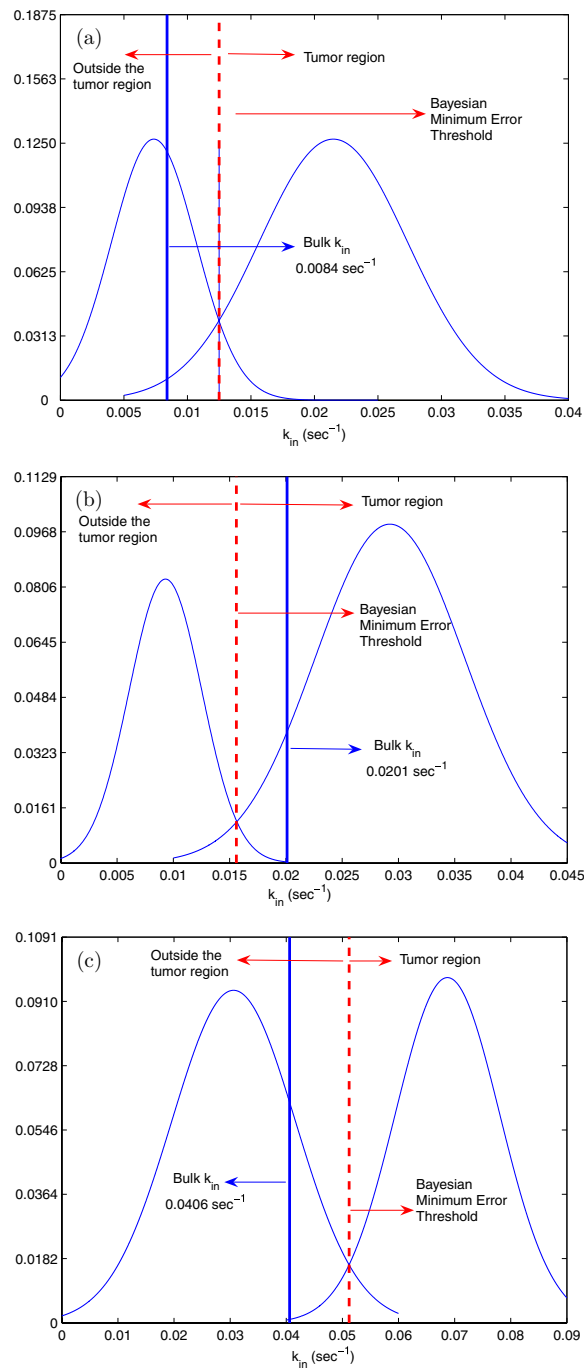


Figure 17. Solid lines (blue) shows bulk k_{in} rates for (a) case 1, (b) case 2, (c) case 3 together with the histogram fits. The dashed (red) line indicates the Bayesian minimum error classifier threshold.

images. The dotted line shows the Bayesian minimum error classifier threshold (the value corresponding to the intersection of the histograms) (Fukunaga 1990) for each case. We see

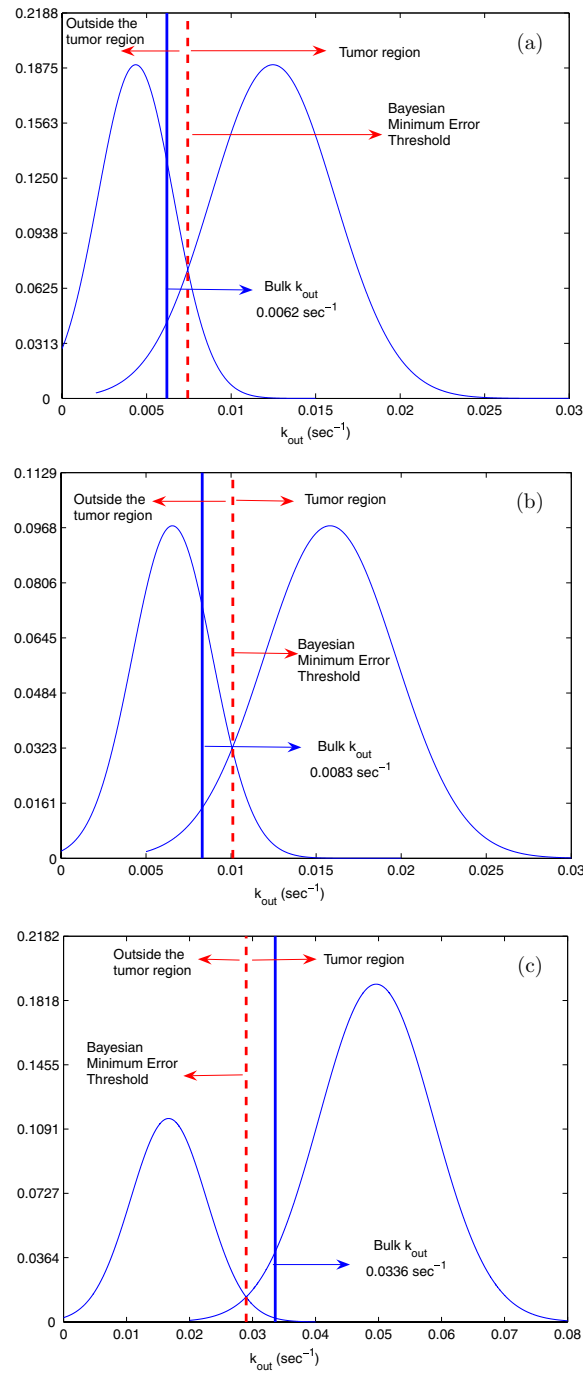


Figure 18. Solid lines (blue) shows bulk k_{out} rates for (a) case 1, (b) case 2, (c) case 3 together with the histogram fits. The dashed (red) line indicates the Bayesian minimum error classifier threshold.

that for case 1, the bulk rates of k_{in} and k_{out} are both classified as healthy tissue (outside the tumor region). For case 2, k_{in} is classified as cancerous tissue (in the tumor region) and k_{out} is

classified as healthy tissue. Similarly for case 3, k_{in} is classified as healthy and k_{out} is classified as cancerous tissue. This indicates that spatially resolved rates may provide more consistent and superior information than the bulk rates.

5. Conclusion

In this study, we presented a method of forming pharmacokinetic-rate images and reported pharmacokinetic rate images of ICG for three patients with breast tumors. To form pharmacokinetic rate images, we first obtained a sequence of ICG concentration images using the differential diffuse optical tomography technique. We next employed the two-compartment model, and estimated the pharmacokinetic rates and concentrations in each compartment for each voxel using the EKF framework. We have shown in our prior work (Alacam *et al* 2006) that the EKF framework has a number of advantages in pharmacokinetic rate estimation, some of which include robust estimation in the presence of measurement noise and dynamic model uncertainties.

We formed the pharmacokinetic rate images using the *in vivo* data obtained from three patients with breast tumors. We also obtained bulk pharmacokinetic rates for each patient. Both spatially resolved and bulk rates show that high values of k_{in} and k_{out} may be indicative of tumor aggressiveness. Along with the pharmacokinetic rates, we also estimated the ICG concentrations in plasma and EES compartments. We observed that ICG concentrations in plasma and the EES compartments are higher in the tumor region agreeing with the hypothesis that around the tumor region ICG may act as a diffusible extravascular flow in leaky capillary of tumor vessels.

Comparison of spatially resolved and bulk ICG pharmacokinetic rates show that ICG pharmacokinetic imaging may provide more consistent and superior information than bulk ICG pharmacokinetic rates.

While the available patient data are limited to perform a full scale receiver operating characteristic study, clearly, pharmacokinetic rate imaging provides a new tool to investigate and improve breast cancer diagnosis, staging, and treatment monitoring. This includes extraction of new quantitative features from ICG pharmacokinetic rate images, within patient comparison of these features, and statistical analysis of spatial distribution of pharmacokinetic rates. We leave for future work to collect sufficient number of patient data, and to fully investigate the value of ICG pharmacokinetic rate imaging for breast cancer diagnosis, staging, and treatment monitoring.

Acknowledgments

This work was supported by US Army Medical Research Acquisition Activity under grant W81XWH-04-1-0559, and the Center for Subsurface Sensing and Imaging Systems, under the Engineering Research Centers Program of the National Science Foundation, Award Number EEC-9986821.

References

- Alacam B, Yazici B, Intes X and Chance B 2006 Extended Kalman filtering for the modeling and analysis of ICG pharmacokinetics in cancerous tumors using NIR optical methods *Trans. IEEE Biomed. Eng.* **53** 1861–71
- Anderson D H 1983 *Lecture Notes in Biomathematics: Compartmental Modeling and Tracer Kinetics* (Berlin: Springer)
- Arridge S R 1999 Optical tomography in medical imaging *Inverse Problems* **15** 41–93

- Boas D, Gaudette T and Arridge S 2001 Simultaneous imaging and optode calibration with diffuse optical tomography *Opt. Exp.* **8** 263–70
- Boppart S A, Luo W, Marks D L and Singletary K W 2004 Optical coherence tomography: feasibility for basic research and image-guided surgery of breast cancer *Breast Cancer Res. Treat.* **84** 85–97
- Chen C 1999 *Linear System Theory and Design* (New York: Oxford University Press)
- Cuccia D J, Bevilacqua F, Durkin A J, Merritt S, Tromberg B J, Gulsen G, Yu H, Wang J and Nalcioglu O 2003 *In vivo* quantification of optical contrast agent dynamics in rat tumors by use of diffuse optical spectroscopy with magnetic resonance imaging coregistration *Appl. Opt.* **42** 2940–50
- ElDeosky A, Seifalian A, Cope M, Delpy D and Davidson B 1999 Experimental study of liver dysfunction evaluated by direct indocyanine green clearance using near infrared spectroscopy *Br. J. Surg.* **86** 1005–11
- Fukunaga K 1990 *Introduction to Statistical Pattern Recognition* (New York: Academic)
- Gu X, Zhang Q, Larcom L and Jiang H 2004 Three-dimensional bioluminescence tomography with model-based reconstruction *Opt. Exp.* **12** 3996–4000
- Gurfinkel M *et al* 2000 Pharmacokinetics of ICG and HPPH-car for the detection of normal and tumor tissue using fluorescence, near-infrared reflectance imaging: a case study *Photochem. Photobiol.* **72** 94–102
- Hansen D, Spence A, Carski T and Berger M 1993 Indocyanine green (ICG) staining and demarcation of tumor margins in a rat glioma model *Surg. Neurol.* **40** 451–6
- Hansen P and O’Leary D 1993 The use of the *L*-curve in the regularization of discrete ill-posed problems *SIAM J. Sci. Comput.* **14** 1487–503
- Intes X and Chance B 2005 Non-PET functional imaging techniques: optical *Radio. Clin. North Am.* **43** 221–34
- Intes X, Ripoll J, Chen Y, Nioka S, Yodh A G and Chance B 2003 *In vivo* continuous-wave optical breast imaging enhanced with indocyanine green *Med. Phys.* **30** 1039–47
- Jacquez J A 1972 *Compartmental Analysis in Biology and Medicine: Kinetics of Distribution of Tracer-labeled Materials* (New York: Elsevier)
- Landsman M L J, Kwant G, Mook G A and Zijlstra W G 1976 Light-absorbing properties, stability, and spectral stabilization of indocyanine green *J. Appl. Physiol.* **40** 575–83
- Ljung L 1979 Asymptotic behavior of the extended Kalman filter as a parameter estimator for linear systems *IEEE Trans. Auto. Control* **AC24** 36–50
- Mahmood U, Tung C H, Bogdanov Jr A and Weissleder R 1999 Near infrared optical imaging of protease activity for tumor detection *Radiology* **213** 866–70
- Milstein A B, Webb K J and Bouman C A 2005 Estimation of kinetic model parameters in fluorescence optical diffusion tomography *J. Opt. Soc. Am.* **22** 1357–68
- Mussurakis S, Buckley D L, Drew P J, Fox J N, Carleton P J, Turnbull L W and Horsman A 1997 Dynamic MR imaging of the breast combined with analysis of contrast agent kinetics in the differentiation of primary breast tumours *Clin. Radiol.* **52** 516–26
- Nelson L and Stear E 1976 The simultaneous on-line estimation of parameters and states in linear systems *IEEE Trans. Auto. Control* **21** 94–8
- Nioka S, Yung Y, Schnall M, Zhao S, Orel S, Xie C, Chance B and Solin S 1997 Optical imaging of breast tumor by means of continuous waves *Adv. Exp. Med. Biol.* **411** 227–32
- Ntziachristos V, Chance B and Yodh A 1999 Differential diffuse optical tomography *Opt. Exp.* **5** 230–42
- Ntziachristos V, Yodh A G, Schnall M and Chance B 2000 Concurrent MRI and diffuse optical tomography of breast after indocyanine green enhancement *Med. Sci.* **97** 2767–72
- O’Leary M 1996 Imaging with diffuse photon density waves *PhD Thesis* Department of Physics & Astronomy, University of Pennsylvania
- Ripoll J, Ntziachristos V, Carminati R and Nieto-Vesperinas M 2001a Kirchhoff approximation for diffusive waves *Phys. Rev.* **64** 051917
- Ripoll J, Ntziachristos V, Culver J P, Pattanayak D N, Yodh A G and Nieto-Vesperinas M 2001b Recovery of optical parameters in multilayered diffusive media: theory and experiments *J. Opt. Soc. Am. A* **18** 821–30
- Sevick-Muraca E M, Lopez G, Troy T L, Reynolds J S and Hutchinson C L 1997 Fluorescence and absorption contrast mechanisms for biomedical optical imaging using frequency-domain techniques *Photochem. Photobiol.* **66** 55–64
- Shinohara H, Tanaka A, Kitai T, Yanabu N, Inomoto T, Satoh S, Hatano K, Yamaoka Y and Hirao K 1996 Direct measurement of hepatic indocyanine green clearance with near-infrared spectroscopy: separate evaluation of uptake and removal *Hepatology* **23** 137–44
- Su M Y, Yu H J, Carpenter P M, McLaren C E and Nalcioglu O 2005 Pharmacokinetic parameters analyzed from MR contrast enhancement kinetics of multiple malignant and benign breast lesions detected in the same patients *Technol. Cancer Res. Treat.* **4** 255–63

- Sun H, Collins J M, Mangner T J, Muzik O and Shields A 2006 Imaging the pharmacokinetics of [F-18]FAU in patients with tumors: PET studies *Cancer Chemother. Pharmacol.* **57** 343–8
- Togneri R and Deng L 2003 Joint state and parameter estimation for a target-directed nonlinear dynamic system model *IEEE Trans. Sig. Proc.* **51** 3061–70
- Tornøe C W 2002 Grey-box PK/PD modeling of insulin *MS Thesis* Technical University of Denmark
- Vaupel P, Schlenger K, Knoop C and Hockel M 1991 Oxygenation of human tumors: evaluation of tissue oxygen distribution in breast cancers by computerized O₂ tension measurements *Cancer Res.* **51** 3316–22
- Yodanis C L and Chance B 1995 Spectroscopy and imaging with diffusing light *Phys. Tod.* **48** 34–40